

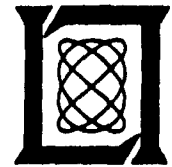
AD-A201 044

Quarterly Technical Report

Solid State Research

1988:1

**Lincoln Laboratory**  
MASSACHUSETTS INSTITUTE OF TECHNOLOGY  
*LEXINGTON, MASSACHUSETTS*



Prepared under Electronic Systems Division Contract F1962B-85-C-0002.

Approved for public release; distribution unlimited.

**DTIC**  
**ELECTE**  
**S** DEC 02 1988  
**E**

88 12 2 084

The work reported in this document was performed at Lincoln Laboratory, a center for research operated by Massachusetts Institute of Technology, with the support of the Department of the Air Force under Contract F19628-85-C-0002.

This report may be reproduced to satisfy needs of U.S. Government agencies.

The views and conclusions contained in this document are those of the contractor and should not be interpreted as necessarily representing the official policies, either expressed or implied, of the United States Government.

The ESD Public Affairs Office has reviewed this report, and it is releasable to the National Technical Information Service, where it will be available to the general public, including foreign nationals.

This technical report has been reviewed and is approved for publication.

FOR THE COMMANDER

*Hugh L. Southall*

Hugh L. Southall, Lt. Col., USAF  
Chief, ESD Lincoln Laboratory Project Office

Non-Lincoln Recipients

**PLEASE DO NOT RETURN**

Permission is given to destroy this document  
when it is no longer needed.

**MASSACHUSETTS INSTITUTE OF TECHNOLOGY  
LINCOLN LABORATORY**

**SOLID STATE RESEARCH**

**QUARTERLY TECHNICAL REPORT**

**1 NOVEMBER 1987 — 31 JANUARY 1988**

**ISSUED 5 AUGUST 1988**

**Approved for public release; distribution unlimited.**

**LEXINGTON**

**MASSACHUSETTS**

## **ABSTRACT**

This report covers in detail the research work of the Solid State Division at Lincoln Laboratory for the period 1 November 1987 through 31 January 1988. The topics covered are Solid State Device Research, Quantum Electronics, Materials Research, Microelectronics, and Analog Device Technology. Funding is provided primarily by the Air Force, with additional support provided by the Army, DARPA, Navy, SDIO, NASA, and DOE.

## TABLE OF CONTENTS

Abstract	iii
List of Illustrations	vii
List of Tables	xi
Introduction	xiii
Reports on Solid State Research	xvii
Organization	xxv
 1. SOLID STATE DEVICE RESEARCH	 1
1.1 Integrated-Optical $2 \times 2$ Switch with Y-Branch Mode Splitters	1
1.2 Hybrid Approach to Surface-Emitting Two-Dimensional Diode Laser Arrays	3
1.3 High-Performance InGaAsP/InP Buried-Heterostructure Lasers Defined by Ion-Beam-Assisted Etching	8
1.4 Buried-Heterostructure Diode Lasers Emitting at $1.4 \mu\text{m}$	12
1.5 Growth of InP on GaAs by OMVPE	15
 2. QUANTUM ELECTRONICS	 19
2.1 Electrooptically Tuned Single-Frequency Ti:Al <sub>2</sub> O <sub>3</sub> Laser	19
2.2 Interferometric Measurement of Optically Induced Refractive Index Changes in Ti:Al <sub>2</sub> O <sub>3</sub>	22
2.3 Microcavity Nd:YAG Laser	26
2.4 Frequency Conversion	28
 3. MATERIALS RESEARCH	 35
3.1 Liquid-Solid Interface Morphologies and Defect Structures in Zone-Melting-Recrystallized Si-on-Insulator Films	35
3.2 IrSi Schottky-Barrier Infrared Detectors	43
 4. MICROELECTRONICS	 51
4.1 Diamond Permeable Base Transistor	51
4.2 Laser-Direct-Write Tuning and Modification of Monolithic Microwave Integrated Circuits	54
4.3 GaAs Growth on Diamond Substrates by MBE	57

5. ANALOG DEVICE TECHNOLOGY	59
5.1 Control of Stoichiometry of Reactively Sputtered Niobium Nitride Films	59
5.2 Superconducting Analog Track-and-Hold Circuit	62
5.3 Four-Channel, 128-Sample, 64-Tap Analog-Ternary CCD Correlator	68

## LIST OF ILLUSTRATIONS

Figure No.		Page
1-1	Schematic Illustration of the $2 \times 2$ Switch in the (a) Bar State, and (b) Cross State. For Both Cases, the Field Profiles of Light Incident on the Wide and Narrow Input Guides as it Traverses Through the Switch Are Shown by Solid and Dashed Lines, Respectively.	2
1-2	Schematic Illustration of Hybrid Two-Dimensional Surface-Emitting Diode Laser Array	4
1-3	(a) Sawed Cross Section of Groove Etched in Si with Flat Bottom and $45^\circ$ Sidewalls. (b) Top View of Linear Laser Array Mounted in Metallized Si Groove. Reflections of the Cleaved End Facets of the GaAs/AlGaAs Linear Bar Array Can Be Seen in the $45^\circ$ Deflecting Mirrors.	5
1-4	Near-Field Pattern of a Hybrid Two-Dimensional Surface-Emitting Laser Array Consisting of Three 4-mm-Wide GaAs/AlGaAs Linear Bar Arrays Mounted in Three Separate Grooves on a Common Si Substrate	6
1-5	Power Output vs Pulsed Current of the Three-Laser-Bar Hybrid Array Whose Near-Field Pattern Is Shown in Figure 1-4. Here, Each Bar Was Driven Separately.	7
1-6	IBAE-Defined MTBH Lasers Before Metallization. (a) Schematic Cross-Sectional View. (b) SEM Perspective View.	9
1-7	Room-Temperature, Light-Current Characteristic of IBAE-Defined MTBH Lasers. (a) CW Characteristics of Five Adjacent Lasers, with the Horizontal Scale Shifted by 10 mA for Each Device, and (b) Pulsed Characteristic of a Single Laser.	10
1-8	Far-Field Patterns in the Junction Plane Measured at Four Current Levels.	11
1-9	SEM Micrograph Showing High Quality Interface Between the $\lambda = 1.4\text{-}\mu\text{m}$ Alloy and the p-Type InP Buffer Layer and the n-Type InP Cap Layer. There Is No Evidence of Dissolution of the Alloy into the InP Growth Solution.	12
1-10	Optical Power vs Current Before AR Coating. Solid Circle Indicates Current at Which Spectrum Shown in Figure 1-11 Was Recorded.	13
1-11	Typical Mode Spectrum of the $\lambda = 1.4\text{-}\mu\text{m}$ Lasers	14

Figure No.		Page
1-12	Nomarski Photomicrographs of InP Growth on (100) GaAs Substrates. The Top Photo Shows Growth Typical of a Single-Step Process, and the Bottom Photo Shows the Improvement That Results When the Growth at 650°C Is Preceded by the Deposition of 100-200 Å Layer at 400°C.	16
1-13	Typical Profile of Relative Growth Thickness vs Position on Substrate. Here 100 Corresponds to 1.5 μm.	17
2-1	Time Dependence of the Single-Frequency Ti:Al <sub>2</sub> O <sub>3</sub> Laser Intensity. Three Electrooptic Crystals, Including a MgO-Doped LiNbO <sub>3</sub> Crystal, Are in the Laser Cavity. The Fall in Intensity Is Fit by an Exponential Decay with a Lifetime of 30 s Caused by Photorefractive Damage of the MgO-Doped LiNbO <sub>3</sub> Crystal.	20
2-2	Electrooptic Switching of the Single-Frequency Ti:Al <sub>2</sub> O <sub>3</sub> Laser. The Upper Trace Shows the Voltage Applied to the LiNbO <sub>3</sub> Crystal. The Lower Trace Shows the Transmission with the Crystal Operating at the Lower Voltage. The Applied Voltage Is a Repetitive Square Wave of 100 V.	21
2-3	Schematic of the Experimental Setup for the Interferometric Measurement of Optically Induced Changes in Refractive Index $ \Delta n_\pi $ and $ \Delta n_o $ . BS1 and BS2 Denote Beamsplitters, and M1 and M2 Denote Mirrors.	23
2-4	Temporal Dependence of the Intensity $I$ of the Transmitted Signal Beam for the $\sigma$ Polarization. $I_{\max}$ and $I_{\min}$ Are the Minimum and Maximum Values of $I$ .	24
2-5	(a) Induced Phase and Index of Refraction Changes for the $\pi$ and $\sigma$ Polarizations vs Incident Pump Energy Density. (b) Difference in Induced Phase Change and Index of Refraction Changes Between the $\pi$ and $\sigma$ Polarizations Obtained from Interferometric and Optically Induced Birefringence Measurements. Straight Lines Are Linear Fits to the Data, Which Are Shown as Circles.	25
2-6	(a) Illustration of a Diode-Pumped Microcavity Solid State Laser. (b) Gain Spectrum of a Solid State Medium Shown Superimposed on the Cavity Mode Spacing of a Microcavity Laser to Illustrate Why Single-Frequency Operation Occurs.	26
2-7	Photograph of a Microcavity Nd:YAG Laser, Showing the Gain Medium and Cavity Mirrors.	27
2-8	(a) Instrument-Limited-Spectrometer and (b) Fabry-Perot Traces of the Output of the Nd:YAG Microcavity Laser.	29

Figure No.		Page
2-9	Input-Output Power Characteristics of the Nd:YAG Microcavity Laser. The Input Power Shown Is the Absorbed Pump Power, and the Output Power Was Measured from the Output Face of the Cavity Only.	29
2-10	Temporal Pulse Envelope of Mode-Locked Nd:YAG Laser.	30
2-11	Internal Frequency-Doubling Efficiency vs Incident Power Density in KD*P Crystals for a Macropulse Length of 1 $\mu$ s and PRF of 10 Hz.	30
2-12	Internal Frequency-Doubling Efficiency vs Incident Power Density in BaB <sub>2</sub> O <sub>4</sub> for a Macropulse Length of 1 $\mu$ s and PRF of 10 Hz.	32
3-1	Interface Morphologies as a Function of Increasing Upper-Strip Power. (a) 2.43 kW, (b) 2.49 kW, (c) 2.54 kW.	36
3-2	Cell Spacing for Four Grains as a Function of Power Supplied to the Upper Strip	37
3-3	Optical Micrographs Showing Three Types of Defects. (a) Trails of Isolated Dislocations. (b) Trails of Dislocation Clusters. (c) Continuous Subboundaries.	38
3-4	Fraction of the Three Defect Types Shown in Figure 3-3, Plotted as a Function of Power (Data Were Taken from a Single Grain).	39
3-5	Interface Morphologies as a Function of Increasing Velocity. (a) 90 $\mu$ m/s, (b) 330 $\mu$ m/s, (c) 420 $\mu$ m/s. Upper-Strip Power = 2.5 kW.	40
3-6	Dependence of Cell Period on Zone Velocity.	41
3-7	Optical Micrographs Showing Defect Patterns Obtained for Velocities of (a) 90 $\mu$ m/s, (b) 330 $\mu$ m/s, and (c) 420 $\mu$ m/s.	42
3-8	High-Resolution Cross-Sectional Transmission Electron Micrographs of Ir-Si Samples Prepared by (a) Present and (b) Previous Processing Procedures.	44
3-9	(a) Forward and (b) Reverse Current-Voltage Characteristics at Four Temperatures for an IrSi Schottky-Barrier Detector. The Active Device Area Is $1.37 \times 10^{-3}$ cm <sup>2</sup> .	45
3-10	Plot of $J/T^2$ vs Reciprocal Absolute Temperature $1/T$ for the IrSi Detector of Figure 3-9, Where $J$ Is the Dark-Current Density at a Reverse Bias Voltage $V_R = 1$ V.	46
3-11	Plot of $(Y h\nu)^{1/2}$ vs Photon Energy $h\nu$ for the IrSi Detector of Figure 3-9, Where $Y$ Is the Quantum Efficiency Measured at a Reverse Bias Voltage $V_R = 2$ V.	47

Figure No.		Page
4-1	Electron Velocity as a Function of Electric Field for Several Semiconductors (References 1, 2, and 3). The Curves Are Terminated at the Approximate Position of the Electric Field Breakdown for Each Semiconductor (Reference 4).	51
4-2	Theoretical Curve of the Maximum Operational Voltage of a Transistor as a Function of the Cutoff Frequency $f_T$ for Several Semiconductors (Reference 5).	52
4-3	Thermal Conductivities of Several Solids as a Function of Temperature. The Vertical Gray Band Around 300 K Represents the Temperature Range from -25 to 125°C. The Thermal Conductivity of Ila Diamond Is Displayed (Reference 6).	53
4-4	(a) Schematic Diagram of a Diamond Permeable Base Transistor. To Fabricate This Device, Ion-Beam-Assisted Etching Was Used to Produce the Grating in the Diamond (Reference 9). (b) Collector Current as a Function of Collector-Emitter Voltage for Base Emitter Voltage Steps of 2 V.	54
4-5	Circuit Trimming of a Ka-band Attenuator. (a) SEM Micrograph of the Monolithic Attenuator Using W Lines as Tuning Inductors. (b) Measured Transmission for Different Gate Biases Without W Tuning Inductors. (c) Measured Transmission With Laser-Direct-Written Tuning Inductors.	56
5-1	(a) Variation of the Target Voltage and Transition Temperature as a Function of Nitrogen Flow for Reactive Sputtering of NbN. (b) Variation of the Deposition Rate, Emissivity, Nitrogen Consumption, and Transition Temperature as a Function of Nitrogen Flow.	61
5-2	Schematic Diagram of the Feedback Control Mechanism to Maintain the Stoichiometry of the NbN Films.	62
5-3	(a) Circuit Diagram of Superconducting Analog Track-and Hold. (b) Sine-Shaped-Junction Threshold Curve.	63
5-4	(a) Shaped Junction Lumped-Element Equivalent Circuit. (b) Simulated Equivalent-Time Response to a Pulsed Input.	65
5-5	Test Apparatus for High-Speed Analog Measurements.	66
5-6	(a) Real-Time Input Signal Pulse. (b) Gating Pulse Used to Trigger the Track-and-Hold. The Gating Pulse Is Swept Across the Input (a) to Produce the Equivalent-Time Response (c).	67

<b>Figure No.</b>		<b>Page</b>
5-7	Equivalent-Time Response of Track-and-Hold to a 1-GHz Sinusoidal Input Signal Phase-Locked to the System Clock.	68
5-8	Photomicrograph of a Four-Channel, 128-Sample, 64-Tap Analog-Ternary CCD Correlator. The Chip Size is $4.8 \times 5.83$ mm.	69
5-9	Performance of the Correlator in Processing a 63-Chip m-Sequence at a 10-MHz Sample Rate, Displayed at a Sweep Rate of (a) $1.4 \mu\text{s}/\text{div}$ and (b) $100 \text{ ns}/\text{div}$ .	71

## LIST OF TABLES

<b>Table No.</b>		<b>Page</b>
1-1	Experimental Performance of Integrated-Optical $2 \times 2$ Switch at $\lambda = 1.15 \mu\text{m}$ for Cross (X) and Bar (=) States.	3
5-1	Track-and-Hold Circuit Parameters	64
5-2	Correlator Specifications	70

## INTRODUCTION

### 1. SOLID STATE DEVICE RESEARCH

A  $2 \times 2$  optical switch consisting of an interferometric modulator and asymmetric Y-branch mode splitters has been demonstrated. This device offers low switching voltage and has no critical fabrication tolerances.

A hybrid two-dimensional surface-emitting diode laser array consisting of three GaAs/AlGaAs linear laser arrays with cleaved facets mounted in grooves etched in a Si substrate has been fabricated and tested. With 11- to 12-A pulsed drive current, a power output of about 10 W with a differential quantum efficiency greater than 65 percent has been obtained from each linear array.

Ion-beam-assisted etching has been used to fabricate InGaAsP/InP mass-transported buried-heterostructure lasers. These lasers have uniform device characteristics, state-of-the-art threshold currents and differential quantum efficiencies, linear L-I characteristics to high output powers, and smooth far-field patterns.

Growth, fabrication, and testing of InGaAsP/InP double-heterostructure diode lasers emitting at a wavelength of  $1.4 \mu\text{m}$  have been successfully completed. To the extent of the tests, these devices are found to exhibit high performance similar to that of the  $\lambda = 1.3\text{-}\mu\text{m}$  devices previously reported.

InP with good morphology has been grown on (100) GaAs substrates by adding an initial low-temperature step to the OMVPE growth process. This provides a convenient method for measuring deposition uniformity in the OMVPE reactor.

### 2. QUANTUM ELECTRONICS

A Ti:Al<sub>2</sub>O<sub>3</sub> ring laser has been tuned from 767 to 834 nm while maintaining single-frequency operation by using three electrooptic birefringent filters. MgO-doped LiNbO<sub>3</sub>, which is used for the highest order ( $\sim 3000$ ) birefringent filter, is subject to photorefractive damage that limits the laser operation to 2 min.

Optically induced refractive index changes of Ti:Al<sub>2</sub>O<sub>3</sub> pumped at 532 nm have been measured interferometrically at 632.8 nm. These changes, which decay with the 3- $\mu\text{s}$  fluorescence lifetime of Ti<sup>3+</sup> ions, are attributed to nonresonant dispersion effects.

A 1.06- $\mu\text{m}$  laser that exhibits both single longitudinal mode and single transverse mode operation has been constructed from a 700- $\mu\text{m}$  slab of Nd:YAG sandwiched between two flat mirrors. When the laser is pumped at the Nd:YAG absorption peak near 809 nm, a threshold of less than 1 mW is observed, with a slope quantum efficiency of greater than 30 percent.

Frequency-doubling experiments have been carried out in KD\*P and  $\beta\text{-BaB}_2\text{O}_4$  crystals using a modified Nd:YAG laser system to provide the 1.064- $\mu\text{m}$  radiation. Second harmonic generation efficiencies in excess of 50 percent have been achieved in both materials with the laser producing a 1- $\mu\text{s}$  macropulse at 10-Hz repetition frequency.

### 3. MATERIALS RESEARCH

Liquid-solid interface morphologies observed by *in situ* optical microscopy during zone-melting recrystallization of Si-on-insulator films have been correlated with the defect morphologies of the recrystallized films. Stable cellular solidification fronts, which are obtained at low zone velocities if the radiation intensity gradient in the interfacial region is small, yield subboundary-free films.

IrSi Schottky-barrier infrared detectors with a cutoff wavelength beyond 9  $\mu\text{m}$  have been fabricated by *in situ* processing under vacuum. High-resolution transmission electron microscopy shows that these detectors have clean, abrupt silicide-Si interfaces.

### 4. MICROELECTRONICS

Permeable-base transistors have been fabricated in diamond, demonstrating the potential of this wide-bandgap material for practical devices. The measured transconductance was 30  $\mu\text{S}/\text{mm}$ , limited primarily by series bulk resistance.

Laser-direct-writing techniques have been adapted to the modification of conventionally fabricated monolithic microwave integrated circuits. As one example, shunt inductors have been added to a 30-GHz active attenuator in order to tune out the drain-source capacitances of GaAs MESFETs.

Molecular beam epitaxy has been used to grow GaAs on diamond as a possible material system for power devices. Layers grown on the (110) surface of diamond result in twinned (111)-oriented GaAs, and layers on the (100) surface of diamond are polycrystalline.

### 5. ANALOG DEVICE TECHNOLOGY

The target voltage, deposition rate, and nitrogen consumption have been measured as a function of the nitrogen flow for the reactive sputtering of niobium nitride thin films and correlated with the superconductive transition temperature for these films. Based on the sharp increase in the target voltage observed for nitrogen flows corresponding to films with the highest transition temperature, a simple scheme using the target voltage to control the nitrogen flow has been implemented, allowing high-quality NbN films to be consistently obtained.

A superconducting analog track-and-hold circuit has been designed, fabricated, and tested. A 1.2-GHz bandwidth and a 34-dB dynamic range have been measured, and model calculations indicate that bandwidths of 20 GHz can be achieved.

A flexible, programmable, analog-ternary (allowed reference weights of +1, -1, and 0) correlator has been designed and fabricated using 4- $\mu\text{m}$  n-channel CCD technology. The device has achieved very high dynamic range ( $> 66$  dB), operates at up to 40-MHz sample rates, has a programmable length of up to 128 samples, and, by using a high level of integration, has been made self-contained, adjustment-free, and compatible with standard logic levels and power-supply voltages.

## REPORTS ON SOLID STATE RESEARCH

1 November 1987 through 31 January 1988

### PUBLISHED REPORTS

#### Journal Articles

#### JA No.

- |      |   |  |  |
|------|---|--|--|
| 5991 | Excimer-Laser In Situ Treatment of GaAs Surface: Electrical Properties of Tungsten/GaAs Diodes  | P.A. Maki<br>D.J. Ehrlich  | Appl. Phys. Lett. <b>51</b> , 1274 (1987)                |
| 5994 | Visible-Laser Etching of Refractory Metals by Surface Modification  | M. Rothschild<br>J.H.C. Sedlacek<br>D.J. Ehrlich   | J. Vac. Sci. Technol. B <b>5</b> , 1400 (1987)           |
| 5997 | Electrical Properties of Fe-Doped Semi-insulating InP After Proton Bombardment and Annealing  | J.D. Woodhouse<br>J.P. Donnelly<br>G.W. Iseler   | Solid-State Electron. <b>31</b> , 13 (1988)              |
| 6008 | Characterization of Mass-Transported p-Substrate GaInAsP/InP Buried-Heterostructure Lasers with Analytical Solutions for Electrical and Thermal Resistances | Z.L. Liao<br>J.N. Walpole<br>D.Z. Tsang<br>V. Diadiuk  | IEEE J. Quantum Electron. <b>QE-24</b> , 36 (1988)       |
| 6012 | Nanometer-Scale Columns in GaAs Fabricated by Angled Chlorine Ion-Beam-Assisted Etching   | W.D. Goodhue<br>S.W. Pang<br>G.D. Johnson<br>D.K. Astolfi<br>D.J. Ehrlich                          | Appl. Phys. Lett. <b>51</b> , 1726 (1987)                |
| 6025 | 30- $\mu$ m Heterodyne Receiver   | T.Kostiuk*<br>D.L. Spears  | Int. J. Infrared Millimeter Waves <b>8</b> , 1269 (1987) |
| 6044 | Infrared Anisotropy of $\text{La}_{1.85}\text{Sr}_{0.15}\text{CuO}_{4-y}$   | G.L. Doll*<br>J. Steinbeck*<br>G. Dresselhaus*<br>M.S. Dresselhaus*<br>A.J. Strauss<br>H.J. Zeiger | Phys. Rev. B <b>36</b> , 8884 (1987)                     |

---

\* Author not at Lincoln Laboratory.

## PUBLISHED REPORTS

### Meeting Speeches

#### MS No.

- |      |   |  |  |
|------|---|--|--|
| 7167 | Analog Signal Correlator Using Superconductive Integrated Components  | J.B. Green<br>L.N. Smith*<br>A.C. Anderson<br>S.A. Reible*<br>R.S. Withers   | IEEE Trans. Magn. <b>MAG-23</b> , 895 (1987)   |
| 7260 | Superconductive Delay Line with Integral MOSFET Taps  | M.A. Delaney*<br>R.S. Withers<br>A.C. Anderson<br>J.B. Green<br>R.W. Mountain  | IEEE Trans. Magn. <b>MAG-23</b> , 791 (1987)   |
| 7273 | GaAs Circuit Restructuring by Multilevel Laser-Direct-Written Tungsten Process                                | J.G. Black<br>S.P. Doran<br>M. Rothschild<br>J.H.C. Sedlacek<br>D.J. Ehrlich   | Mat. Res. Soc. Symp. Proc., Vol. <b>75</b> (1987), pp. 651-655, DTIC AD-A187548  |
| 7397 | Fabrication of Submicrometer-Size Structures in Si Using SF <sub>6</sub> /O <sub>2</sub> Reactive Ion Etching | A.R. Forte<br>D.D. Rathman   | Proc. First International Symposium on ULSI Technology, Electrochemical Society, Philadelphia, Pennsylvania, 10-15 May 1987, pp. 251-252 |
| 7556 | On the Applications of Laser-Direct-Writing Techniques to GaAs Monolithic Microwave Integrated Circuits       | C.L. Chen<br>J.G. Black<br>W.E. Courtney<br>S.P. Doran<br>L.J. Mahoney<br>M. Rothschild<br>D.J. Ehrlich<br>R.A. Murphy | Proc. IEEE Gallium Arsenide Integrated Circuit Symposium, Portland, Oregon, 13-16 October 1987, pp. 167-170                              |
| 7704 | Avalanche-induced Drain-Source Breakdown in Silicon-on-Insulator n-MOSFETs                                    | K.K. Young   | 1987 IEEE SOS/SOI Technology Workshop, Durango, Colorado, 6-8 October 1987, p. 82  |

---

\* Author not at Lincoln Laboratory.

## UNPUBLISHED REPORTS

### Journal Articles

#### JA No.

6030	New MBE Buffer Used To Eliminate Backgating in GaAs MESFETs	F.W. Smith A.R. Calawa C.L. Chen M.J. Manfra L.J. Mahoney	Accepted by IEEE Electron Device Lett.
6031	Avalanche-Induced Drain-Source Breakdown in Silicon-on-Insulator n-MOSFETs	K.K. Young J.A. Burns	Accepted by IEEE Trans. Electron Devices
6037	Planar Quantum Wells with Controlled Spatially Dependent Thicknesses and Al Content	W.D. Goodhue J.J. Zayhowski K.B. Nichols	Accepted by J. Vac. Sci. Technol.
6040	Pump Power Minimization for High-Gain CW Laser Amplifiers	A. Walther A. Sanchez	Accepted by Appl. Opt.
6052	Optical Wavefront Measurement and/or Modification Using Integrated Optics	R.H. Rediker T.A. Lind B.E. Burke	Accepted by the Joint Special Issue of J. Lightwave Technol. and IEEE J. Quantum Electron.
6055	Device Applications of Diamonds	M.W. Geis N.N. Efremow D.D. Rathman	Accepted by J. Vac. Sci. Technol.
6057	Laser Patterning of Metal-Oxide Superconductor Films by Reactive Solid-State Transformation	M. Rothschild J.H.C. Sedlacek J.G. Black D.J. Ehrlich	Accepted by IEEE Electron Device Lett.
6060	Pt-Ir Silicide Schottky-Barrier IR Detectors	B-Y. Tsaur M.M. Weeks* P.W. Pellegrini*	Accepted by IEEE Electron Device Lett.
6065	Reversible Laser Chemically Induced Phase Transformations in Thin-Film $\text{Ba}_2\text{YCu}_3\text{O}_x$	M. Rothschild J.H.C. Sedlacek J.G. Black D.J. Ehrlich	Accepted by Appl. Phys. Lett.

---

\* Author not at Lincoln Laboratory.

## UNPUBLISHED REPORTS

### Meeting Speeches

#### MS No.

6868F	Hot-Jet Etching of GaAs and Si	M.W. Geis N.N. Efremow G.A. Lincoln	Seminar, Rice University, Houston, Texas, 22 January 1988
7004B	Millimeter-Wave Monolithic Circuits for Receiver and Transmitter Applications	C.L. Chen	Seminar, Chinese Institute of Engineers, Taipei, Republic of China, 21 December 1987
7556A	On the Applications of Laser- Direct-Writing Techniques to GaAs Monolithic Microwave Integrated Circuits	C.L. Chen	
7238C	Optics for Computation	P.L. Kelley	Seminar, Northwestern Uni- versity, Evanston, Illinois, 5 November 1987
7434A, B	History and Projection of the Future of Laser Diodes	R.H. Rediker	Lincoln Laboratory Technical Seminars Series, MIT, Cambridge, Massachusetts, 9 December 1987; Elmsford, New York, 19 January 1988
7451C	Progress in Tunable $\text{Ti:Al}_2\text{O}_3$ Lasers	A. Sanchez	Seminar, Boston College, Newton, Massachusetts, 2 December 1987
7472A	CCDs for Real-Time Analog Signal Processing	A.M. Chiang	Seminar, Columbia University, New York, New York, 12 November 1987
7491A	Superconductive Wideband Analog Signal Correlator with Buffered Digital Output	J.B. Green A.C. Anderson R.S. Withers	SPIE O-E/LASE '88 Symposium on Innovative Science and Technology, Los Angeles, California, 10-15 January 1988
7660	Fabrication of Miniature Lenses and Mirrors for InGaAsP/InP Lasers	D. Yap Z.L. Liao J.N. Walpole V. Diadiuk	

\* Author not at Lincoln Laboratory.

MS No.

7609	Monolithic Two-Dimensional GaInAsP/InP Laser Arrays	Z.L. Liao J.N. Walpole	3rd International Laser Science Conference, Atlantic City, New Jersey, 4 November 1987
7622A	A Comparison of SAW- and CCD-Based Signal Processing	S.C. Munroe D.R. Arsenault R.W. Ralston	IEEE Ultrasonics Society, Boston Chapter, Raytheon Research Laboratory, Lexington, Massachusetts, 20 January 1988
7623	Optical Considerations for Excimer Steppers	M. Rothschild D.J. Ehrlich	Materials Research Society, Boston, Massachusetts, 30 November - 4 December 1987
7625	Laser-Direct-Written Interconnection Techniques for Multiple-Chip and Wafer-Scale Systems	J.G. Black S.P. Doran D.K. Astolfi M. Rothschild D.J. Ehrlich	
7626	Liquid-Solid Interface Morphologies and Defect Structures in Zone-Melting-Recrystallized Silicon-on-Insulator Films	J.S. Im* C.K. Chen C.V. Thompson* H. Tomita* M.W. Geis	
7685	Normal State Infrared Anisotropy of Polycrystalline $\text{La}_{1.85}\text{Sr}_{0.15}\text{CuO}_{4-y}$	G.L. Doll* J. Steinbeck* G. Dresselhaus* M.S. Dresselhaus* A.J. Strauss H.J. Zeiger	
7693	Magnetic Excitations in $\text{La}_2\text{CuO}_4$	I. Ohana* Y.C. Liu* M.S. Dresselhaus* G. Dresselhaus* P.J. Picone* H. Jenssen* D.R. Gabbe* H.J. Zeiger A.J. Strauss	
7699	RF Surface Resistance of YBaCuO Thin Films	A.C. Anderson B-Y. Tsaur M.S. Dilorio	

\* Author not at Lincoln Laboratory.

**MS No.**

7645A	Superconductive Microwave and High-Speed Circuits	R.S. Withers	Cambridge Conference on Commercial Application of Superconductivity, Boston, Massachusetts, 25 January 1988
7654	Device Applications of Diamonds	M.W. Geis	American Vacuum Society, Anaheim, California, 2-6 November 1987
7656B	Two-Dimensional Surface-Emitting Diode Laser Arrays	R.C. Williamson	Lincoln Laboratory Technical Seminars Series, Madison, Wisconsin, 13 November 1987
7678A	Recent Advances in Solid-State Laser Technology	A. Mooradian	1987/1988 Fall and Spring Seminar Series, GTE Laboratories, Waltham, Massachusetts, 14 January 1988
7702	Emerging Technology for In Situ Processing	D.J. Ehrlich	Seminar on Focused Ion Beam Technology and Applications, Osaka, Japan, 16-20 November 1987
7703	Planar Vias Through Si <sub>3</sub> N <sub>4</sub> Fabricated by Focused Ion Beam Implantation	J. Melngailis T.O. Herndon M.I. Shepard* H. Lezec*	
7732	GaAs Epitaxy on Si for GaAs Si Integration	S.J. Eglash	
7756A	High-Frequency Device Applications of Superconductive Electronics	J.B. Green	Industrial Liaison Program on High-Temperature Superconductivity, MIT, Cambridge, Massachusetts, 26 January 1988
7819	Deposition and Characterization Techniques for Low RF Loss in Films	A.C. Anderson	

---

\* Author not at Lincoln Laboratory.

**MS No.**

7765 Focused Ion Beam Implantation

H. Lezec\*  
L.J. Mahoney  
M.I. Shepard\*  
J. Melngailis

Seminar, VLSI Review, MIT,  
Cambridge, Massachusetts,  
14 December 1987

7771 A Tunable Solid-State Laser:  
Titanium-Doped Sapphire

K.F. Wall

Seminar, Worcester  
Polytechnic Institute,  
Worcester, Massachusetts,  
14 December 1987

---

\* Author not at Lincoln Laboratory.

## ORGANIZATION

### SOLID STATE DIVISION

A.L. McWhorter, *Head*  
I. Melngailis, *Associate Head*  
E. Stern, *Associate Head*  
J.F. Goodwin, *Assistant*

N.L. DeMeo, Jr., *Associate Staff*

### QUANTUM ELECTRONICS

A. Mooradian, *Leader*  
P.L. Kelley, *Associate Leader*  
A. Sanchez-Rubio, *Assistant Leader*

Aggarwal, R.L.	McClung, S.K.
Barch, W.E.	Menyuk, N.
Belanger, L.J.	Mims, V.A.*
Brailove, A.A.	Schulz, P.A.
Daneu, V.	Sciacca, M.D.
DeFeo, W.E.	Seppala, J.P.
Fan, T-Y.	Sharfin, W.F.
Hancock, R.C.	Sullivan, D.J.
Hryniewicz, J.V.	Tapper, R.S.
Jeys, T.H.	Walker, W.A.
Lacovara, P.	Wall, K.F.
Le, H.Q.	Zayhowski, J.J.

### ELECTRONIC MATERIALS

A.J. Strauss, *Leader*  
B-Y. Tsaur, *Associate Leader*  
H.J. Zeiger, *Senior Staff*

Anderson, C.H., Jr.	Kolesar, D.F.
Button, M.J.	Krohn, L., Jr.
Chen, C.K.	Mastromattei, E.L.
Choi, H.K.	Mattia, J.P.
Clark, H.R.	Nitishin, P.M.
Connors, M.K.	Pantano, J.V.
Delaney, E.J.	Tracy, D.M.
Eglash, S.J.	Turner, G.W.
Fahey, R.E.	Wang, C.A.
Finn, M.C.	Young, K.K.
Iseler, G.W.	

### APPLIED PHYSICS

R.C. Williamson, *Leader*  
D.L. Spears, *Assistant Leader*  
R.H. Rediker, *Senior Staff*

Aull, B.F.	Hovey, D.L.	Pang, L.Y.†
Betts, G.E.	Johnson, L.M.	Rauschenbach, K.
Bossi, D.E.†	Ketteridge, P.A.	Reeder, R.E.
Corcoran, C.J.†	Kim, S-M.†	Roussell, H.V.
Cox, C.H., III	Shiple, S.D.†	Seielstad, D.A.
Diadiuk, V.	Liau, Z.L.	Tsang, D.Z.
Donnelly, J.P.	Lind, T.A.	Walpole, J.N.
Ferrante, G.A.	O'Donnell, F.J.	Woodhouse, J.D.
Groves, S.H.	Palmacci, S.T.	Yap, D.†
Harman, T.C.	Palmateer, S.C.	Yee, A.C.

---

\* Staff Associate

† Research Assistant

## ANALOG DEVICE TECHNOLOGY

R.W. Ralston, *Leader*

R.S. Withers, *Associate Leader*

Anderson, A.C.  
Arsenault, D.R.  
Bhushan, M.  
Boisvert, R.R.  
Brogan, W.T.  
Denneno, A.P.  
Dolat, V.S.  
Fitch, G.L.

Frickey, J.M.  
Green, J.B.  
Holtham, J.H.  
Lattes, A.L.  
Lichtenwalner, D.J.\*  
Macedo, E.M., Jr.  
Munroe, S.C.  
Oates, D.E.

Pan, J.Y.\*  
Sage, J.P.  
Seidel, M.N.\*  
Slattery, R.L.  
Steinbeck, J.W.  
Thompson, K.E.  
Wong, S.C.\*

## MICROELECTRONICS

W.T. Lindley, *Leader*

R.A. Murphy, *Associate Leader*

E.D. Savoye, *Associate Leader*

D.J. Ehrlich, *Assistant Leader*

B.B. Kosicki, *Assistant Leader*

Astolfi, D.K.  
Bales, J.W.\*  
Bennett, P.C.  
Black, J.G.  
Bozler, C.O.  
Brown, E.R.  
Burke, B.E.  
Calawa, A.R.  
Chen, C.L.  
Chiang, A.M.  
Clifton, B.J.  
Daniels, P.J.  
Doherty, C.L., Jr.  
Doran, S.P.  
Durant, G.L.  
Efremow, N.N., Jr.  
Felton, B.J.  
Gajar, S.A.\*  
Geis, M.W.

Goodhue, W.D.  
Gray, R.V.  
Gregory, J.A.  
Hollis, M.A.  
Huang, J.C.M.  
Johnson, B.W.  
Johnson, K.F.  
LaFranchise, J.R.  
LeCoz, Y.L.\*  
Lincoln, G.A., Jr.  
Lyszczarz, T.M.  
Mahoney, L.J.  
Maki, P.A.  
Manfra, M.J.  
Mathews, R.H.  
McGonagle, W.H.  
McIntosh, K.A.  
Melngailis, J.†  
Mountain, R.W.

Nichols, K.B.  
Pang, S.W.  
Parker, C.D.  
Pichler, H.H.  
Rabe, S.  
Rathman, D.D.  
Reich, R.K.  
Reinold, J.H., Jr.  
Rooks, M.J.  
Rothschild, M.  
Sedlacek, J.H.C.  
Smith, F.W.\*  
Smythe, D.L., Jr.  
Sollner, T.C.L.G.  
Uttaro, R.S.  
Vera, A.  
Wilde, R.E.  
Young, E.M.

---

\* Research Assistant

† Part Time

## 1. SOLID STATE DEVICE RESEARCH

### 1.1 INTEGRATED-OPTICAL $2 \times 2$ SWITCH WITH Y-BRANCH MODE SPLITTERS

We recently completed an initial demonstration of a  $2 \times 2$  switch<sup>1</sup> consisting of a Mach-Zehnder interferometric modulator and asymmetric Y-branch mode splitters. This switch design does not contain directional couplers which have critical fabrication tolerances, nor does it contain active mode splitters which require large drive voltages. In this initial device we have demonstrated switching at a wavelength of  $1.15 \mu\text{m}$  with crosstalk of less than  $-15 \text{ dB}$ .

A schematic illustration of the switch is shown in Figure 1-1. The Mach-Zehnder interferometric modulator is connected to the input and output asymmetric Y-branches by short double-mode waveguide sections. The asymmetric Y-branches function as mode splitters combiners.<sup>1</sup> As the waveguides in the Y-branches become more separated and hence more decoupled, the fundamental and second-order mode powers of the structure become increasingly concentrated in the wide guide and the narrow guide, respectively. For small branch angles, the structure is adiabatic. Therefore, light entering the device through the wide guide couples into the fundamental mode of the double-mode guide and light entering the narrow guide couples into the second-order mode. Increasing the branch angle results in higher cross-coupling between the two modes. The Mach-Zehnder interferometric modulator acts as a mode converter to achieve switching. The bar and cross states of the switch are shown in Figures 1-1(a) and (b), respectively. In the bar state, with zero applied voltage, it is assumed there is no induced optical phase shift between the two arms of the interferometer. Therefore, light entering the wide input guide of the device remains in the fundamental mode following the interferometer and couples into the wide output guide. Similarly, light entering the narrow input guide couples into the narrow output guide. In the cross state, a voltage of  $V_\pi$  is applied to the modulator electrodes, resulting in an optical phase shift difference of  $\pi$  radians between the two arms of the interferometer. Light incident on the interferometer in the fundamental mode couples into the second-order mode at the interferometer output and light incident in the second-order mode couples into the fundamental mode. Cross-state switching is therefore achieved. The relative amounts of bar-state and cross-state output power varies sinusoidally with the modulator drive voltage.

A key feature of this switch is the separation of the passive mode splitter from the active mode converter. The mode converter can therefore be designed to optimize switching speed and drive voltage independently of crosstalk requirements. Another advantage of this switch is the lack of critical fabrication tolerances. However, the mode-splitter branch angles must be no greater than that which results in the maximum allowable crosstalk.

The experimental device was fabricated for operation at  $1.15 \mu\text{m}$ . Titanium strips  $600 \text{ \AA}$  thick were diffused into X-cut  $\text{NiNbO}_3$  for 6 h at  $1050^\circ\text{C}$  in flowing  $\text{O}_2$  and water vapor. The waveguide dimensions were  $W_1 = 6.0 \mu\text{m}$ , and  $W_2 = 4.0 \mu\text{m}$ , and  $W = 5.0 \mu\text{m}$ . The branch angle  $\theta$  of the interferometer was  $1^\circ$  for all devices while the angle  $\phi$  for the mode splitters ranged

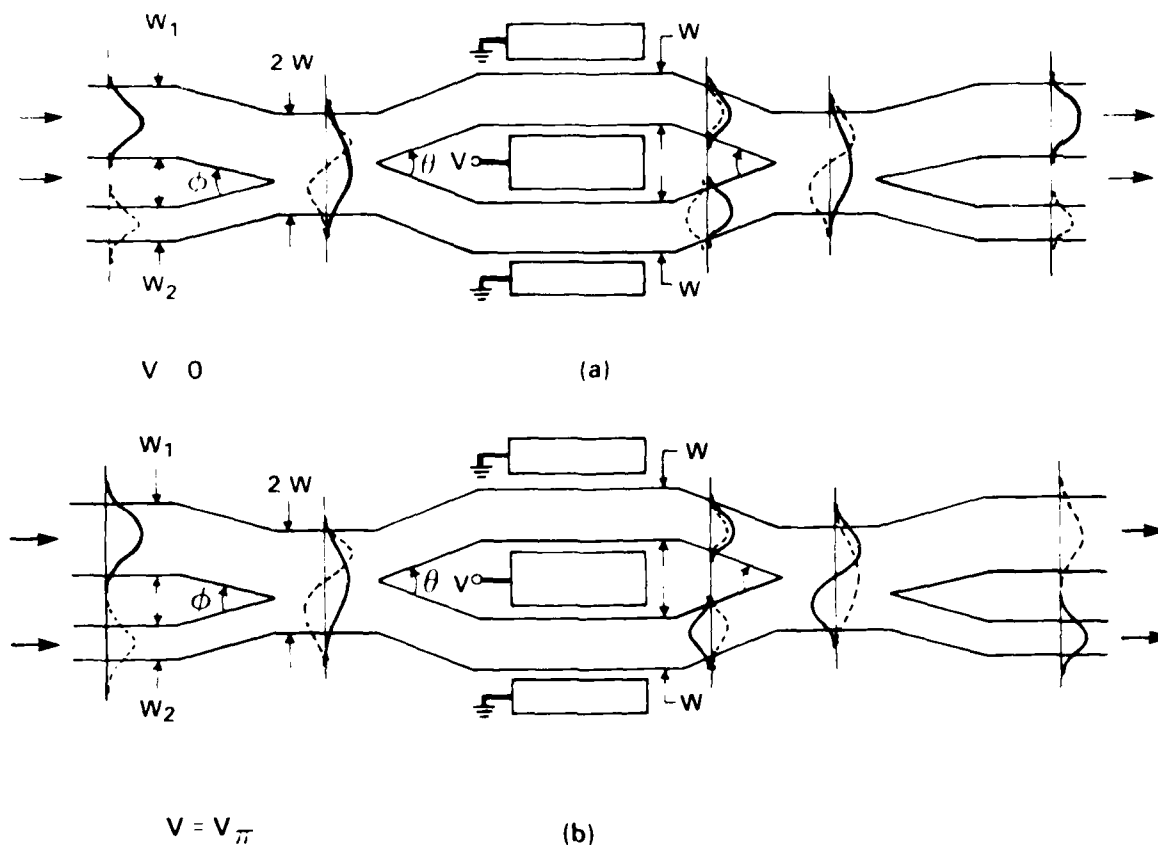


Figure 1-1. Schematic illustration of the  $2 \times 2$  switch in the (a) bar state, and (b) cross state. For both cases, the field profiles of light incident on the wide and narrow input guides as it traverses through the switch are shown by solid and dashed lines, respectively.

from  $0.2$  to  $1.0^\circ$ . The center-to-center spacing between the input and output waveguides was  $20\text{ }\mu\text{m}$ . The modulator electrodes were fabricated of evaporated Au and were  $5\text{ mm}$  long with a  $7\text{-}\mu\text{m}$  gap. The total device length was  $4\text{ cm}$  with waveguide propagation in the Y direction of the  $\text{LiNbO}_3$ .

The device was tested by endfire coupling TE-polarized light from a  $1.15\text{-}\mu\text{m}$  HeNe laser. The crosstalk levels were minimized for both the bar and cross states by adjusting the electrode voltage with light coupled successively into each of the two input guides. The measurements for the device with the  $0.2^\circ$  branch angle are summarized in Table 1-1. The switching voltage was  $5.8\text{ V}$ . The lowest crosstalk was  $-18.5\text{ dB}$  for the bar state with input light coupled into the  $67\text{-}\mu\text{m}$  input guide. The lower output powers associated with the  $4\text{-}\mu\text{m}$  guides are a result of the reduced coupling efficiency for this guide width. It is likely that this effect can be nearly eliminated by tapering the input and output guide widths. The switch insertion loss was less than

<b>TABLE 1-1</b> <b>Experiment Performance of Integrated-Optical <math>2 \times 2</math> Switch</b> <b>at <math>\lambda = 1.15 \mu\text{m}</math> for Cross (<math>\times</math>) and Bar (<math>=</math>) States</b>				
Input Guide	Switch State	4- $\mu\text{m}$ Output*	6- $\mu\text{m}$ Output*	Crosstalk (dB)
6 $\mu\text{m}$	$\times$	1750	55	-15.0
	=	35	2500	-18.5
4 $\mu\text{m}$	$\times$	35	1200	-15.4
	=	840	20	-16.2

\* Output power in arbitrary units.

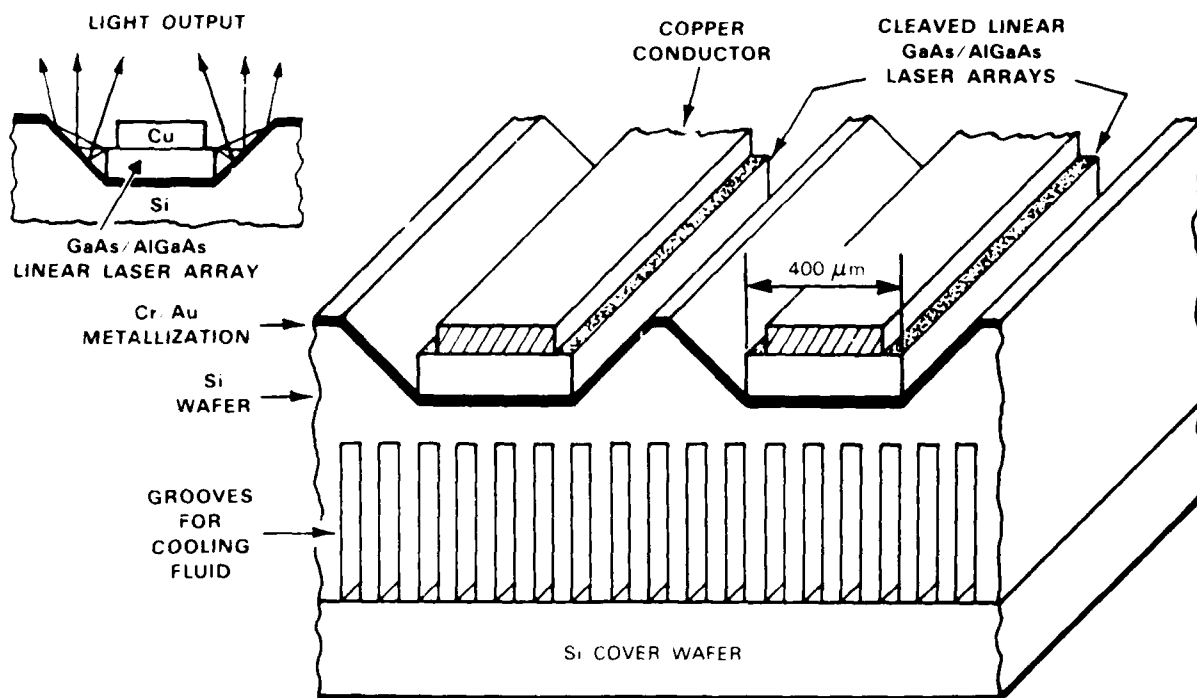
1.5 dB relative to straight guides fabricated on the same substrate. Devices with larger mode-splitter branch angles were also characterized and had higher crosstalk levels. With a branch angle of  $0.4^\circ$ , the minimum crosstalk was -10 dB. It should be possible to reduce the crosstalk to less than -20 dB by using branch angles smaller than  $0.2^\circ$ .

L.M. Johnson  
H.V. Roussell

## 1.2 HYBRID APPROACH TO SURFACE-EMITTING TWO-DIMENSIONAL DIODE LASER ARRAYS

We report a new hybrid approach to two-dimensional surface-emitting diode laser arrays that takes advantage of both the advanced state of development of linear laser arrays with conventional cleaved end facets<sup>2,3</sup> and the rapid development of Si heat sink technology.<sup>4-6</sup> The complete design for a high-power CW two-dimensional laser array is illustrated in Figure 1-2. The Si substrate provides both high-quality  $45^\circ$  beam deflectors and efficient microchannel heatsinking. For this initial demonstration of the hybrid approach, arrays were fabricated without the cooling fluid slots in the Si substrate and the Cu conductors on top of each linear array. However, we have demonstrated these omitted features in separate work<sup>6</sup> and it appears that their inclusion in future arrays should be straightforward. The cooling fluid slots can be cut on a standard dicing saw,<sup>6</sup> and therefore orientation is not a consideration for their inclusion.

The flat bottom grooves with  $45^\circ$  sidewalls are etched in (100) Si using standard photolithography and an orientation selective etch. A strip pattern oriented in a (013) direction is first defined in a  $\text{Si}_3\text{N}_4$  capping layer, which serves as an etch mask. The Si is then etched in a KOH, isopropanol,  $\text{H}_2\text{O}$  solution at  $80^\circ\text{C}$ . The bottom (100) Si plane etches about 2.5 times



96005-2

Figure 1-2. Schematic illustration of hybrid two-dimensional surface-emitting diode laser array.

faster than the (331) sidewalls, which are theoretically at an angle of  $46.5^\circ$  to the (100) surface. A sawed cross section of an etched groove is shown in Figure 1-3(a). The bottom is flat and parallel to the top surface and the sidewalls are approximately  $45^\circ$  to bottom and top surfaces. For the hybrid laser arrays reported here, the grooves are about  $210\text{ }\mu\text{m}$  deep and the bottoms of the grooves are approximately  $400\text{ }\mu\text{m}$  long. The surface of the etched Si wafer is metallized with Cr Au. Figure 1-3(b) shows a top view of a test GaAs/AlGaAs linear bar array mounted in a metallized groove. Reflections of the cleaved end facets of the GaAs/AlGaAs bar are visible in the  $45^\circ$  deflecting mirrors.

The GaAs/AlGaAs wafer used to make the laser arrays contained a single quantum well symmetrically positioned in a large optical cavity. Organometallic vapor phase epitaxy was used to grow the following epitaxial layers on a (100) Si-doped  $n^+$  GaAs substrate:  $1.8\text{-}\mu\text{m}$   $n^+$   $\text{Al}_{0.6}\text{Ga}_{0.4}\text{As}$  confinement,  $0.32\text{-}\mu\text{m}$   $n$   $\text{Al}_{0.3}\text{Ga}_{0.7}\text{As}$ ,  $0.02\text{-}\mu\text{m}$  undoped GaAs active,  $0.32\text{-}\mu\text{m}$   $p$   $\text{Al}_{0.3}\text{Ga}_{0.7}\text{As}$ ,  $1.5\text{-}\mu\text{m}$   $p$   $\text{Al}_{0.6}\text{Ga}_{0.4}\text{As}$  confinement and  $0.2\text{-}\mu\text{m}$   $p^+$  GaAs contacting. The two  $0.32\text{-}\mu\text{m}$   $\text{Al}_{0.3}\text{Ga}_{0.7}\text{As}$  layers on either side of the active layer form the large optical cavity.

The linear arrays made from the wafer consisted of proton-defined  $40\text{-}\mu\text{m}$ -wide stripe lasers on  $250\text{-}\mu\text{m}$  centers. The proton bombardment used to define the laser stripes penetrated to a depth approximately  $0.2\text{ }\mu\text{m}$  above the top of the large optical cavity (i.e., above the top of the p

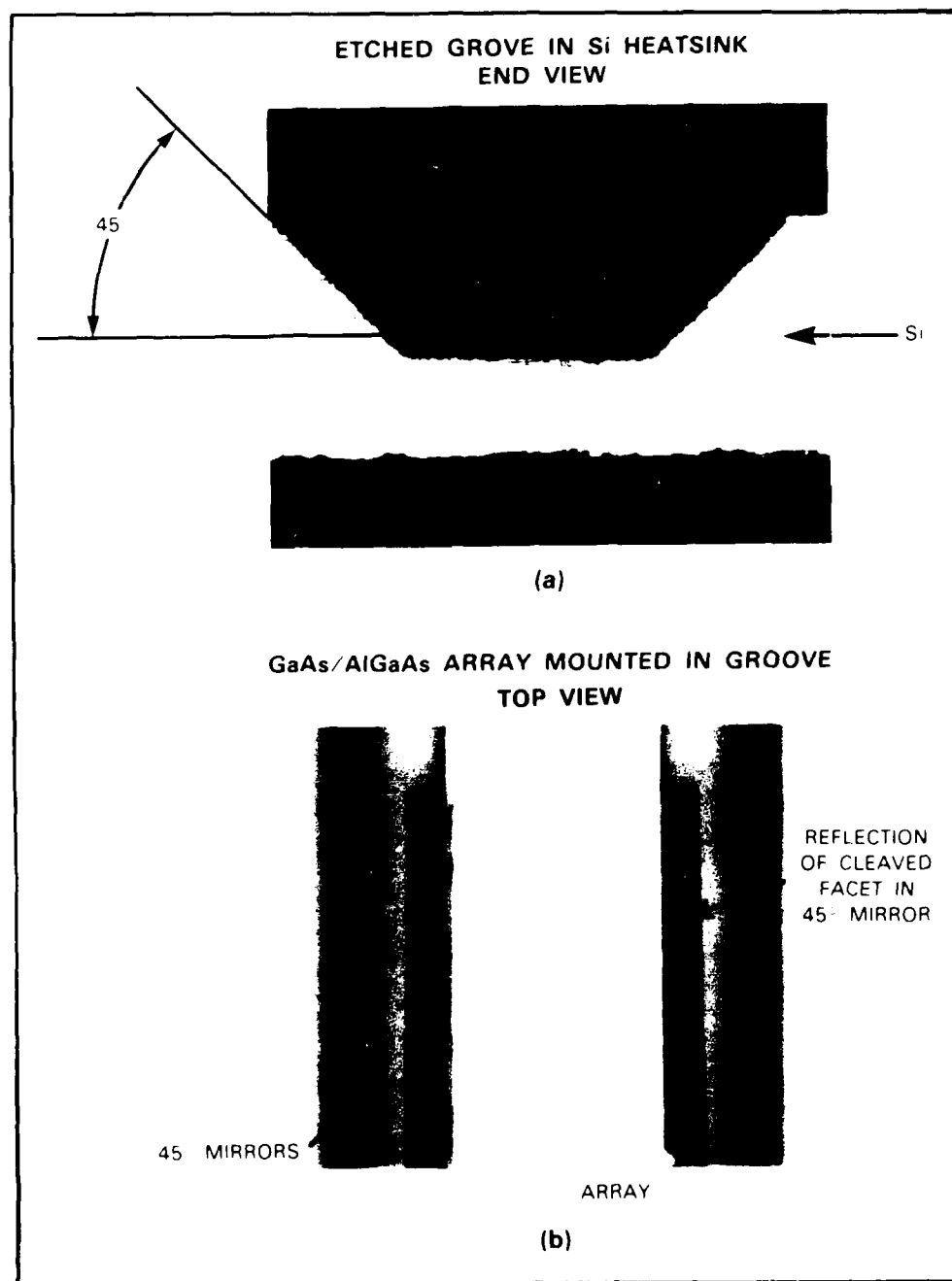


Figure 1-3. (a) Sawed cross section of groove etched in Si with flat bottom and 45° sidewalls. (b) Top view of linear laser array mounted in metallized Si groove. Reflections of the cleaved end facets of the GaAs/AlGaAs linear bar array can be seen in the 45° deflecting mirrors.

$\text{Al}_{0.3}\text{Ga}_{0.7}\text{As}$  layer). An additional proton bombardment at higher energies was performed to introduce sufficient optical loss in  $10\text{-}\mu\text{m}$ -wide stripes midway between the lasers to suppress lasing in the transverse direction. The wafer was then thinned to about  $75\text{ }\mu\text{m}$  and an ohmic contact made to the  $\text{n}^+$  GaAs substrate. Linear bar arrays with  $400\text{-}\mu\text{m}$ -long laser cavities were then cleaved from the wafer. Several of these arrays were tested using  $100\text{-ns}$  current pulses at a repetition rate of  $1\text{ kHz}$ . The average threshold current per  $40\text{-}\mu\text{m}$ -wide stripe laser was approximately  $120\text{ mA}$  and the measured differential quantum efficiencies per facet were consistently greater than 30 percent. The cone angle of the laser emission (full width at half maximum) in the vertical direction was about  $41^\circ$ .

Several linear bar arrays approximately  $4\text{ mm}$  wide and containing 15 to 16 lasers were mounted in the metallized grooves etched in a Si substrate. The hybrid array was then mounted on a header and wires bonded to the top of each bar array from both ends. Each bar in the array could be driven separately or any combination in parallel. The near-field pattern of the laser emission from a hybrid array, consisting of three linear GaAs/AlGaAs bar arrays mounted in three Si grooves, is shown in Figure 1-4. Although there is some nonuniformity due to high series resistance along the top of each bar, the output from the middle (Bar 2) and bottom (Bar 3) arrays appear similar to the outputs obtained directly from the cleaved end facets, which indicates that the reflections off the  $45^\circ$  mirrors are well behaved. The series resistance can be

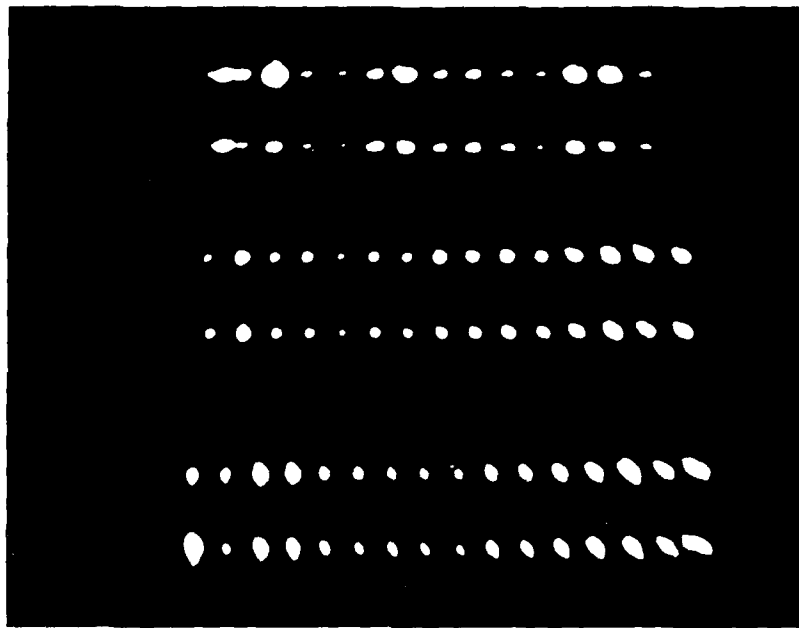


Figure 1-4. Near-field pattern of a hybrid two-dimensional surface-emitting laser array consisting of three  $4\text{-mm}$ -wide GaAs/AlGaAs linear bar arrays mounted in three separate grooves on a common Si substrate.

96005-4

reduced significantly by using a conducting bar on top of each linear array as illustrated in Figure 1-2 or by plating thick contact stripes along the top of each linear array. There is some scattering apparent in the output of the top array (Bar 1) due both to several mirror defects in the linear bar array itself and to some bonding material on the cleaved laser facets and deflecting mirrors.

The pulsed power out of this hybrid array was measured with all three linear bar arrays driven in parallel and with each driven separately. Because of limitation in current available from the pulser, it was necessary to drive the linear arrays one at a time to obtain high output powers. The output power vs pulsed current obtained from each of the bars driven separately is shown in Figure 1-5. Approximately 10 W of peak power perpendicular to the array surface was obtained from each bar with currents in the 11 to 13 A range. The total threshold current of Bar 3, which contained 16 lasers, was about 1.6 A for an average threshold current per laser of 100 mA, while that of Bar 1, which contained 15 lasers, was about 2.4 A for an average threshold current per laser of 160 mA. The total differential quantum efficiency of Bar 3 was about 70 percent, while that of Bar 1 was about 65 percent. These high differential quantum efficiencies indicate that the 45° metallized Si mirrors are deflecting essentially all of the light emitted from the laser facets.

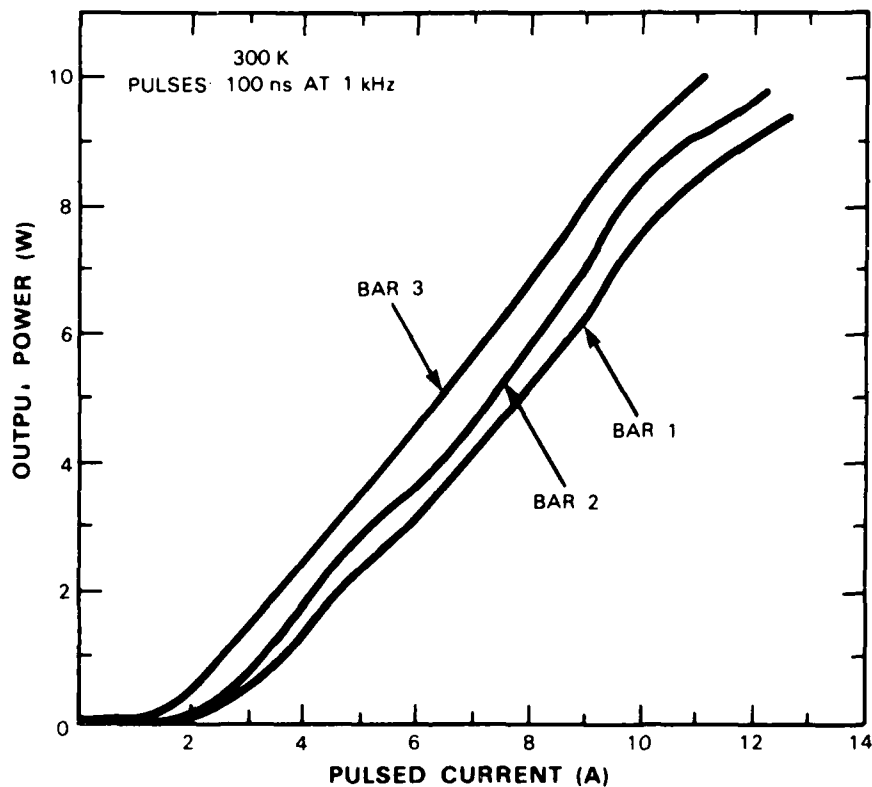


Figure 1-5. Power output vs pulsed current of the three-laser-bar hybrid array whose near-field pattern is shown in Figure 1-4. Here, each bar was driven separately.

This hybrid approach can be used with other semiconductor lasers in addition to the GaAs AlGaAs lasers illustrated here. Arrays are limited in size only by the size of the Si substrates. It should be possible with this hybrid approach to reduce the current requirements of large arrays by using high-resistivity Si substrates and/or selective oxides and metallization to electrically insulate the linear laser arrays from each other and then drive them in series or some parallel series combination. Also high-power CW operation of these arrays should be possible by incorporating an integral microchannel heat sink in the bottom of the Si substrate, as was shown in Figure 1-2.

J.P. Donnelly  
C.A. Wang

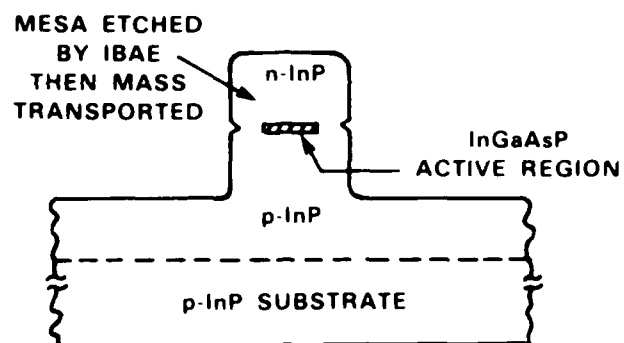
G.A. Simpson  
K. Raushenbach

### **1.3 HIGH-PERFORMANCE InGaAsP/InP BURIED-HETEROSTRUCTURE LASERS DEFINED BY ION-BEAM-ASSISTED ETCHING**

A dry etching technique, ion-beam-assisted etching (IBAE),<sup>7</sup> has been used to define the stripes of InGaAsP/InP mass-transported buried-heterostructure (MTBH) lasers. Previous MTBH lasers were defined by wet-chemical etching.<sup>8,9</sup> The present IBAE-defined lasers have a new, deeply etched rectangular mesa that has resulted in low current leakage, smooth far-field patterns and uniform device characteristics. They also have threshold currents and differential quantum efficiencies that are comparable with state-of-the-art devices. This is the first report of InGaAsP/InP BH laser stripes defined by dry etching.

The structure of our IBAE-defined MTBH laser is illustrated in Figure 1-6(a). Note that the laser mesa has a rectangular shape and is fairly narrow. (Typical mesa widths are 2 to 4  $\mu\text{m}$ .) The use of rectangular mesas offers several advantages such as improved dimensional control and uniformity of device characteristics, since the active-region width does not vary with the thickness of the InP cap layer. This thickness variation is especially evident in LPE-grown heterostructures. The rectangular shape of the mesa also permits smaller spacings between adjacent stripes when fabricating multiple-stripe arrays. A novel feature of our new laser structure is that the rectangular mesas extend well below the active layer towards the substrate, typically by several micrometers. This feature offers the added advantage of reducing the current leakage since the current is directed perpendicular to the junction. Thus, there is less lateral voltage build-up along the p-n homojunctions adjacent to the active region, which allows the transported InP regions on either side of the active region to be much wider.<sup>9,10</sup>

The fabrication procedure used in making our new lasers is similar to that used in making our other p-substrate MTBH lasers,<sup>8,9</sup> with the exception that the mesas were etched by IBAE. The etching was carried out by chlorine gas, at a partial pressure of about  $1.5 \times 10^{-4}$  Torr, with an incident 500-eV argon ion beam at a current density of about  $80 \mu\text{A}/\text{cm}^2$ . The samples were kept at approximately  $190^\circ\text{C}$  during the etching. After the mesas were defined, a short wet-chemical etch was used to remove any damage produced by the ion bombardment. Then, channels were etched into the InGaAsP active layer from both sides with a selective chemical etchant.



(a)



IBAE-DEFINED LASER MESA  
AFTER MASS TRANSPORT

(b)

Figure 1-6. IBAE-defined MTBH lasers before metallization. (a) Schematic cross-sectional view. (b) SEM perspective view.

The channels were refilled to bury the active region by mass transport of InP at a temperature of approximately 620°C for 30 min. Figure 1-6(b) shows an SEM photograph of a laser mesa after etching and mass transport. A stain has been used to reveal the quaternary regions. The active region is approximately 1.5  $\mu\text{m}$  wide. The slight roughness seen in the sidewalls is due primarily to roughness in the photomask and has been considerably smoothed by the mass transport.

The fabricated lasers have excellent operating characteristics. The room-temperature CW threshold currents of five adjacent devices range from 11.5 to 12.5 mA and the differential quantum efficiencies just above threshold are between 32 and 34 percent per facet, as shown in Figure 1-7(a). These lasers have a 0.12- $\mu\text{m}$ -thick active region and are 290  $\mu\text{m}$  long. The average threshold current of 40 devices with lengths between 185 and 480  $\mu\text{m}$  is 13.6 mA, with 95 percent of the devices having threshold currents between 12 and 16 mA. The performance of the IBAE-defined devices compares well with that of the best conventional mass-transported lasers and other types of BH lasers. Furthermore, the uniformity in the L-I characteristics is better than what we have observed in most of our previous devices.

Pulsed excitation was used to investigate the device performance without the effects of heating. The pulsed L-I characteristic from a device is shown in Figure 1-7(b). An output power of 31.5 mW was obtained and was limited only by the drive current available. Note that the L-I

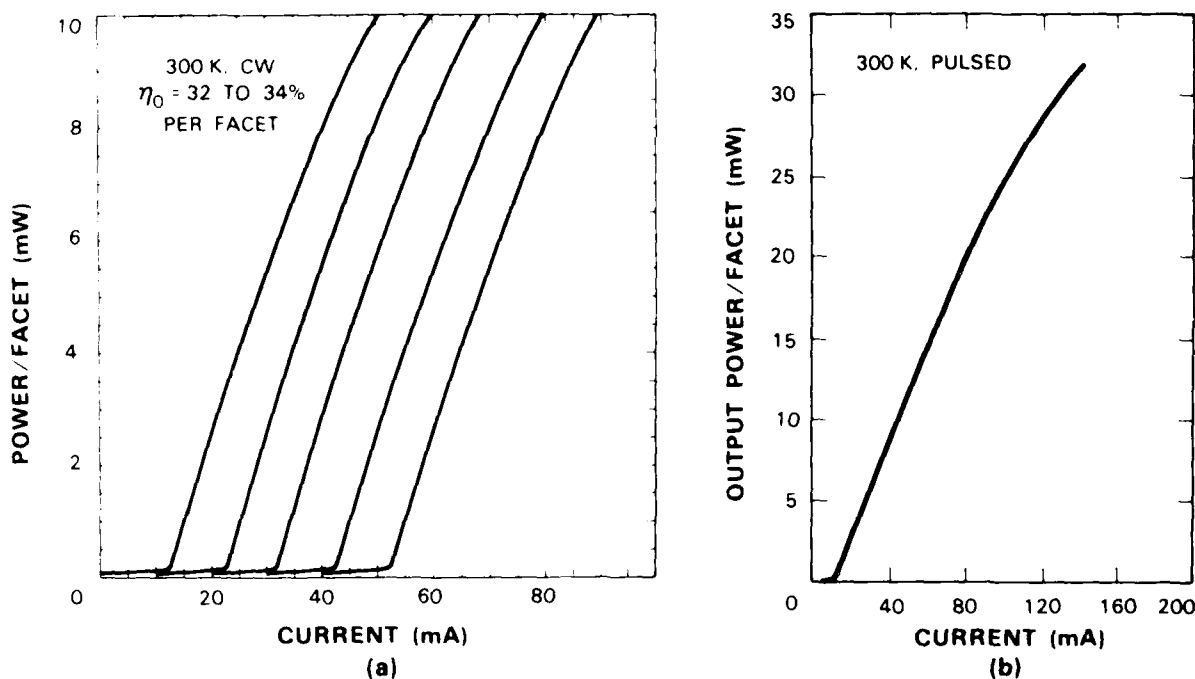


Figure 1-7. Room-temperature, light-current characteristics of IBAE-defined MTBH lasers. (a) CW characteristics of five adjacent lasers, with the horizontal scale shifted by 10 mA for each device, and (b) pulsed characteristic of a single laser.

characteristic remains substantially linear for outputs up to 20 mW. A measure of the current leakage is obtained by noting the drive current at which the leakage current (the departure from linear L-I characteristic) is 1 mA.<sup>10</sup> For this device, the value is around 60 mA. This is comparable to the best results we have obtained from previous lasers, and those particular lasers had much narrower ( $<0.5 \mu\text{m}$ ) transported regions than the present devices.

Typical far-field patterns of an IBAE-defined MTBH laser are shown in Figure 1-8. The far-field patterns are very smooth and have beam divergences of  $30^\circ$  FWHM which do not vary with the drive current. The smoothness of the far-field patterns suggests that there is little scattering from the sidewalls of the stripes. Such smooth patterns have not been obtained for our previous MTBH lasers fabricated on p-type substrates.<sup>9</sup>

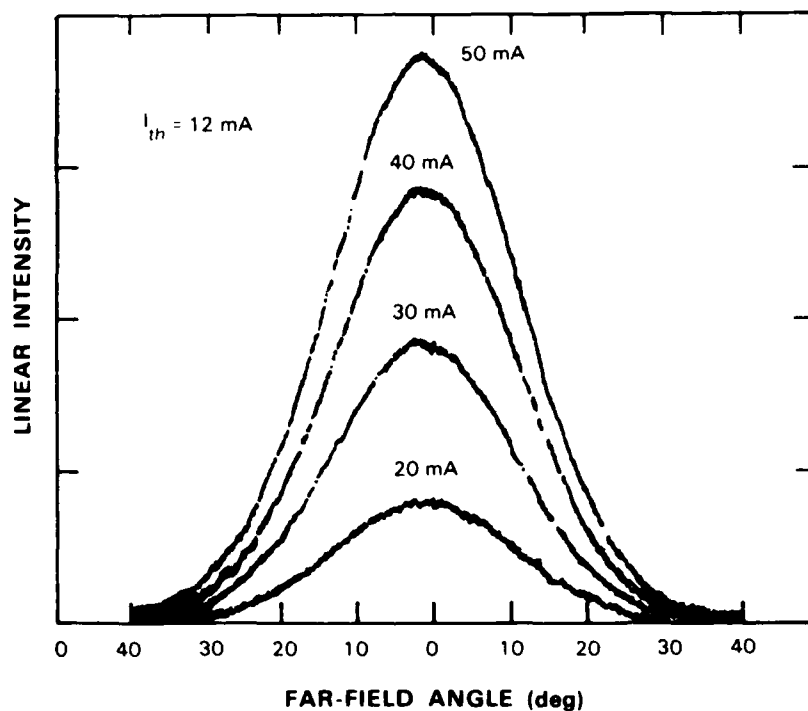


Figure 1-8. Far-field patterns in the junction plane measured at four current levels.

The low threshold currents, high differential quantum efficiencies and smooth far-field patterns obtained with these InGaAsP/InP MTBH lasers indicate the high quality of the IBAE-defined structures. Since vertical sidewalls are obtained in all crystallographic directions, the laser stripes could be fabricated concurrently with etched and mass-transported end-mirrors.<sup>11</sup> This should improve control of the fabrication and allow structures to be aligned along any direction on the substrate.

D. Yap  
Z.L. Liao

D.Z. Tsang  
J.N. Walpole

#### 1.4 BURIED-HETEROSTRUCTURE DIODE LASERS EMITTING AT 1.4 $\mu\text{m}$

Growth, fabrication and testing of InGaAsP/InP double-heterostructure diode lasers emitting at a wavelength of 1.4  $\mu\text{m}$  have been successfully carried out. This work is motivated by the fact that the 1.4- $\mu\text{m}$  wavelength is harmless to the human eye.

As a first step, it was necessary to determine the composition of the liquid-phase epitaxial (LPE) growth solution in equilibrium with the  $\text{In}_{0.67}\text{Ga}_{0.33}\text{As}_{0.73}\text{P}_{0.27}$  alloy at the growth temperature. This quaternary has a bandgap corresponding to a wavelength of 1.4  $\mu\text{m}$  and a lattice constant equal to that of InP. Double crystal x-ray diffractometry was used to establish the lattice matching to  $\Delta a/a \leq 1 \times 10^{-4}$ . After successful growth of the 1.4- $\mu\text{m}$  alloy on an LPE-grown InP buffer layer on an InP substrate, its "meltback" behavior was tested under the solution used to grow the InP cap layer of the double heterostructure. The thin, 1500-Å alloy layer was found to stay intact, a behavior similar to the  $\lambda = 1.3\text{-}\mu\text{m}$  alloy rather than the  $\lambda = 1.5\text{-}\mu\text{m}$  alloy. The scanning electron micrograph of Figure 1-9, showing a thin alloy layer between the InP buffer and cap layers, is evidence of the high quality of the double-heterostructure interfaces with the 1.4- $\mu\text{m}$  alloy. Therefore, growth of a simple, three-layer structure is possible, without the need for

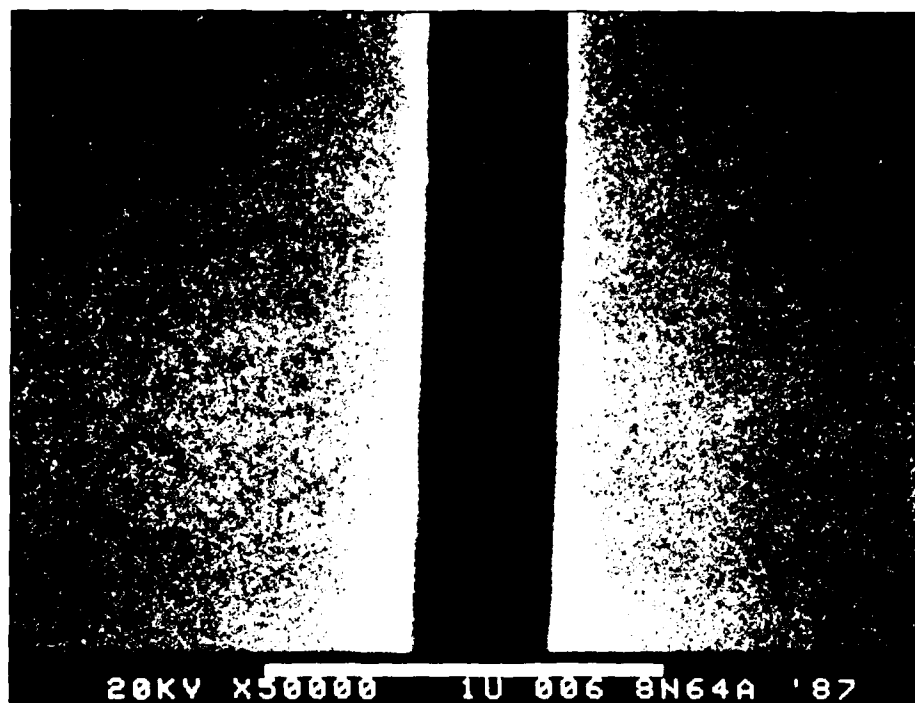


Figure 1-9. SEM micrograph showing high quality interfaces between the  $\lambda = 1.4\text{-}\mu\text{m}$  alloy and the p-type InP buffer layer and the n-type InP cap layer. There is no evidence of dissolution of the alloy into the InP growth solution.

an "anti-meltback" layer of intermediary alloy composition. [In the course of this investigation, it was determined that the LPE buffer layer is necessary if a continuous film of the alloy is to be grown. This observation applies to the situation of low supercooling (3 to 5°C) of the alloy growth solution, which is typically used to give a low growth rate and, consequently, adequate control of the thickness of the thin alloy layer.]

Fabrication of the buried-heterostructure lasers followed the procedures used for the  $\lambda = 1.3\text{-}\mu\text{m}$  devices. Etch rates and etched-surface morphology were determined to be similar to those of the  $\lambda = 1.3\text{-}\mu\text{m}$  structures. The mass-transport technique used to produce a buried active layer was found to work equally well for this composition of the quaternary layer, as expected since the transport involves primarily the InP layers.

Several wafers were used to fabricate single-element and linear arrays of lasers operating at  $\lambda = 1.4\text{ }\mu\text{m}$ . These devices exhibited low threshold currents ( $\leq 10\text{ mA}$ ) and high output power. A representative light output vs current curve is shown in Figure 1-10 for a device without antireflection (AR) coating. After AR coating one of the facets, lasing action was eliminated, but when

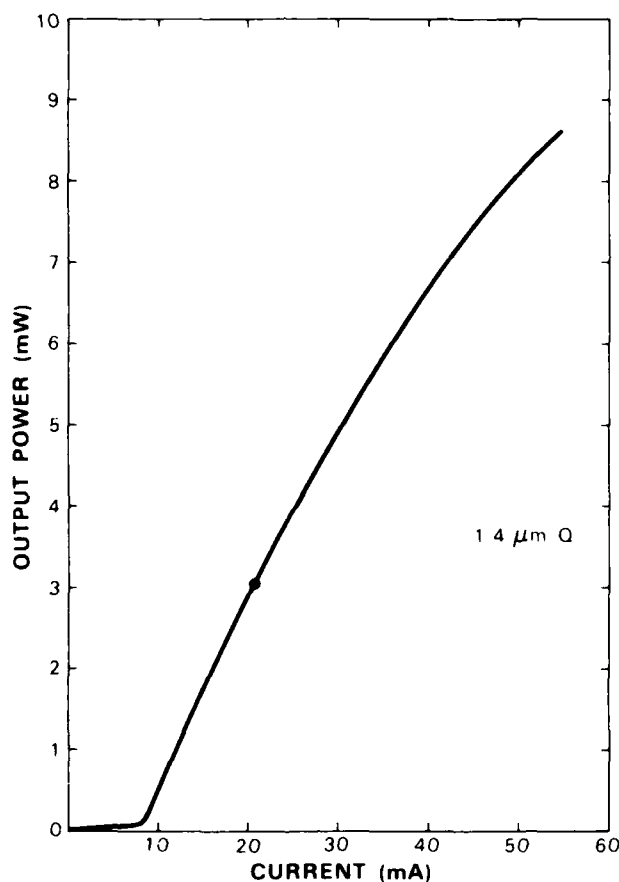


Figure 1-10. Optical power vs current before AR coating. Solid circle indicates current at which spectrum shown in Figure 1-11 was recorded.

the device was operated in an external cavity, the threshold current was brought back to within 10 percent of the value before AR coating. A typical wavelength spectrum for these devices is shown in Figure 1-11. The mode pattern is similar to that of the  $\lambda = 1.3\text{-}\mu\text{m}$  quaternary devices, other than, of course, the shifted wavelength.

V. Diadiuk  
S.H. Groves  
Z.L. Liao

M.C. Plonko  
J.N. Walpole

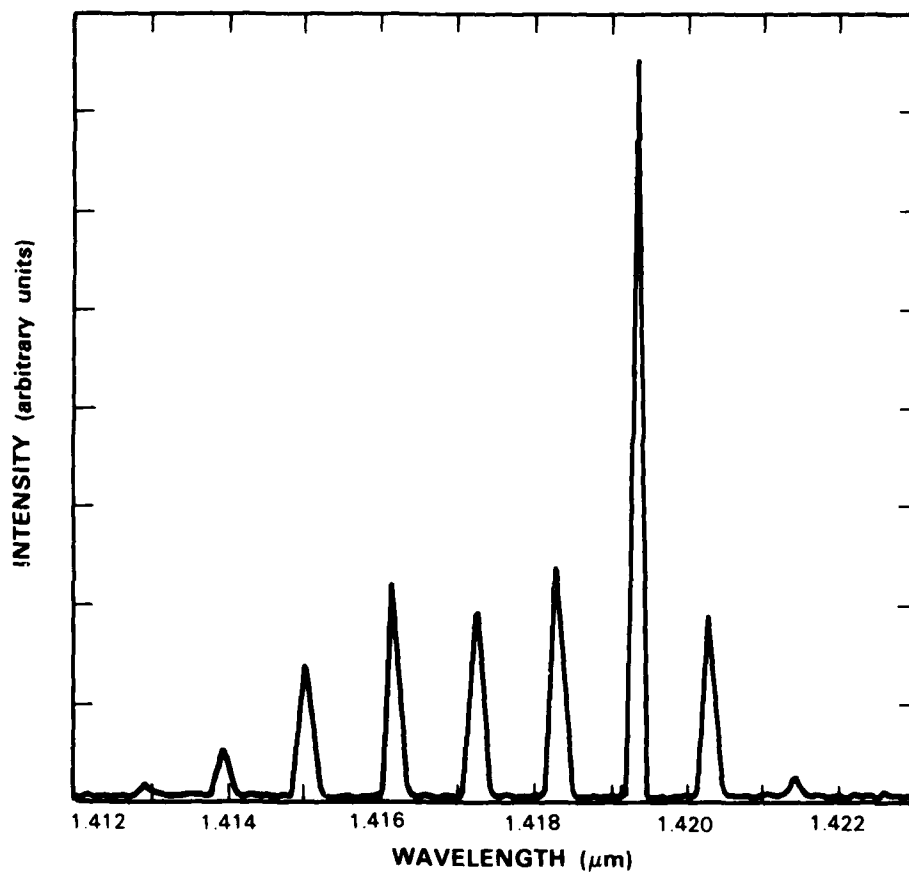


Figure 1-11. Typical mode spectrum of the  $\lambda = 1.4\text{-}\mu\text{m}$  lasers.

96006-11

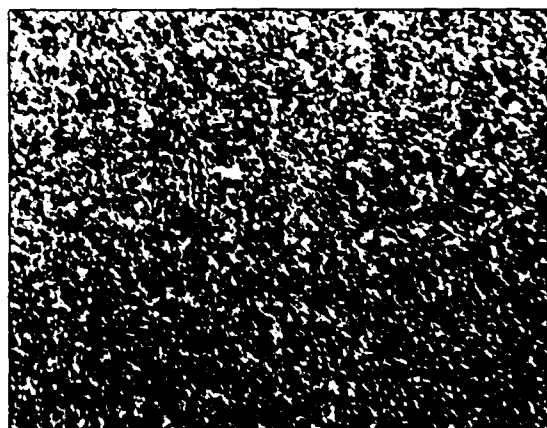
## 1.5 GROWTH OF InP ON GaAs BY OMVPE

We report on a technique which has been useful for establishing deposition uniformity over large areas in an organometallic vapor phase epitaxial (OMVPE) reactor, designed for growth of the InGaAsP/InP materials. The technique involves the growth of InP on GaAs substrates. This structure takes advantage of the low cost of GaAs substrates (compared to that of InP) and the differences in the GaAs-InP chemistry.

We have found that relatively smooth epitaxial growth of InP on (100) GaAs substrates can be obtained with a two-step process in which, first, a thin layer, estimated to be 100 to 200 Å thick, is deposited at a low temperature ( $\sim 400^\circ\text{C}$ ) and then growth is restarted at the normal growth temperature ( $\sim 650^\circ\text{C}$ ). This behavior is similar to that of the growth of GaAs on Si substrates; the problems are similar in that the lattice constant of the unstrained epitaxial material is about 4 percent larger than that of the substrate in both cases. Nomarski photomicrographs of the InP/GaAs growth are displayed in Figure 1-12 and show the improvement in morphology which results from using the two-step process. The mat-like appearance of the growth from the single-step process is caused by an island-like morphology. At a higher magnification, islands of approximately  $1 \times 10 \mu\text{m}$ , aligned along  $\langle 110 \rangle$  directions, can be resolved.

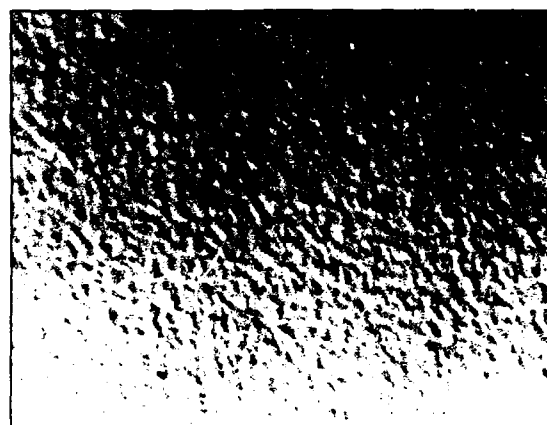
The InP/GaAs growth has been used to evaluate deposition patterns in a chimney reactor designed to hold a single 2-in-diam. substrate. Susceptor rotation will be employed to provide good uniformity, but the tests we have undertaken here are designed to establish the effects of parameters such as the amount and type of carrier gas, injector design, and cooling of the reactor wall opposite the substrate surface. These effects are more readily discerned in the absence of rotational averaging. Typically, InP of roughly  $1\text{-}\mu\text{m}$  thickness is deposited during an hour of growth by the two-step process on a 2-in-diam. GaAs substrate. After growth, an etch mask ( $\sim 2000 \text{ Å}$  PSG) with  $1.5\text{-mm}$  protected squares on  $2\text{-mm}$  centers is patterned on the InP growth by photolithographic techniques, and an etch, consisting of equal volumes of hydrochloric and phosphoric acids which etches InP but not GaAs, is used to isolate the protected squares. A surface profilometer is then used to establish InP thickness vs position on the wafer. Figure 1-13 displays relative thickness data from a typical run and shows a front-to-back thickness decrease of  $\sim 30$  percent. At  $650^\circ\text{C}$  the growth rate is limited by the diffusion of the indium alkyl to the substrate surface, and the thickness variation can be explained by a boundary layer model where the diffusion occurs across a boundary layer which increases in width with distance from the leading edge of the substrate. With a profilometer stylus of  $12.5\text{-}\mu\text{m}$  tip radius, the observed variation in height across the  $1.5\text{-mm}$  squares is typically in the  $30$  to  $60 \text{ Å}$  region for the InP/GaAs grown by the two-step process, but can be an order of magnitude greater for material grown without the low-temperature step.

S.H. Groves  
S.C. Palmateer  
A. Napoleone



**SINGLE-STEP PROCESS**

┌──────────┐  
100  $\mu$ m



**TWO-STEP PROCESS**

*Figure 1-12. Nomarski photomicrographs of InP growth on (100) GaAs substrates. The top photo shows growth typical of a single-step process, and the bottom photo shows the improvement that results when the growth at 650° C is preceded by the deposition of 100-200 Å layer at 400° C.*

96005-12

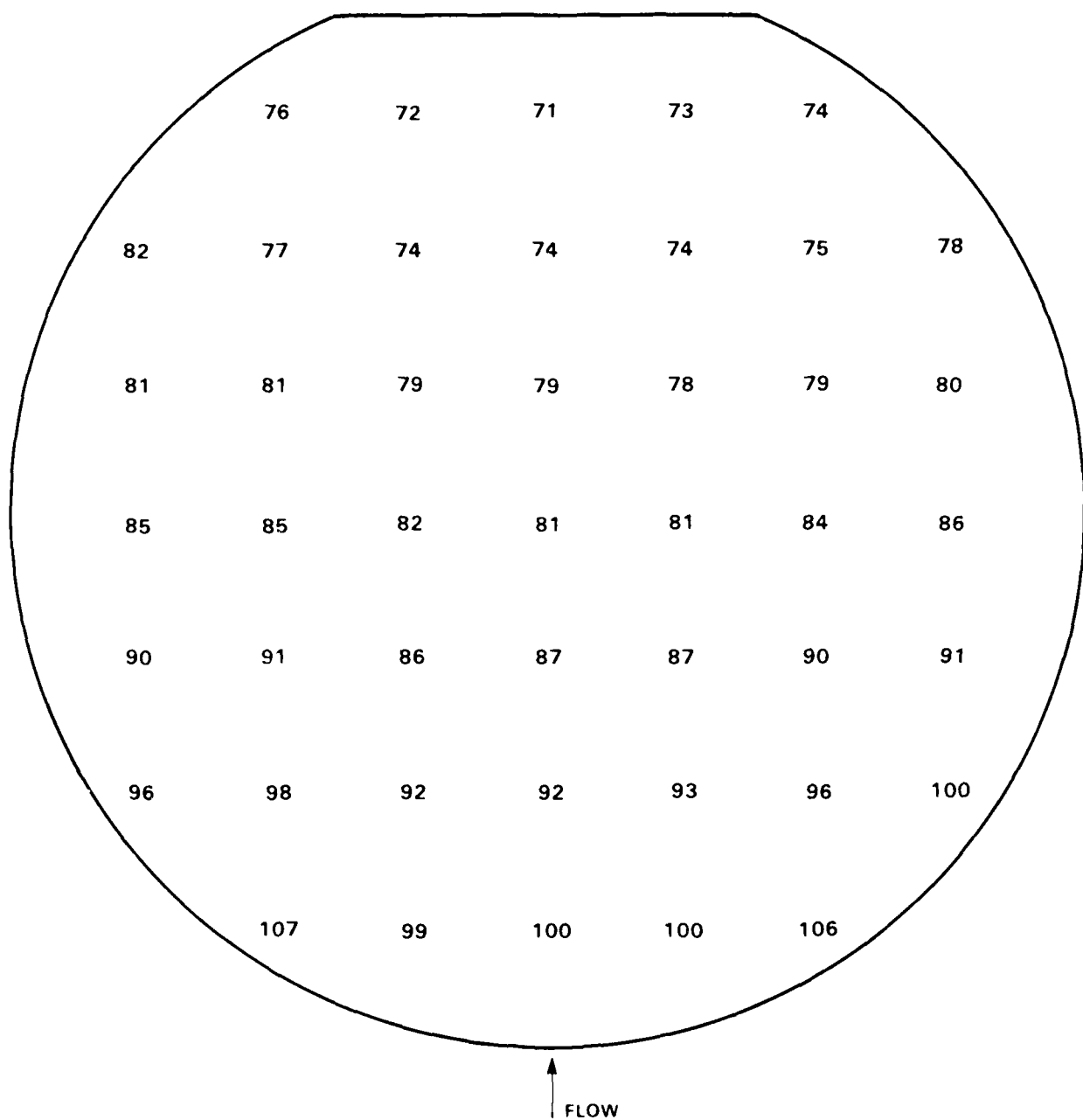


Figure 1-13. Typical profile of relative growth thickness vs position on substrate. Here 100 corresponds to 1.5  $\mu\text{m}$ .

## REFERENCES

1. W.K. Burns and A.F. Milton, IEEE J. Quantum Electron. **QE-16**, 446 (1980)
2. G.L. Harnagel, P.S. Cross, C.R. Lennon, M. Devito, and D.R. Scifres, Electron. Lett. **23**, 744 (1987)
3. D.F. Welch, W. Streifer, R.L. Thornton, and T.L. Paoli, Electron. Lett. **23**, 525 (1987).
4. D.B. Tuckerman and R.F.W. Pease, IEEE Electron Device Lett. **EDL-2**, 126 (1981).
5. R.J. Philips, M.S. Thesis, MIT, Cambridge, Massachusetts (1987).
6. L.A. Missaggia, J.N. Walpole and Z.L. Liao (unpublished).
7. N.L. DeMeo, J.P. Donnelly, F.J. O'Donnell, M.W. Geis, and K.J. O'Connor, Nucl. Instrum. Methods Phys. Res. **B7/8**, 814 (1985), DTIC AD-A155713.
8. D.Z. Tsang and Z.L. Liao, J. Lightwave Technol. **LT-5**, 300 (1987), DTIC AD-A188676.
9. Z.L. Liao, J.N. Walpole, D.Z. Tsang, and V. Diadiuk, IEEE J. Quantum Electron. **QE-24**, 36 (1988).
10. Z.L. Liao, and J.N. Walpole, IEEE J. Quantum Electron. **QE-23**, 313 (1987), DTIC AD-A187552.
11. Z.L. Liao, J.N. Walpole, and D.Z. Tsang, Appl. Phys. Lett. **44**, 945 (1984), DTIC AD-A147996.

## 2. QUANTUM ELECTRONICS

### 2.1 ELECTROOPTICALLY TUNED SINGLE-FREQUENCY $\text{Ti:Al}_2\text{O}_3$ LASER

A  $\text{Ti:Al}_2\text{O}_3$  ring laser can be tuned with electrooptic crystals from 767 to 834 nm while maintaining single-frequency operation. The tuning is accomplished with three electrooptic birefringent filters. The highest order birefringent tuner, made of MgO-doped  $\text{LiNbO}_3$ , operates in 3000th order. This crystal is subject to photorefractive damage that limits the laser operation to 2 min before the crystal needs to be moved.

The ring cavity for the  $\text{Ti:Al}_2\text{O}_3$  laser is similar to the cavity described in previous reports.<sup>1</sup> An argon ion laser pumps a four-mirror ring cavity containing the laser crystal, three electrooptic crystals, and an acousto-optic modulator used as a unidirectional device. The laser output is monitored by a power meter, wavemeter, and Fabry-Perot spectrum analyzer. This report describes the three stages of electrooptic tuning and factors affecting their selection.

Tuning using birefringent filters relies on a fixed linear polarization in the laser cavity. The birefringent crystal selects the laser wavelength by acting as an integer-order waveplate for one specific wavelength, but as a fractional-order waveplate for other wavelengths. For these other wavelengths, the waveplate changes the polarization from linear horizontal to elliptical. For polarizations other than horizontal, the cavity has additional losses caused by the Brewster-angle surfaces. To the author's knowledge, this is the first study that has placed three electrooptic tuning elements in a laser cavity and the first investigation of electrooptic tuning in a ring laser cavity.

The coarsest tuner in the cavity consisted of a 12th-order bias plate and a  $\text{LiNbO}_3$  crystal between Brewster-angle windows. The bias plate is a 0.12-mm-thick antireflection-coated sapphire crystal with its optical axis normal to the direction of light propagation and at  $45^\circ$  to the polarization direction. The  $\text{LiNbO}_3$  crystal is 25 mm long by 2 mm thick, with the optical axis oriented along the direction of propagation. A voltage of 700 V across the thickness of the crystal induces a birefringence at  $45^\circ$  to the polarization direction with a retardation of one wavelength.

A description of this element, its tuning characteristics, and its operation as the sole tuning element in the  $\text{Ti:Al}_2\text{O}_3$  laser is described elsewhere.<sup>2</sup> A voltage between 0 and 700 V tunes the wavelength of the laser between 767 nm and 834 nm. The tuning range is limited by the retardation order of the waveplate. The waveplate acts as an integer-order waveplate for all wavelengths  $\lambda$  that satisfy  $\Delta n L / N = \lambda$ , where  $\Delta n$  is the birefringence,  $L$  is the length of the crystal, and  $N$  is an integer. Thus, the tuning range near 800 nm for a 12th-order bias is 800 nm / 12 = 67 nm, in good agreement with the observed tuning range. Although a lower order bias plate would give a wider tuning range, we observed that a 4th-order bias plate did not provide enough selectivity for the next higher resolution tuning element.

The second tuning element consisted of a  $\sim 150$ th-order bias plate and a KD\*P crystal between Brewster-angle windows. This device is obtained commercially and its operation is described elsewhere.<sup>3</sup> The tuning range available with this crystal alone should be  $800 \text{ nm} / 150 = 5.3 \text{ nm}$ , in good agreement with a measured wavelength hopping of  $4.9 \text{ nm}$ . This wavelength hopping range implies that the waveplate was operating in approximately 160th order. Tuning over the  $4.9\text{-nm}$  interval required a change of  $9.5 \text{ kV}$  across the KD\*P. Each of 13 tuning ranges was accessed by changing the applied voltage on the coarse tuner while leaving the second tuner at a fixed voltage. Thus, it can be presumed that any wavelength in the interval between  $767 \text{ nm}$  and  $834 \text{ nm}$  is accessible. However, the selectivity is not great enough to induce single-frequency operation without an even higher resolution tuning element.

The third tuning element, which is unique to the present study, consisted of a 3000th-order MgO-doped LiNbO<sub>3</sub> crystal between Brewster-angle surfaces. The antireflection-coated crystal is  $3 \text{ mm}$  thick by  $30 \text{ mm}$  long (propagation direction) with the optic axis perpendicular to the propagation direction and parallel to the direction in which the voltage is applied. The crystal is oriented so that the optic axis is at  $45^\circ$  to the incident polarization. The large birefringence of LiNbO<sub>3</sub>,  $\Delta n = 0.072$ , provides the large bias. Only  $500 \text{ V}$  is required to change the retardation by one wavelength. The tuning range available with this crystal alone should be  $800 \text{ nm} / 3000 = 0.27 \text{ nm}$ . Unfortunately, extensive testing with this crystal in the laser cavity could not be done because the buildup of photorefractive damage prevented long-term measurements. However, it was observed that during the  $2 \text{ min}$  of laser operation the single-frequency operation was stable as measured with a Fabry-Perot etalon.

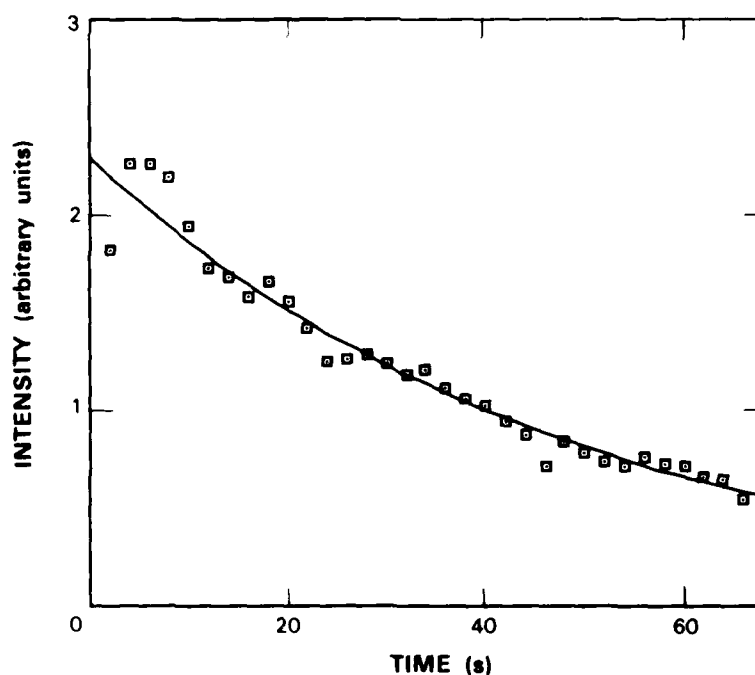


Figure 2-1. Time dependence of the single-frequency Ti:Al<sub>2</sub>O<sub>3</sub> laser intensity. Three electrooptic crystals, including a MgO-doped LiNbO<sub>3</sub> crystal, are in the laser cavity. The fall in intensity is fit by an exponential decay with a lifetime of  $30 \text{ s}$  caused by photorefractive damage of the MgO-doped LiNbO<sub>3</sub> crystal.

96005-14

The power decay is shown in Figure 2-1. It is seen that the decay does not drop off linearly in time as would be expected if the losses increased linearly. Instead it appears that the loss in the laser cavity induced by the MgO-doped LiNbO<sub>3</sub> crystal decreases with decreasing laser intensity, as expected for the photorefractive effect.<sup>4</sup> The dependence of photorefractive damage on crystallographic orientation was also observed<sup>4</sup> and is consistent with the greater damage in the fine tuner than in the coarse tuner.

Electrooptic frequency switching from one single frequency to another is limited by the selectivity of the highest resolution tuning element, which provides only 0.01 percent additional loss for the adjacent frequency modes. Therefore, as seen in Figure 2-2, it takes a time of approximately 0.5 ms to switch to a new frequency. Figure 2-2 is obtained by monitoring the transmission of a fixed Fabry-Perot etalon while switching the voltage being applied to the MgO-doped LiNbO<sub>3</sub> crystal. The fast turn-off time for this mode is a result of much larger additional loss because the applied voltage tunes the laser over many longitudinal modes. In the future we plan to obtain much faster tuning and eliminate the photorefractive damage by using different crystals and using electrooptic etalons instead of the highest order birefringent tuner.

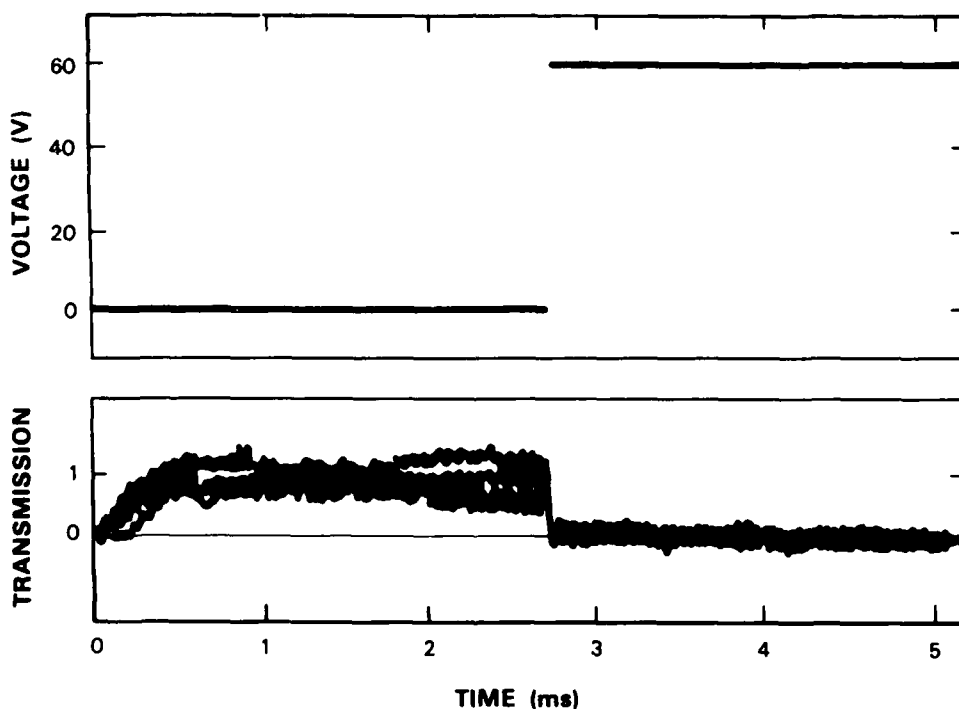


Figure 2-2. Electrooptic switching of the single-frequency Ti:Al<sub>2</sub>O<sub>3</sub> laser. The upper trace shows the voltage applied to the LiNbO<sub>3</sub> crystal. The lower trace shows the transmission through a fixed Fabry-Perot etalon adjusted for maximum transmission with the crystal operating at the lower voltage. The applied voltage is a repetitive square wave of 100 V.

Finally, we note the use of an acoustooptic modulator rather than a Faraday rotator and compensator as a unidirectional device.<sup>5</sup> In using the Faraday rotator and compensator, we observed occasional reversal of directions. Presumably, the polarization rotation brought about by the Faraday rotator and compensator for reverse direction propagation could be undone by the electrooptic birefringent tuners. Rather than investigate this issue we have used the acoustooptic modulator as a unidirectional device because it does not affect the laser polarization.

In conclusion, we have operated an electrooptically tuned single-frequency Ti:Al<sub>2</sub>O<sub>3</sub> laser by using three birefringent tuning elements. This laser can tune from one frequency to another in 0.5 ms. The laser operates stably but not in a single frequency using only two tuners. The addition of the third and highest resolution tuner results in single-frequency operation, but photorefractive damage to the tuner limits the operating time to 2 min.

P.A. Schulz

## 2.2 INTERFEROMETRIC MEASUREMENT OF OPTICALLY INDUCED REFRACTIVE INDEX CHANGES IN Ti:Al<sub>2</sub>O<sub>3</sub>

Optically induced refractive index changes of Ti:Al<sub>2</sub>O<sub>3</sub> pumped at 532 nm have been measured interferometrically at 632.8 nm. These changes, which decay with the 3- $\mu$ s fluorescence lifetime of Ti<sup>3+</sup> ions, are attributed to nonresonant dispersion effects.

Ti:Al<sub>2</sub>O<sub>3</sub> is an important material for optically pumped, tunable solid-state laser oscillators and amplifiers in the near-infrared spectral region. We have recently observed<sup>6</sup> optically induced birefringence at signal wavelengths of 632.8 nm (He-Ne laser) and 790.7 nm (Ti:Al<sub>2</sub>O<sub>3</sub> laser) in Ti:Al<sub>2</sub>O<sub>3</sub> pumped with 532-nm radiation from a frequency-doubled, Q-switched (10-ns pulses) Nd:YAG laser. This induced birefringence,  $\delta n(t) = |\Delta n_{\pi}(t) - \Delta n_o(t)|$ , where  $\Delta n_{\pi}(t)$  and  $\Delta n_o(t)$  are the changes in refractive index for light polarized parallel and perpendicular to the c-axis, respectively, decays with a time constant characteristic of the fluorescence lifetime of the Ti<sup>3+</sup> ions in Ti:Al<sub>2</sub>O<sub>3</sub>. The peak values of  $\delta n(t)$  at 632.8 nm and 790.7 nm are similar. These properties suggest that the optically induced birefringence is a nonresonant effect due to the population transfer from the <sup>2</sup>T<sub>2g</sub> ground state to the <sup>2</sup>E<sub>g</sub>(E<sub>3/2</sub>) excited state, which is the upper lasing level. To further investigate the origin of the induced birefringence we have interferometrically measured  $|\Delta n_{\pi}(t)|$  and  $|\Delta n_o(t)|$  at 632.8 nm. The results are consistent with those of the earlier measurements.

Measurements of  $|\Delta n_{\pi}(t)|$  and  $|\Delta n_o(t)|$  were made at room temperature by using the experimental setup shown schematically in Figure 2-3, which incorporates a Mach-Zehnder interferometer. The Ti:Al<sub>2</sub>O<sub>3</sub> sample was a 6-mm-diameter, single-crystal cylinder of length  $L = 20$  mm with its axis perpendicular to the c-axis. The peak absorption coefficient  $\alpha_{\pi}$  at 490 nm was 3 cm<sup>-1</sup>, corresponding to a Ti<sup>3+</sup> concentration of  $3 \times 10^{19}$  cm<sup>-3</sup>. The crystal was placed in one arm of the interferometer. The beam from a CW He-Ne laser propagated along the axis of the cylinder, almost collinearly ( $\sim 1.5^\circ$ ) with the Q-switched 532-nm pump beam. The polarization of the He-Ne laser beam was fixed. The sample was rotated to make the signal beam either parallel or

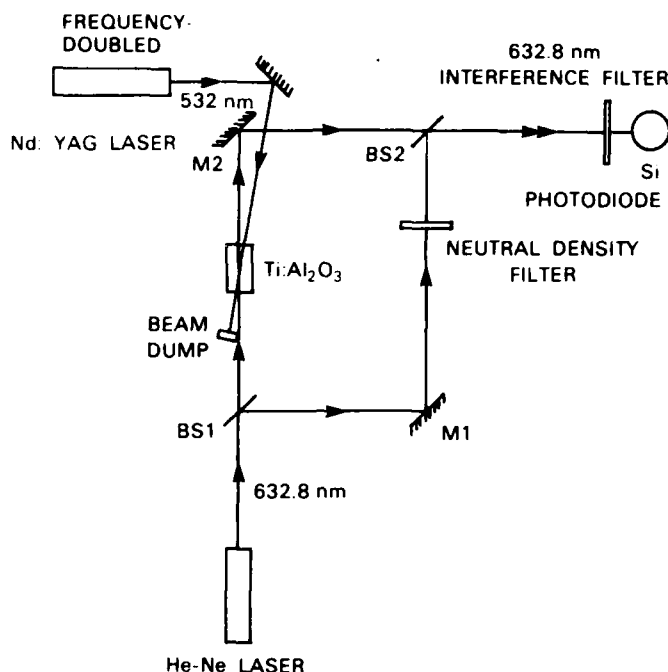


Figure 2-3. Schematic of the experimental setup for the interferometric measurement of optically induced changes in refractive index  $|\Delta n_\pi|$  and  $|\Delta n_\sigma|$ . BS1 and BS2 denote beamsplitters, and M1 and M2 denote mirrors.

perpendicular to the c-axis, and the pump polarization was rotated to maintain it parallel to the c-axis. Neutral density filters were used to balance the two arms of the interferometer. A 632.8-nm interference filter was placed in front of a silicon photodiode that measured the intensity  $I$  of the transmitted signal beam.

An example of the temporal dependence of  $I$  for the  $\sigma$  polarization is shown in Figure 2-4. The time at which the 10-ns pump pulse is incident on the  $\text{Ti:Al}_2\text{O}_3$  sample is designated as  $t = 0$ . The minimum and maximum intensities are indicated by  $I_{\min}$  and  $I_{\max}$ , respectively. The initial rise of the signal is limited by the response time of the detector, which is 600 ns. The dashed horizontal line indicates the intensity for  $t < 0$ . Most of the pump-induced change in intensity decays with a time constant characteristic of the fluorescence lifetime of the  $\text{Ti}^{3+}$  ions ( $3 \mu\text{s}$ ). The remaining small change decays on a millisecond time scale characteristic of thermal effects.

The intensity transmitted through the interferometer at a time  $t$  is given by

$$I(t) = \frac{1}{2} (I_{\max} - I_{\min}) \{1 + \cos [\phi_0 + \phi(t)]\} + I_{\min} \quad (2-1)$$

where  $\phi_0$  is the initial phase difference between the two arms of the interferometer and  $\phi(t)$  is the pump-induced phase difference. From Equation (2-1) we deduce  $\phi(t_1)$  and  $\phi(t_2)$  at the times  $t_1$

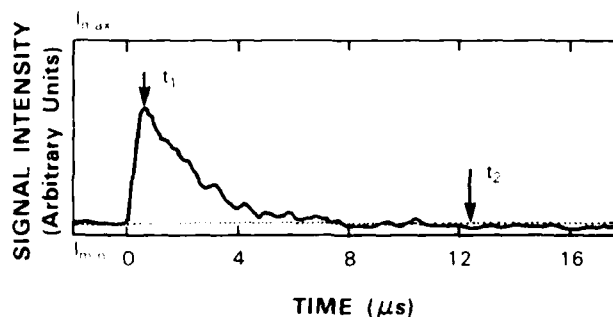


Figure 2-4. Temporal dependence of the intensity  $I$  of the transmitted signal beam for the  $\sigma$  polarization.  $I_{\max}$  and  $I_{\min}$  are the minimum and maximum values of  $I$ .

and  $t_2$  indicated in Figure 2-4. When  $\exp(-\alpha_\pi L) \ll 1$ , valid in the present case where  $\alpha_\pi L = 6$ , the difference between  $\phi(t_1)$  and  $\phi(t_2)$  yields the peak value of  $\phi(t)$  for the  $\sigma$  polarization

$$\Delta\phi_\sigma = |\phi_\sigma(t_2) - \phi_\sigma(t_1)| = \frac{2\pi}{\lambda} \frac{|\Delta n_\sigma|}{\alpha_\pi} \quad (2-2)$$

where  $\lambda$  is the vacuum wavelength of the probe beam and  $|\Delta n_\sigma|$  is the peak value of the non-thermal portion of the pump-induced change in the refractive index for the  $\sigma$  polarization. A similar procedure was used for the  $\pi$  polarization to obtain  $|\Delta n_\pi|$ .

In Figure 2-5(a),  $\Delta\phi_\pi$  and  $\Delta\phi_\sigma$  are plotted as a function of the incident pump energy density. The right-hand ordinate gives the corresponding values of  $|\Delta n_\pi|$  and  $|\Delta n_\sigma|$  calculated from Equation (2-2). The data are shown as circles, and the straight lines are linear fits to the data constrained to pass through the origin. Note that  $\phi$  and  $|\Delta n|$  are greater for the  $\sigma$  polarization than for the  $\pi$  polarization. This anisotropy is opposite in sign to the anisotropy for the visible absorption band or the infrared fluorescence band. In Figure 2-5(b) we compare the values of  $\delta\phi = \Delta\phi_\sigma - \Delta\phi_\pi$  (with corresponding values of  $\delta n = |\Delta n_\sigma| - |\Delta n_\pi|$  given by the right-hand ordinate) obtained from interferometric measurements with those obtained from optically induced birefringence measurements on the same sample. The results of the two measurements are in rough agreement; this indicates that  $\Delta n_\sigma$  and  $\Delta n_\pi$  have the same sign.

The values of the induced refractive index changes are an order of magnitude larger than those expected from intensity-dependent dispersion associated with the visible absorption band or the infrared fluorescence band. We conclude that the mechanism for the induced refractive index changes is a nonresonant effect due to the population transfer from the  $^2T_{2g}$  ground state to the  $^2E_g(E_{3,2})$  excited state (the upper lasing level). A similar mechanism has been suggested by Venkatesan and McCall<sup>7</sup> for  $\text{Cr}^{3+}$  in  $\text{Al}_2\text{O}_3$ . An effort is under way to obtain quantitative results from this model.

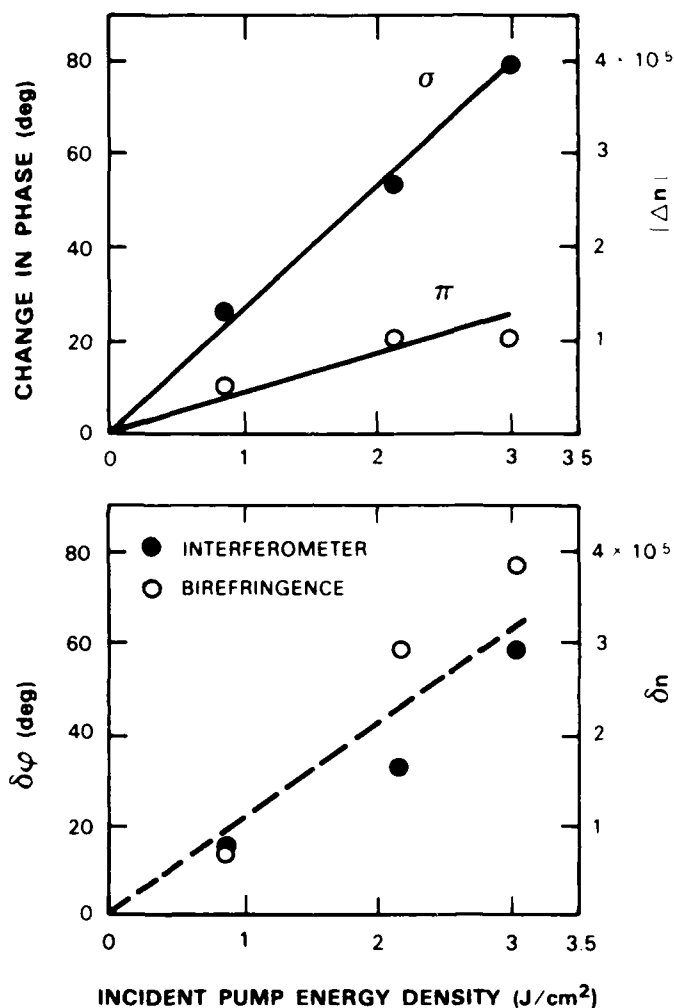


Figure 2-5. (a) Induced phase and index of refraction changes for the  $\pi$  and  $\sigma$  polarizations vs incident pump energy density. (b) Difference in induced phase change and index of refraction changes between the  $\pi$  and  $\sigma$  polarizations obtained from interferometric and optically induced birefringence measurements. Straight lines are linear fits to the data, which are shown as circles.

In high gain pulsed amplifiers, time-dependent changes in refractive index generate chirps in the frequency of the amplifier output. Based on the pump-induced changes in refractive index discussed above, we expect a frequency chirp at the highest levels of pumping of  $\sim 70$  and  $\sim 20$  kHz for the  $\sigma$  and  $\pi$  polarizations, respectively. It should be possible, however, to compensate for the deterministic chirps by controlling the phase of the input pulse.

K.F. Wall	A.J. Strauss
R.E. Fahey	M.D. Sciacca
R.L. Aggarwal	

## 2.3 MICROCAVITY Nd:YAG LASER

Diode-pumped microcavity solid state lasers are potentially compact, rugged sources of single-frequency, coherent radiation. When the laser cavity is made sufficiently short, the cavity mode spacing is greater than the gain-bandwidth of the solid state medium, and only one cavity mode can lase, as illustrated in Figure 2-6. Nd has lasing transitions at about 1.06 and 1.3  $\mu\text{m}$ . Its strong absorption at GaAlAs laser diode wavelengths makes it a candidate for the active element in the gain medium of such a laser. Operating at 1.3  $\mu\text{m}$  (the loss minimum for optical fibers), a Nd-based microcavity laser would be a valuable component for optical communications.

To demonstrate the feasibility of a diode-pumped microcavity solid state laser, a 1.06- $\mu\text{m}$  microcavity Nd:YAG laser was constructed. A slab of Nd:YAG was cut and polished to a thickness of 700  $\mu\text{m}$  and sandwiched between two flat mirrors. The output mirror had a reflectivity of 99.7 percent at 1.06  $\mu\text{m}$  and was designed to reflect the pump laser. The opposite mirror had a reflectivity of 99.9 percent at 1.06  $\mu\text{m}$  and transmitted the pump. Figure 2-7 shows a microcavity laser that was sandwiched between two glass windows. A Ti:Al<sub>2</sub>O<sub>3</sub> laser was used in place of a diode laser as the pump source. It was tuned to the Nd:YAG absorption peak at 0.809  $\mu\text{m}$  and focused onto the laser package with a microscope objective. The focusing lens had a 6.45-mm

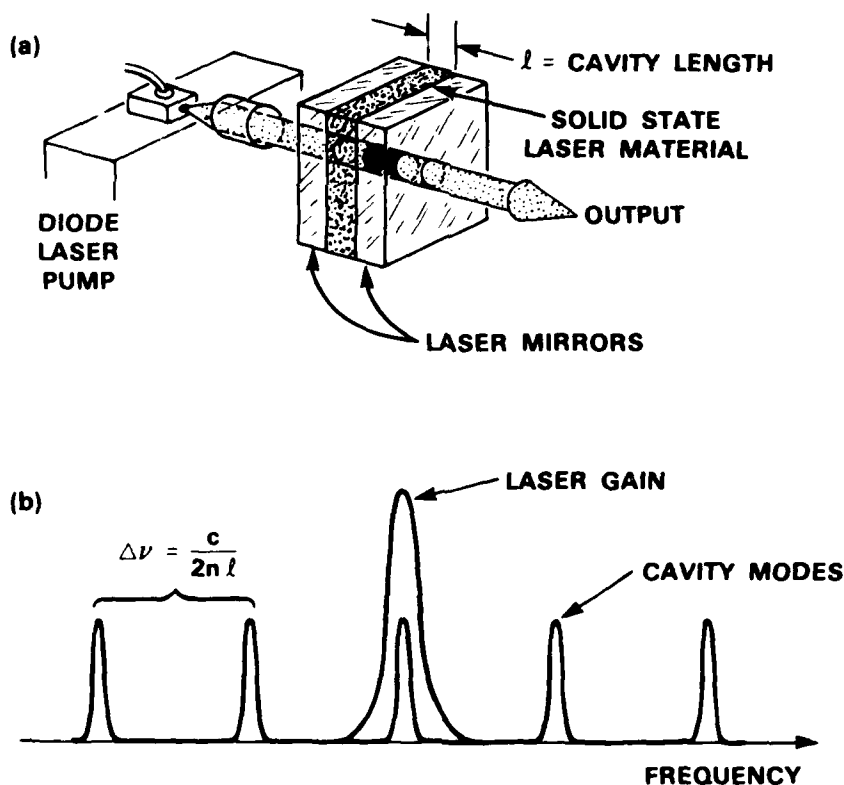


Figure 2-6. (a) Illustration of a diode pumped microcavity solid state laser. (b) Gain spectrum of a solid state medium shown superimposed on the cavity mode spacing of a microcavity laser to illustrate why single-frequency operation occurs.

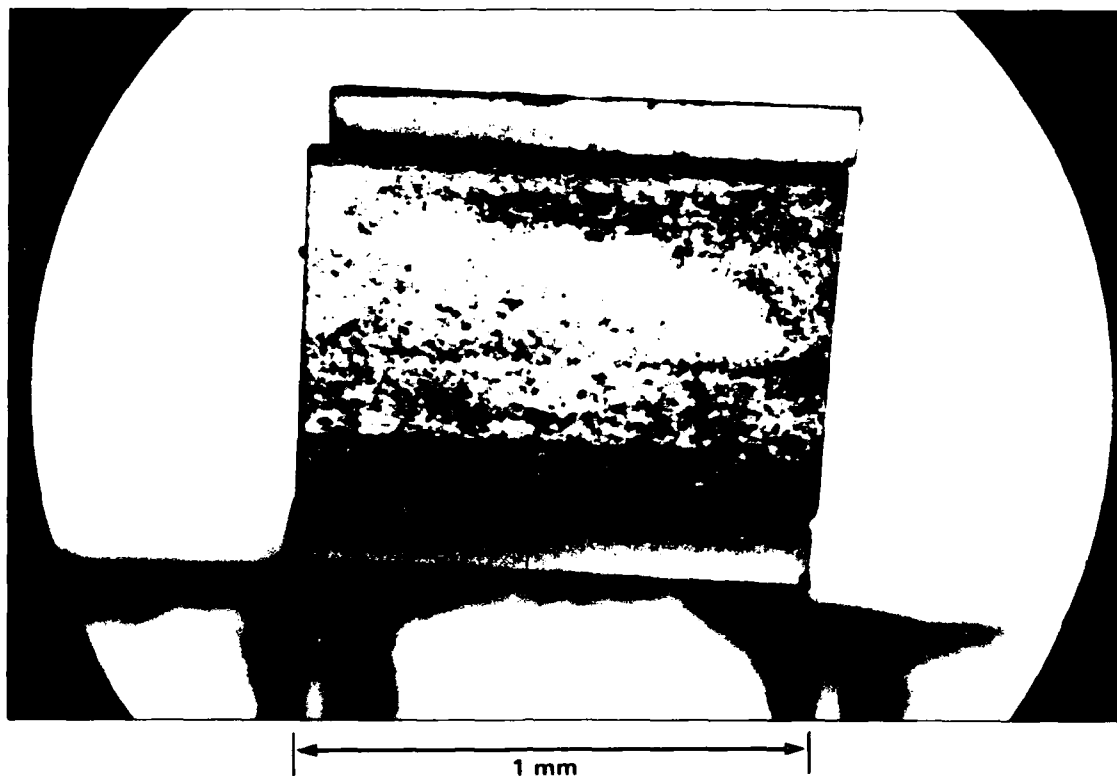


Figure 2-7. Photograph of a microcavity Nd:YAG laser, showing the gain medium and cavity mirrors.

focal length and resulted in an experimentally determined waist size of about  $10\text{ }\mu\text{m}$  for the pump beam. Measurements showed that 18 percent of the incident pump power was reflected by the laser package and 27 percent was transmitted. The experiments were run CW at room temperature. When the Nd:YAG microcavity was properly aligned with the pump, single longitudinal mode and single spatial mode operation was observed. The shape of the spatial mode varied with the position of the pump on the laser package, but was nearly circularly symmetric at the positions where the strongest lasing was observed. At these positions the output consisted of only one longitudinal mode. The spectrometer and Fabry-Perot traces in Figure 2-8 show instrument-limited linewidths at all pump powers. The maximum laser linewidth consistent with these measurements is about 10 MHz. Heterodyne experiments are planned to better resolve the linewidth. At other pump positions it was possible to obtain multimode operation, and the mode separation was measured to be 0.32 nm.

A computer-controlled variable attenuator was introduced into the path of the pump laser to obtain the input-output power characteristics of the Nd:YAG microcavity laser. These characteristics varied considerably with the pump position on the laser package. At the best spots the lasing

threshold was measured to be below 1 mW, and the slope quantum efficiency (calculated from the output of the laser from the 99.7 percent reflecting mirror only) was slightly greater than 30 percent. The input-output curve of a low threshold location is shown in Figure 2-9 for absorbed pump powers of up to 40 mW. At higher absorbed powers, thermal effects result in a strongly nonmonotonic input-output curve. The thermal nature of the effects was confirmed by chopping the pump. At poor spots lasing was not observed with pump powers as high as 400 mW.

Future experiments will involve optimization of the Nd:YAG slab thickness, direct deposition of mirrors on the Nd:YAG crystal, use of other Nd host materials, 1.3- $\mu$ m laser operation, diode laser pumping, and temperature studies. Although much work remains to be done, the low pump threshold, high efficiency, and single-frequency operation of the Nd:YAG microcavity laser makes diode-pumped solid state microcavity lasers extremely promising.

J.J. Zayhowski  
A. Mooradian  
R.C. Hancock

## 2.4 FREQUENCY CONVERSION

A long-pulse Nd:YAG laser system has been modified to produce shorter pulse duration envelopes than the 50- to 200- $\mu$ s macropulse length previously described.<sup>8</sup> The present system still produces wave trains of mode-locked pulses (micropulses) of 100-ps pulse length with a 10-ns spacing, but the duration or envelope of these pulses (the macropulse) is limited to either 1 to 2  $\mu$ s or 10 to 60  $\mu$ s. With these modifications, the temporal output of the system now resembles that of the newly installed multibeam pump laser system of the Ti:Al<sub>2</sub>O<sub>3</sub> laser program. The modified system may now be used as a test bed for investigating material properties for possible application in the larger system.

Initial frequency-conversion experiments have been conducted with the modified system operating at 10 Hz with a 1- $\mu$ s pulse envelope. The temporal shape of a typical macropulse operating at this pulse length is given in Figure 2-10. These experiments were carried out with KD\*P and  $\beta$ -BaB<sub>2</sub>O<sub>4</sub> crystals. Frequency-doubling efficiencies greater than 50 percent were achieved in both these materials, as described below.

For the KD\*P study, three uncoated crystals, > 98 percent deuterated, with lengths of 25, 40, and 50 mm were used. Second harmonic generation (SHG) experiments with a 100- $\mu$ s macropulse had previously been carried out with these crystals. With the long pulse, saturation was observed at SHG efficiency levels between 10 and 20 percent. This was not the case with the shorter 1- $\mu$ s macropulse. For the present experiment the crystals were irradiated with a 5-mm-diameter near-collimated 1.06- $\mu$ m laser beam. The SHG conversion efficiency internal to the crystal, after considering Fresnel losses at the uncoated surfaces, is shown in Figure 2-11. Efficiencies in excess of 50 percent were obtained in both the 40- and 50-mm crystals, and above 40 percent

96005-18

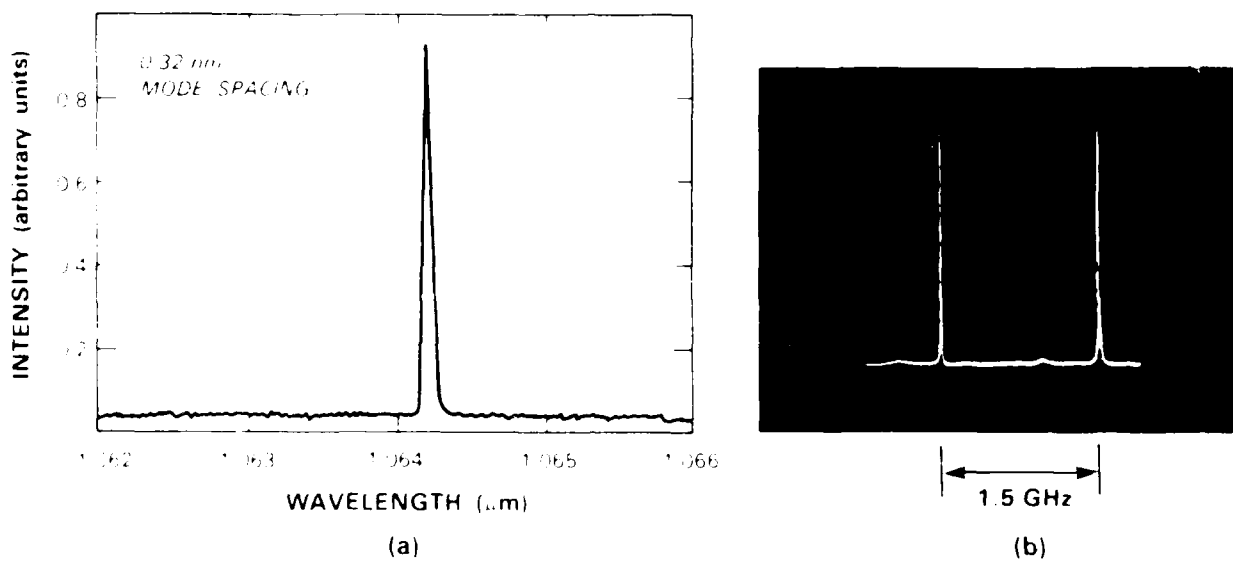


Figure 2-8. (a) Instrument-limited-spectrometer and (b) Fabry-Perot traces of the output of the Nd:YAG microcavity laser.

96005-19

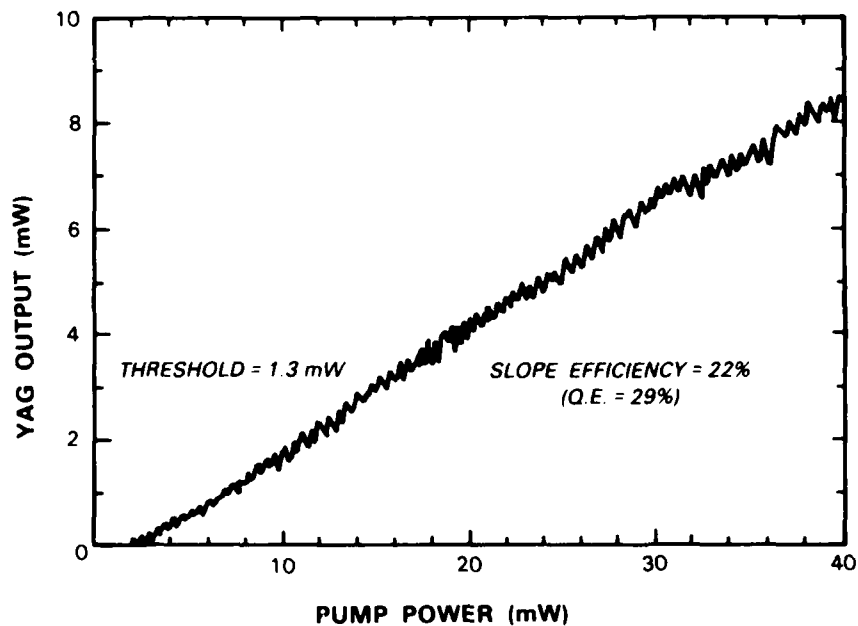


Figure 2-9. Input-output power characteristics of the Nd:YAG microcavity laser. The input power shown is the absorbed pump power, and the output power was measured from the output face of the cavity only.

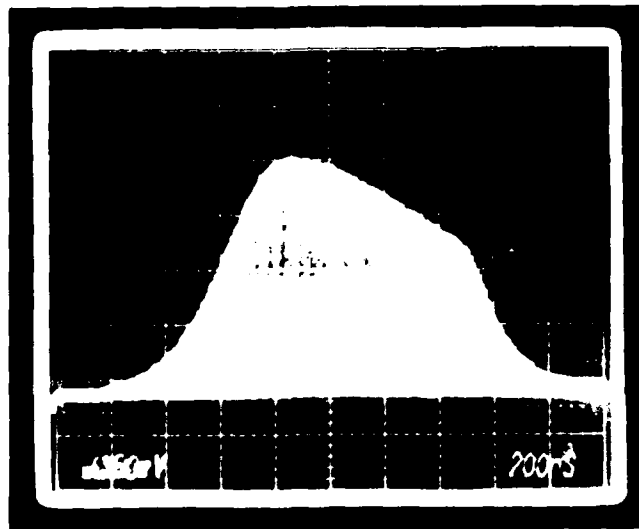


Figure 2-10. Temporal pulse envelope of mode-locked Nd:YAG laser.

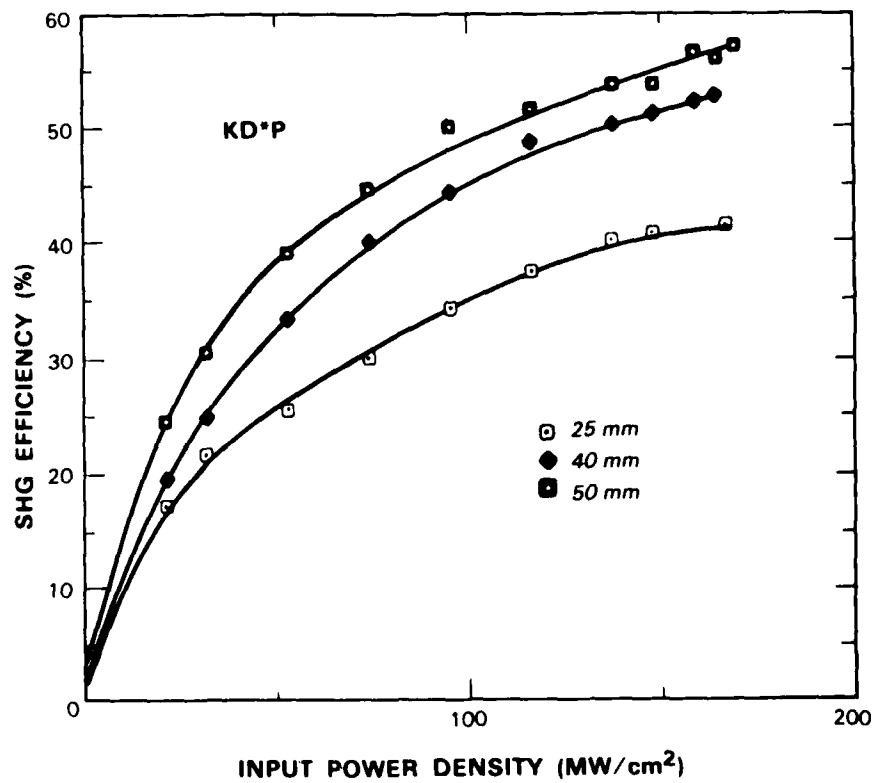


Figure 2-11. Internal frequency-doubling efficiency vs incident power density in KD\*P crystals for a macropulse length of  $1 \mu\text{s}$  and PRF of 10 Hz.

in the 25-mm crystal. The difference in behavior between the 1- $\mu$ s and 100- $\mu$ s pulses may be due to thermal effects occurring during the longer pulse. However, preliminary experiments with a 50- $\mu$ s macropulse failed to show the saturation effect.

In addition, attempts were made to increase the overall frequency conversion efficiency in KD\*P by using two crystals in a quadrature arrangement.<sup>9</sup> No improvement was obtained despite the ability to achieve high efficiencies in each of the crystals individually at their tandem positions. To establish if the lack of improvement is due to feedback from surface reflection, the crystals are being antireflection coated.

A similar experiment was carried out using a 7.2-mm-long uncoated  $\beta$ -BaB<sub>2</sub>O<sub>4</sub> (BBO) crystal as the frequency doubler. For this experiment the near-collimated fundamental beam diameter was reduced to 3.5 mm to reach higher input power densities. The results are given in Figure 2-12. At an average micropulse energy density of 260 MW cm<sup>2</sup>, the internal efficiency is over 50 percent, with no indication of saturation.

A preliminary-frequency-quadrupling experiment was carried out by placing an uncoated BBO crystal oriented for SHG from 0.532  $\mu$ m in tandem with the 1.064- $\mu$ m BBO crystal used in the experiment described above. The frequency conversion efficiency from 0.532 to 0.266  $\mu$ m saturated at a value slightly below 20 percent. The limiting factor in this experiment is believed to be the small phase-matching acceptance angle at 0.532  $\mu$ m.

N. Menyuk  
M.E. MacInnis

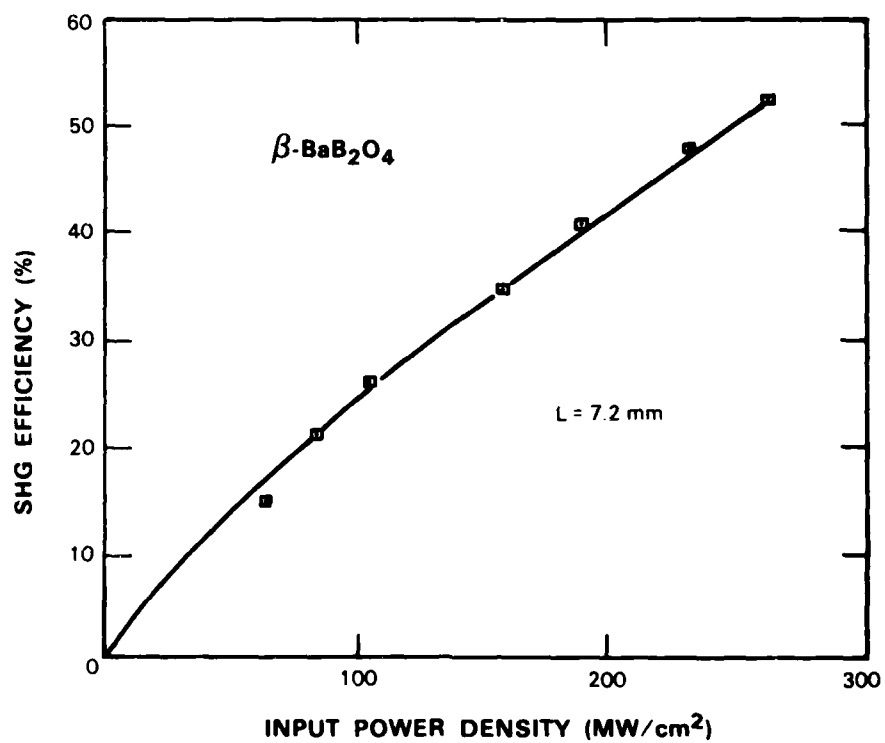


Figure 2-12. Internal frequency-doubling efficiency vs incident power density in BaB<sub>2</sub>O<sub>4</sub> for a macropulse length of 1  $\mu$ s and PRF of 10 Hz.

96005-22

## REFERENCES

1. P.A. Schulz, IEEE J. Quantum Electron. (accepted for publication April 1988).
2. V. Daneu and A. Sanchez, Conference on Lasers and Electrooptics Technical Digest Series 1987, Vol. 14 (OSA, Washington, D.C., 1987), paper THQ3.
3. C.L. Tang, V.G. Kreismanis, and J.M. Ballantyne, Appl. Phys. Lett. 30, 113 (1977).
4. A.M. Glass, Opt. Eng. 17, 470 (1978).
5. R. Roy, P.A. Schulz, and A. Walther, Opt Lett. 12, 672 (1987), DTIC AD-A187550.
6. Solid State Research Report, Lincoln Laboratory, MIT (1987:4).
7. T.N.C. Venkatesan and S.L. McCall, App. Phys. Lett. 30, 282 (1977).
8. Solid State Research Report, Lincoln Laboratory, MIT (1987:1), p. 28, DTIC AD-A185987.
9. D. Eimerl, IEEE J. Quantum Electron. QE-23, 1361 (1987).

### 3. MATERIALS RESEARCH

#### 3.1 LIQUID-SOLID INTERFACE MORPHOLOGIES AND DEFECT STRUCTURES IN ZONE-MELTING-RECRYSTALLIZED SI-ON-INSULATOR FILMS

The zone-melting recrystallization (ZMR) process is now capable of producing high-quality Si-on-insulator (SOI) films, without continuous subboundaries, in which isolated dislocations or dislocation clusters are the principal defects.<sup>1-5</sup> We have conducted a study to define the experimental conditions that yield the lowest defect densities. To prepare the samples, a 1- $\mu\text{m}$ -thick amorphous Si film was formed by low-temperature low-pressure chemical vapor deposition (LTLPCVD) on (100) Si wafers coated with 2  $\mu\text{m}$  of thermally grown  $\text{SiO}_2$ . The Si film was capped with a 2- $\mu\text{m}$ -thick LPCVD film of  $\text{SiO}_2$ , and the samples were annealed at 1000°C in ammonia.<sup>2</sup> *In-situ* observations of the solidification interface were then made during ZMR in a graphite-strip-heater system equipped with an optical microscope and a video recorder.<sup>6</sup> In this report, we describe the relation between the observed liquid-solid interface morphologies and the corresponding defect structures.

Two sets of experiments were performed. In each run of the first set, the power to the upper strip heater was varied in steps between about 2.3 and 2.6 kW with the zone velocity kept at 150  $\mu\text{m/s}$ . In each run of the second set, the velocity was varied in steps from about 100 to 450  $\mu\text{m/s}$  with the upper-strip power kept constant at  $\sim 2.5$  kW. In all cases the separation between the sample and upper heater was 0.8 mm.

Figure 3-1 shows optical micrographs of the liquid-solid interface taken during ZMR at 150  $\mu\text{m/s}$ . As the power to the upper strip was initially increased, partial melting of the Si film occurred. When the power was increased sufficiently to produce a completely molten zone, a cellular-dendritic liquid-solid interface morphology was observed. As the power was further increased, a simple cellular morphology was obtained [Figure 3-1(a)], and there was a gradual decrease in both the cell period and the amplitude of the interface structure [Figures 3-1(b) and 3-1(c)]. The change in cell period is illustrated in Figure 3-2 by results for four different grains. When the power was increased above about 2.6 kW, the interface developed facets of very small amplitude.

In the cellular morphology regime, post-solidification etching and optical microscopy revealed three types of defects in the recrystallized films: isolated dislocations, dislocation clusters, and subboundaries (Figure 3-3), which were dominant at low, intermediate, and high upper-strip power levels, respectively (Figure 3-4). It has been demonstrated that the line directions of the isolated and clustered dislocations are perpendicular to the plane of the film, while subboundaries are low-angle grain boundaries composed of dislocations that lie both perpendicular and parallel to the plane of the film.<sup>4,7</sup>

Whereas cell period and amplitude both decreased monotonically with increasing upper-strip power, variations in the zone velocity at a constant power of 2.5 kW led to more complex



(a)



(b)



(c)

*Figure 3-1. Interface morphologies as a function of increasing upper-strip power. (a) 2.43 kW, (b) 2.49 kW, (c) 2.54 kW.*

96005 23

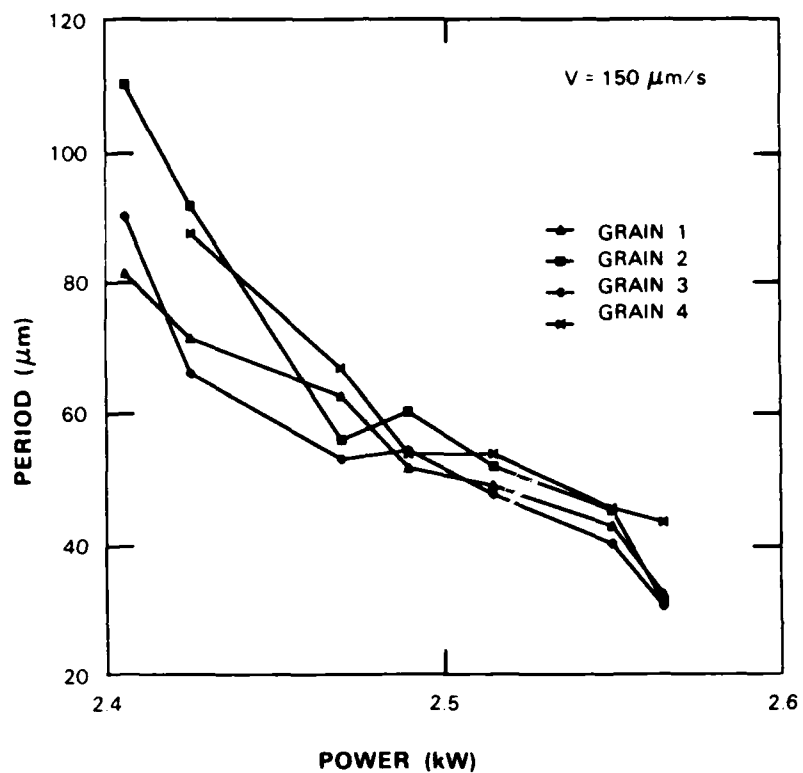
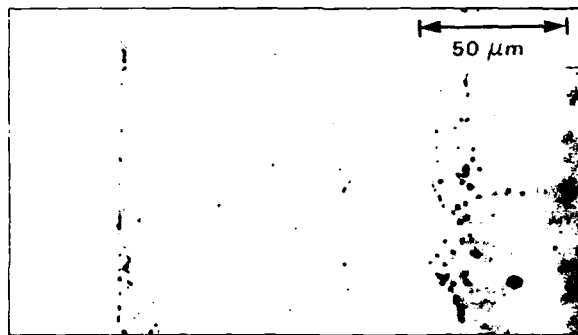
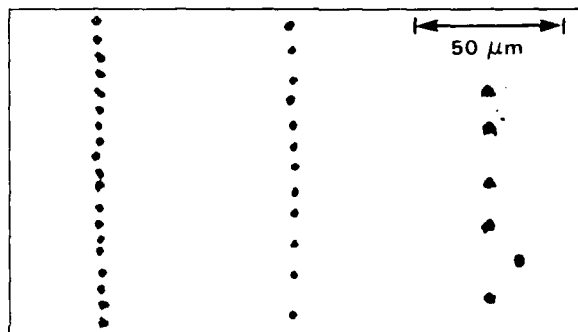


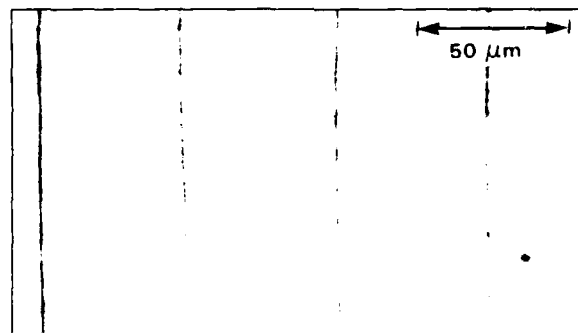
Figure 3-2. Cell spacing for four grains as a function of power supplied to the upper strip.



(a)



(b)



(c)

Figure 3-3. Optical micrographs showing three types of defects. (a) Trails of isolated dislocations. (b) Trails of dislocation clusters. (c) Continuous subboundaries.

96005-25

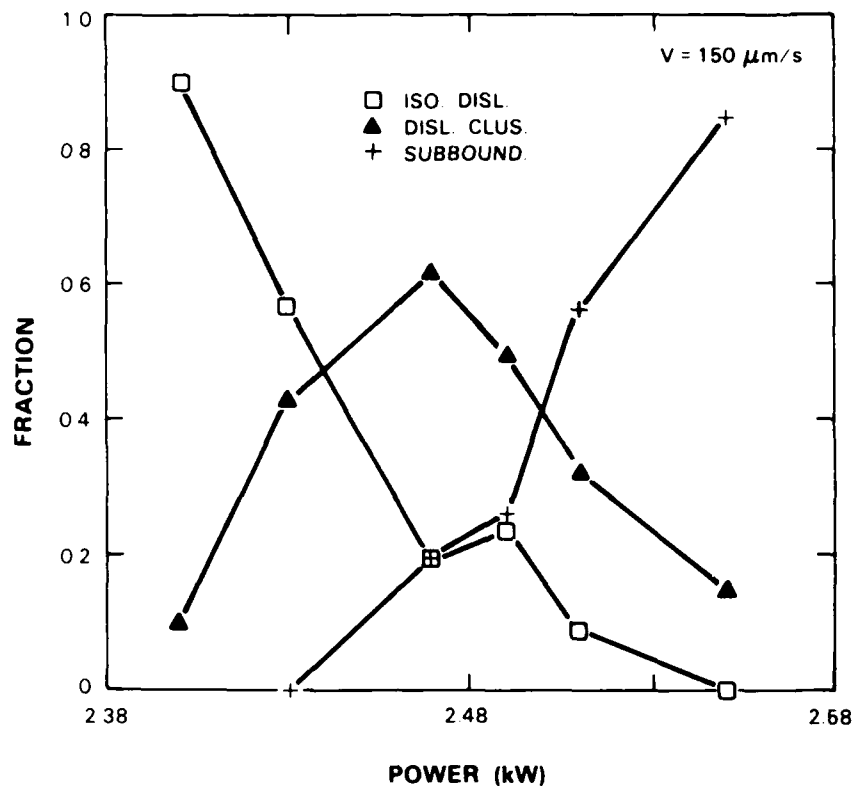
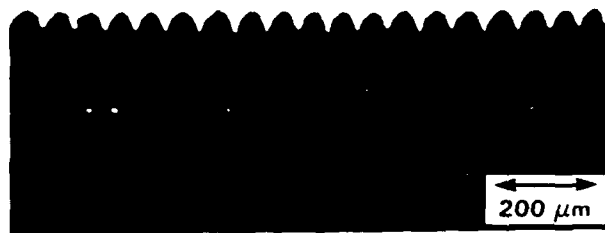


Figure 3-4. Fraction of the three defect types shown in Figure 3-3, plotted as a function of power (data were taken from a single grain).

changes in interface morphology (Figure 3-5). For low velocities, increasing velocity produced a gradual increase in the cell period (Figure 3-6) and the depth of the interface cusps also increased. Following each change in velocity a steady state was reached in a few seconds, after which new cells were not created nor existing cells annihilated. This stability resulted in the formation of parallel defect trails in the zone-melting films. When the velocity was increased above about  $300 \mu\text{m/s}$ , the cell structure became unstable. Cells would typically split in the middle [Figure 3-5(c)], and new cusps would continuously develop and vanish. With further increases in velocity, the period of this unstable interface decreased (Figure 3-6).

The changes in velocity also led to changes in the types of defects formed. For low velocities, isolated dislocations and dislocation clusters were observed [Figure 3-7(a)]. For higher velocities, in addition, X-shaped dislocation clusters [Figure 3-7(b)] were found around protrusions that presumably formed from trapped liquid droplets. When the interface became unstable, branched defect patterns were obtained [Figure 3-7(c)].

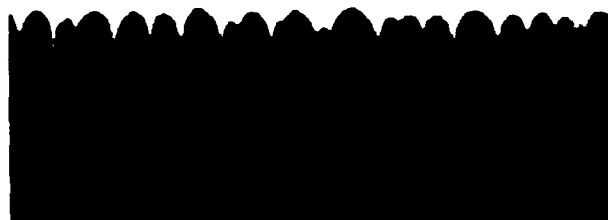
Films with the lowest defect densities were obtained at low zone velocities for upper-strip power levels at the low end of the range that yields a stable cellular interface morphology. The



(a)



(b)



(c)

*Figure 3-5. Interface morphologies as a function of increasing velocity. (a) 90  $\mu\text{m/s}$ , (b) 330  $\mu\text{m/s}$ , (c) 420  $\mu\text{m/s}$ . Upper-strip power = 2.5 kW.*

96005-27

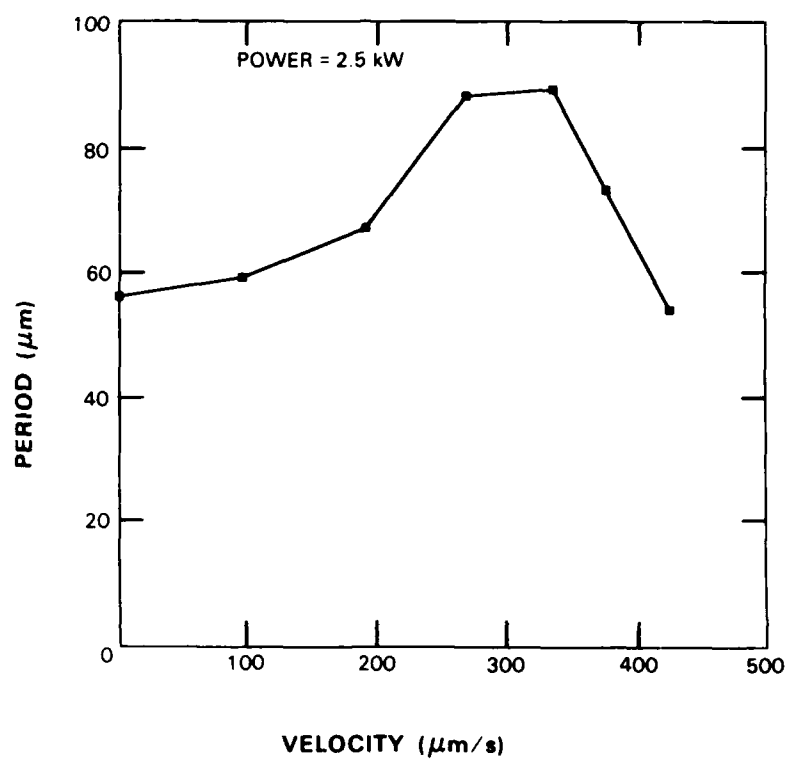
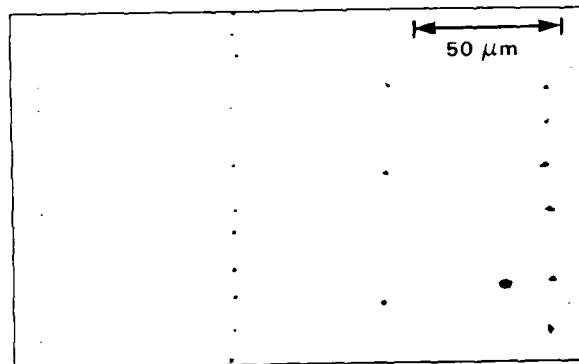
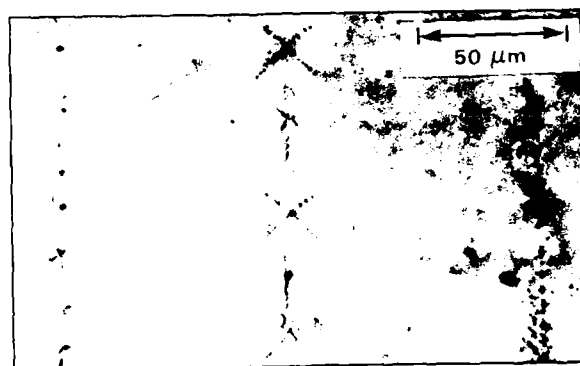


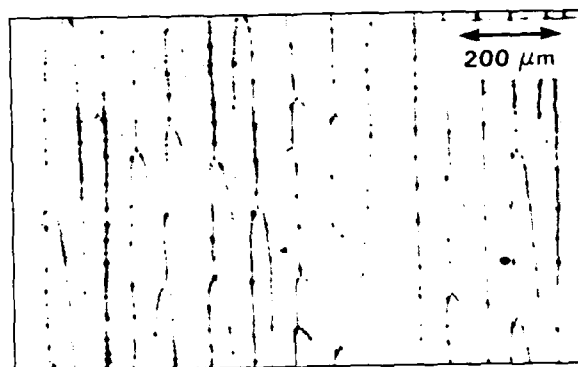
Figure 3-6. Dependence of cell period on zone velocity.



(a)



(b)



(c)

Figure 3-7. Optical micrographs showing defect patterns obtained for velocities of (a)  $90 \mu\text{m/s}$ , (b)  $330 \mu\text{m/s}$ , and (c)  $420 \mu\text{m/s}$ .

lower limit to this power range is imposed by development of a cellular-dendritic morphology, which leads to side branches and protrusions on the surface of the recrystallized films.

We propose that radiant heating from the upper strip, rather than constitutional supercooling,<sup>8</sup> accounts for the stable cellular interface morphology that is observed in the low-power, low-velocity regime yielding the lowest defect densities. If this morphology were produced by constitutional supercooling, the cell period would decrease with increasing velocity<sup>9,10</sup> but the data of Figure 3-6 show that in this regime the cell period increases with zone velocity.

The observed variation in cell amplitude and period with upper-strip power can be explained by changes in the radiation intensity gradient at the solidification interface, which increases with increasing power.<sup>11</sup> In the low-velocity regime, the reduction in cell amplitude with an increase in power reflects the corresponding increase in the intensity gradient. The decrease in the cell period with increasing power may be qualitatively understood in terms of the amplitude-to-period ratio, which roughly reflects the radius of curvature of the cell tip. For a given period, when the cell amplitude decreases the radius of the cell tip increases. Because of the increased fraction of solid Si, this change could result in significant superheating of the solid and undercooling of the liquid at the tip, leading to an unstable interface and perturbation growth. To restore the preferred tip curvature, which depends on the steady-state undercooling and the liquid-solid interfacial energy, an additional cell would then be formed, decreasing the period.

The locations of all defects observed in the solidified films correspond to the trailing cusps between adjacent cells at the liquid-solid interface. Whatever the cause of the cellular morphology, most impurities will be rejected to the cell boundaries. The dislocations present in subboundary-free films may form, at least in part, as a result of impurity incorporation along the cell boundaries.<sup>12,13</sup> When radiation intensity gradients are high enough, subboundary formation may result from thermal stress due to nonlinear thermal gradients adjacent to the interface region.<sup>4,14</sup>

C.K. Chen  
M.W. Geis

J.S. Im\*  
C.V. Thompson\*

### 3.2 IrSi SCHOTTKY-BARRIER INFRARED DETECTORS

Silicide Schottky-barrier detectors are among the most promising sensors for large-scale monolithic infrared imager arrays. State-of-the-art Schottky-barrier arrays employ PtSi detectors,<sup>15,16</sup> which have cutoff wavelength of about 6  $\mu\text{m}$ . Extension of the cutoff wavelength beyond 6  $\mu\text{m}$  has been demonstrated for IrSi (References 17 to 20) and composite Pt-Ir silicide detectors.<sup>20</sup> We report here the reproducible fabrication of IrSi detectors with a cutoff wavelength of 10  $\mu\text{m}$  at a reverse bias of 2 V, which are potentially useful for imager operation in the 8 to 12  $\mu\text{m}$  long-wavelength infrared (LWIR) region.

---

\* MIT Department of Materials Science and Engineering.

In fabricating silicide detectors, silicide-Si Schottky diodes are formed by depositing a noble metal film on a p-type Si substrate, then annealing to convert the metal to the corresponding silicide by reaction with the substrate. It has been difficult to prepare high-quality IrSi-Si interfaces because impurities (especially oxygen) have a strong effect on the reaction between Ir and Si. Consequently, the electrical and optical characteristics of previous IrSi detectors have not been reproducible from run to run. In the present work, major improvements in detector performance have been achieved by reducing impurity effects.

The IrSi detectors we have reported previously<sup>20</sup> did not have either an antireflection coating on the back Si surface or an optical cavity<sup>15</sup> for increasing the IrSi absorption. The structure of the detectors reported here has been modified by incorporation of an optical cavity. The fabrication sequence has also been modified. Previously, the Si substrate was chemically cleaned and etched, an Ir film  $\sim 20$  Å thick was deposited by electron-beam evaporation in a conventional vacuum system, and IrSi was formed by annealing the sample under  $N_2$  in a tube furnace. In the present procedure, after Ir deposition the sample was annealed *in situ* under vacuum.

High-resolution cross-sectional transmission electron micrographs of the IrSi-Si interface in samples prepared by the present and previous procedures are shown in Figures 3-8(a) and 3-8(b), respectively. In the present sample, the interface is abrupt and smooth to within one or two atomic layers. In the sample prepared by the former procedure there are apparently three fairly

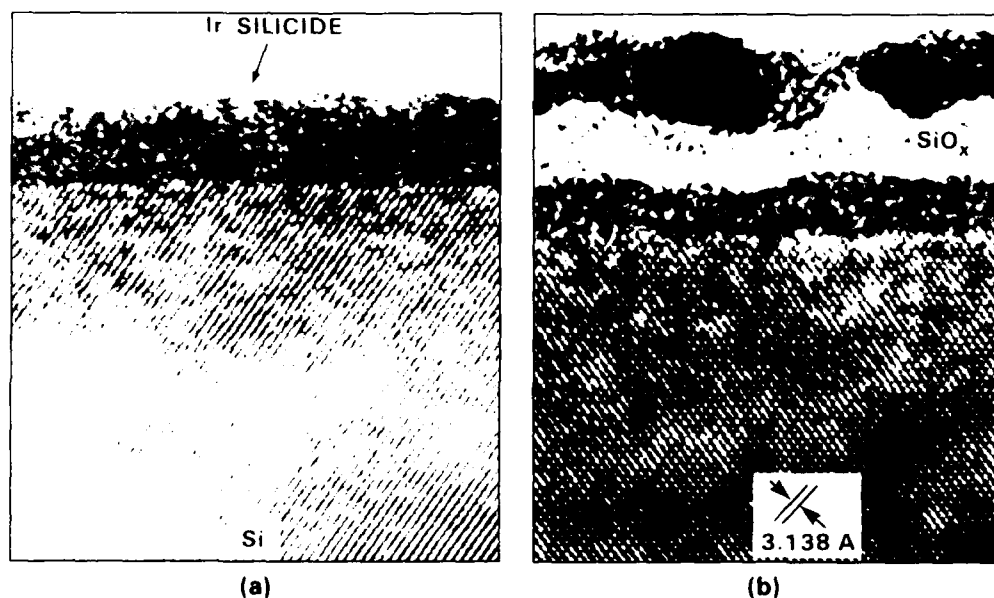


Figure 3-8. High-resolution cross-sectional transmission electron micrographs of Ir-Si samples prepared by (a) present and (b) previous processing procedures.

distinct but rather disordered layers above the substrate. In order of increasing distance from the substrate these layers appear to consist primarily of IrSi, SiO<sub>2</sub>, and Ir, respectively. These layers were probably formed during annealing because oxygen present in the N<sub>2</sub> ambient diffused down through the exposed Ir metal to form SiO<sub>2</sub> by reaction with Si that diffused up through the IrSi layer in contact with the substrate.

Figures 3-9(a) and 3-9(b), respectively, show the forward and reverse I-V characteristics measured in the dark at representative temperatures between 50 and 77 K for a typical IrSi detector fabricated by the present process. The diode characteristics are excellent, with near-unity ideality factors and high reverse-breakdown voltages. Very similar characteristics have been measured for a number of other detectors, both from the same processing run and from other runs.

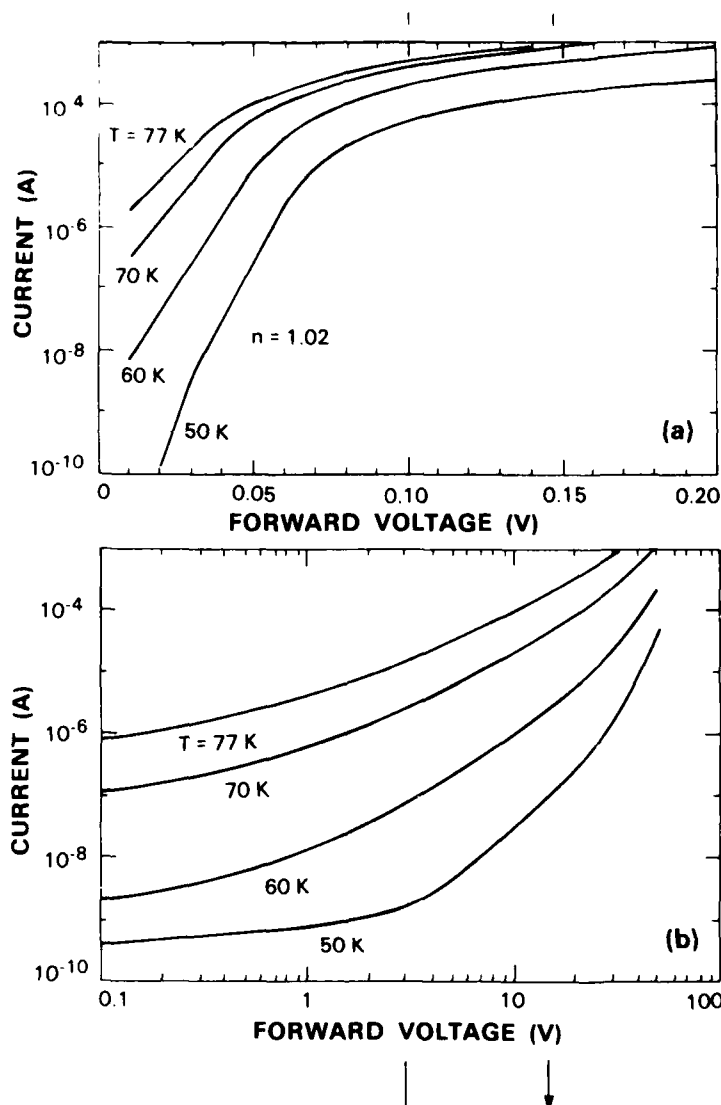


Figure 3-9. (a) Forward and (b) reverse current-voltage characteristics at four temperatures for an IrSi Schottky-barrier detector. The active device area is  $1.37 \times 10^{-3} \text{ cm}^2$ .

The barrier height  $\psi$  of a Schottky diode can be determined by activation energy analysis<sup>21</sup> from the slope of a plot of  $J/T^2$  vs  $1/T$ . Such a plot is shown in Figure 3-10 for the IrSi detector of Figure 3-9. The Schottky-barrier height obtained from the linear portion of this plot is  $\psi = 0.122$  eV.

Values of  $\psi$  have been determined independently from data for the dependence of the quantum efficiency  $Y$ , the number of carriers collected per incident photon, on the photon energy  $h\nu$ . For values of  $h\nu$  extending over a limited range above  $\psi$ ,  $Y$  of a Schottky-barrier detector is given approximately by a modified Fowler equation<sup>22</sup>

$$Y = C_1 \frac{(h\nu - \psi)^2}{h\nu}, \quad (3-1)$$

where the emission coefficient  $C_1$  measures the efficiency of the internal photo-emission process. According to this expression, a plot of  $(Y h\nu)^{1/2}$  vs  $h\nu$  will yield a straight line of slope  $(C_1)^{1/2}$  whose intercept on the  $h\nu$  axis is equal to  $\psi$ , which we designate as the optical barrier height. The cutoff wavelength is defined as  $\lambda_c \equiv 1.24 \psi$ . Figure 3-11 shows such a plot based on the

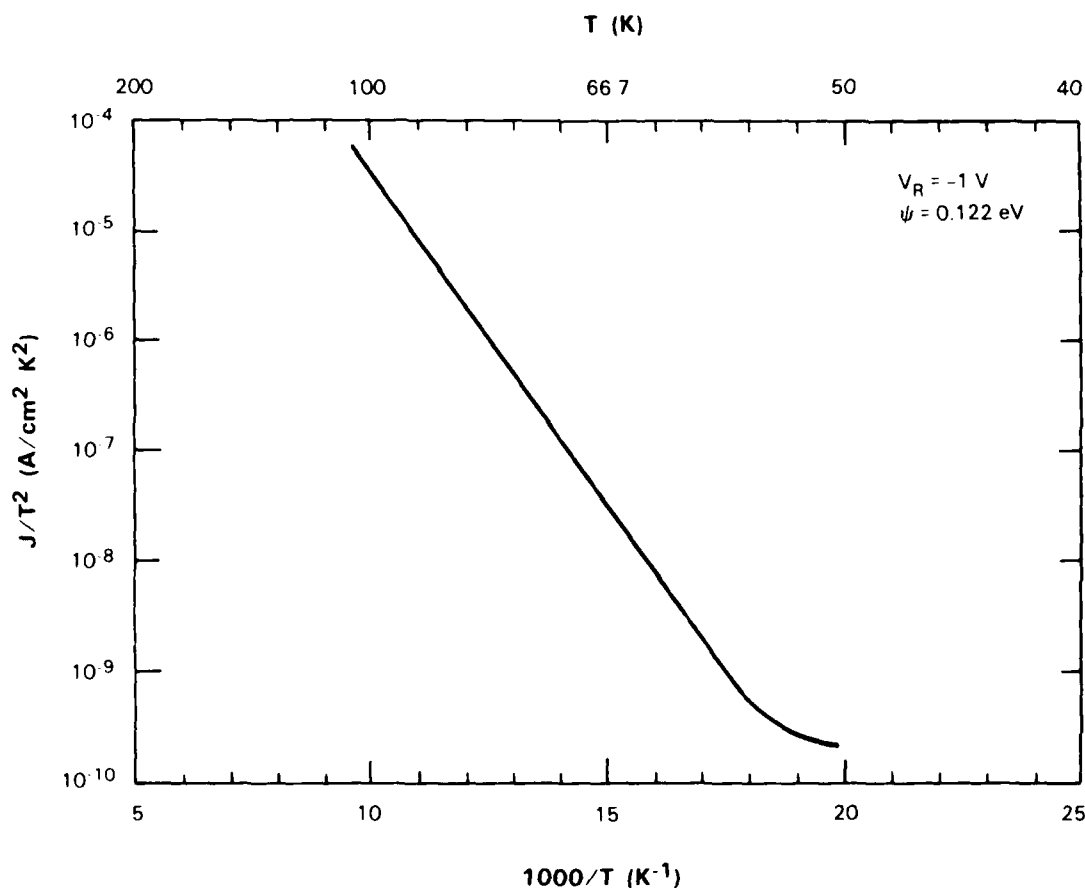


Figure 3-10. Plot of  $J/T^2$  vs reciprocal absolute temperature  $1/T$  for the IrSi detector of Figure 3-9, where  $J$  is the dark-current density at a reverse bias voltage  $V_R = 1 \text{ V}$ .

experimental data measured at 40 K over the wavelength range from 1 to 10  $\mu\text{m}$  for operation at a reverse bias voltage of 2 V. Extrapolation of the straight line drawn through the points in the lower-energy region yields an optical barrier height of  $\psi = 0.129$  eV, corresponding to a cutoff wavelength of 9.6  $\mu\text{m}$ . The value of  $\psi$  is slightly higher than the value found by dark-current activation analysis. This difference is expected because the photoexcited hot carriers in the silicide lose some of their energy through lattice collisions prior to emission over the Schottky barrier.

The  $C_1$  value determined from the plot of Figure 3-11 is  $0.096 \text{ eV}^{-1}$ , which is still much lower than the values of 0.2 to  $0.3 \text{ eV}^{-1}$  obtained for PtSi detectors.<sup>15</sup> Consequently, the values of  $Y$  for this detector exceed those of the PtSi detectors only for wavelengths greater than 3.5  $\mu\text{m}$ . However, there is a good possibility that processing under ultrahigh-vacuum conditions

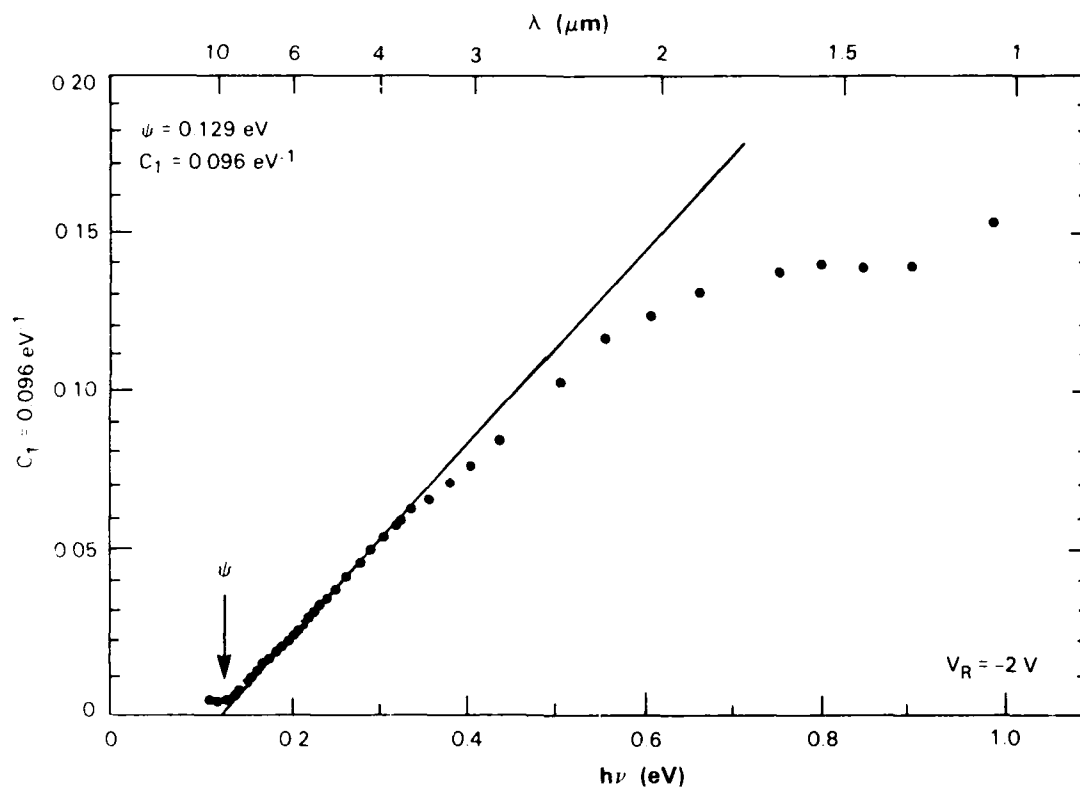


Figure 3-11. Plot of  $(Y h\nu)^{1/2}$  vs photon energy  $h\nu$  for the IrSi detector of Figure 3-9, where  $Y$  is the quantum efficiency measured at a reverse bias voltage  $V_R = 2 \text{ V}$ .

can further reduce the effects of impurities, particularly oxygen, sufficiently to yield detectors with high enough emission coefficients and therefore quantum efficiencies to permit their use in practical LWIR imagers.

B-Y. Tsaur	P.W. Pellegrini*
M.M. Weeks*	T-R. Yew†
R. Trubiano*	

---

\* Rome Air Development Center

† MIT Department of Materials Science and Engineering

## REFERENCES

1. M.W. Geis, C.K. Chen, H.I. Smith, P.M. Nitishin, B-Y. Tsaur, and R.W. Mountain, *Mat. Res. Soc. Proc.* **53**, 39 (1986).
2. C.K. Chen, M.W. Geis, M.C. Finn, and B-Y. Tsaur, *Appl. Phys. Lett.* **48**, 1300 (1986). DTIC AD-A169540.
3. L. Pfeiffer, K.W. West, and D.C. Joy, *Mat. Res. Soc. Proc.* **53**, 29 (1986).
4. M.W. Geis, H.I. Smith, and C.K. Chen, *J. Appl. Phys.* **60**, 1152 (1986), DTIC AD-A172571.
5. L. Pfeiffer, A.E. Gelman, K.A. Jackson, K.W. West, and J.L. Batstone, *Appl. Phys. Lett.* **51**, 1256 (1987).
6. J.S. Im, H. Tomita, and C.V. Thompson, *Appl. Phys. Lett.* **51**, 685 (1987).
7. M. Haond, D.P. Vu, D. Bensahel, and M. Dupuy, *J. Appl. Phys.* **54**, 3892 (1983).
8. J.W. Rutter and B. Chalmers, *Can. J. Phys.* **31**, 15 (1953).
9. R.E. Jessee and H.F.J.I. Giller, *J. Cryst. Growth* **7**, 348 (1970).
10. B. Billia, H. Jamgotchian, and L. Capella, *J. Cryst. Growth* **66**, 596 (1984).
11. J.S. Im, C.V. Thompson, and H. Tomita, *Mat. Res. Soc. Proc.* **74**, 555 (1987).
12. W. Bardsley, J.B. Mullin, and D.T. Hurle, *The Solidification of Metals* (I.S.I. Publication, London, 1967), p. 93.
13. B. Chalmers, *J. Cryst. Growth* **70**, 3 (1984).
14. J.M. Gibson, L. Pfeiffer, K.W. West, and D.C. Joy, *Mat. Res. Soc. Proc.* **53**, 289 (1986).
15. W.F. Kosonocky, F.V. Shallcross, T.S. Villani, and J.V. Groppe, *IEEE Trans. Electron Devices* **ED-22**, 1564 (1985).
16. M. Kimata, M. Denda, N. Yutani, S. Iwade, and N. Tsubouchi, *IEEE ISSCC Digest of Technical Papers* (1987), p. 110.
17. P.W. Pellegrini, A. Golubovic, C.E. Ludington, and M.M. Weeks, *IEDM Tech. Dig.* (1982), p. 157.
18. P.W. Pellegrini, A. Golubovic, and C.E. Ludington, *SPIE Symposium*, New Orleans, May 1987.
19. N. Yutani, M. Kimata, M. Denda, S. Iwade, and N. Tsubouchi, *IEDM Tech. Dig.* (1987), p. 124.

20. B-Y. Tsaur, M.M. Weeks, and P.W. Pellegrini, IEEE Electron Device Lett. **EDL-9**, 100 (1988).
21. S.M Sze, *Physics of Semiconductor Devices*, 2nd ed. (John Wiley and Sons, New York, 1981), p. 284.
22. V.L. Dalal, J. Appl. Phys. **42**, 2274 (1971).

## 4. MICROELECTRONICS

### 4.1 DIAMOND PERMEABLE BASE TRANSISTOR

Diamond is a wide band gap (5.5 eV) semiconductor with several properties that are superior to those of commonly used semiconductors. Diamond's exceptionally high breakdown voltage and high saturation velocity, depicted in Figure 4-1, project a substantial increase in both the cutoff frequency and the maximum operational voltage relative to comparable devices fabricated in GaAs or Si. Figure 4-2 shows the theoretical relation between these latter two quantities for various semiconductors. In addition, diamond also has the highest thermal conductivity of any solid at room temperature and excellent thermal conductivity from 40 to over 500 K, as shown in Figure 4-3. These properties indicate that diamond has the potential for high frequency, high power devices superior to those obtainable with Si, GaAs, or most other semiconductor materials.

Up to this time no practical diamond transistor has been reported. Prins fabricated the first bipolar point-contact transistor using natural p-type diamond, but the device has no current

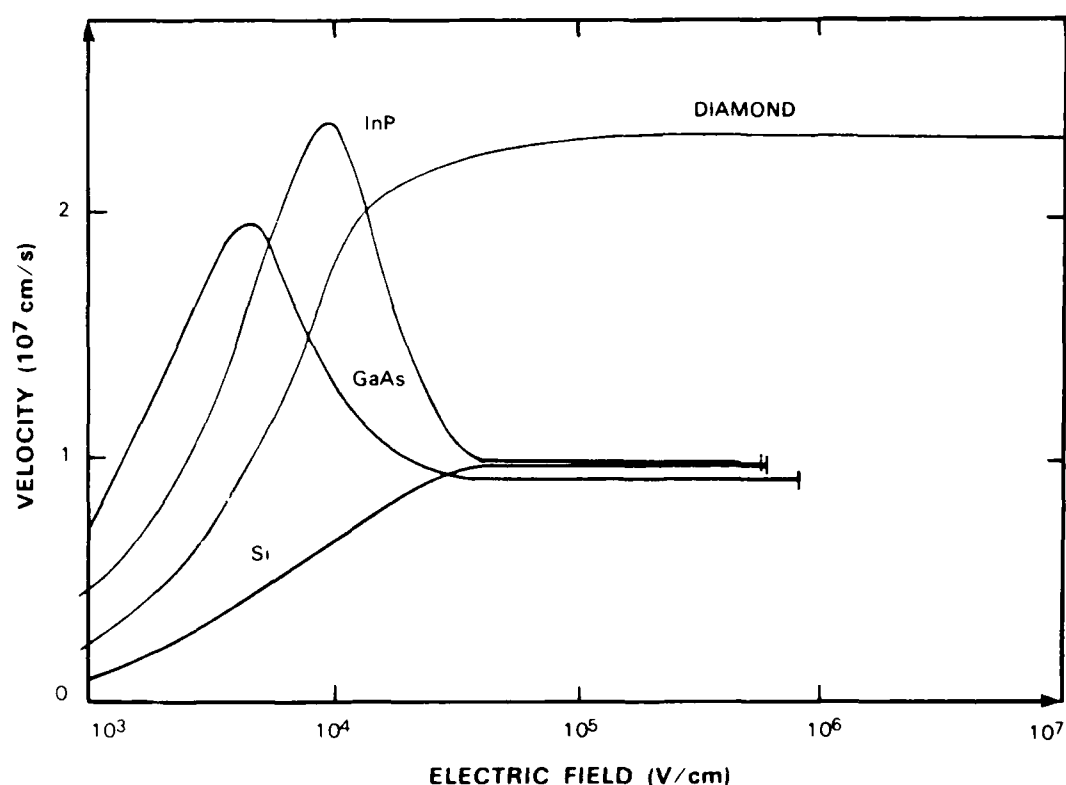


Figure 4-1. Electron velocity as a function of electric field for several semiconductors (References 1, 2, and 3). The curves are terminated at the approximate position of the electric field breakdown for each semiconductor (Reference 4).

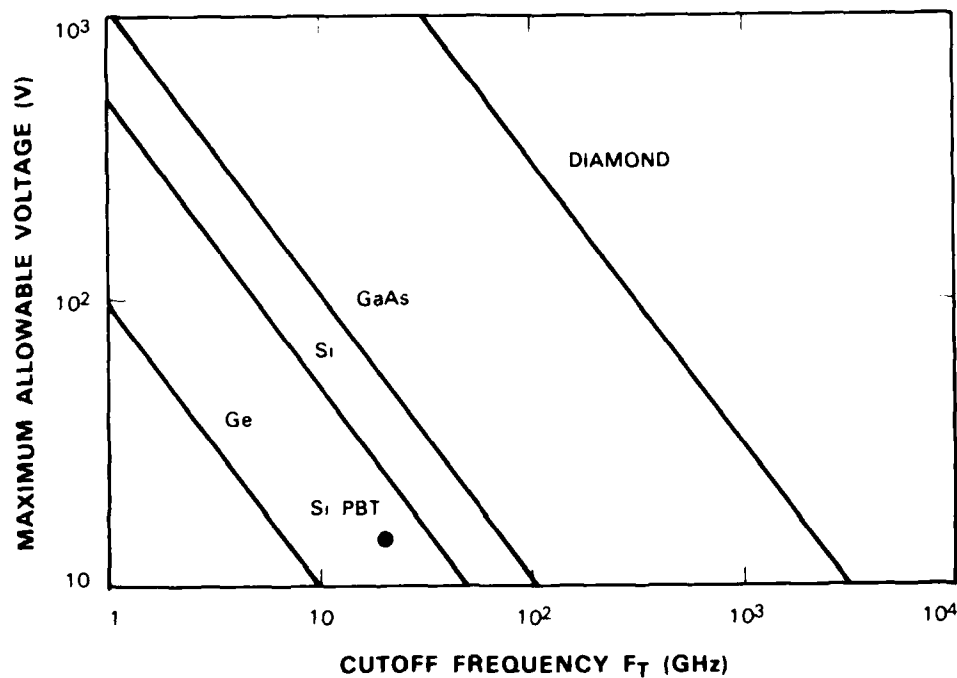


Figure 4-2. Theoretical curve of the maximum operational voltage of a transistor as a function of the cutoff frequency  $f_T$  for several semiconductors (Reference 5).

96005-35

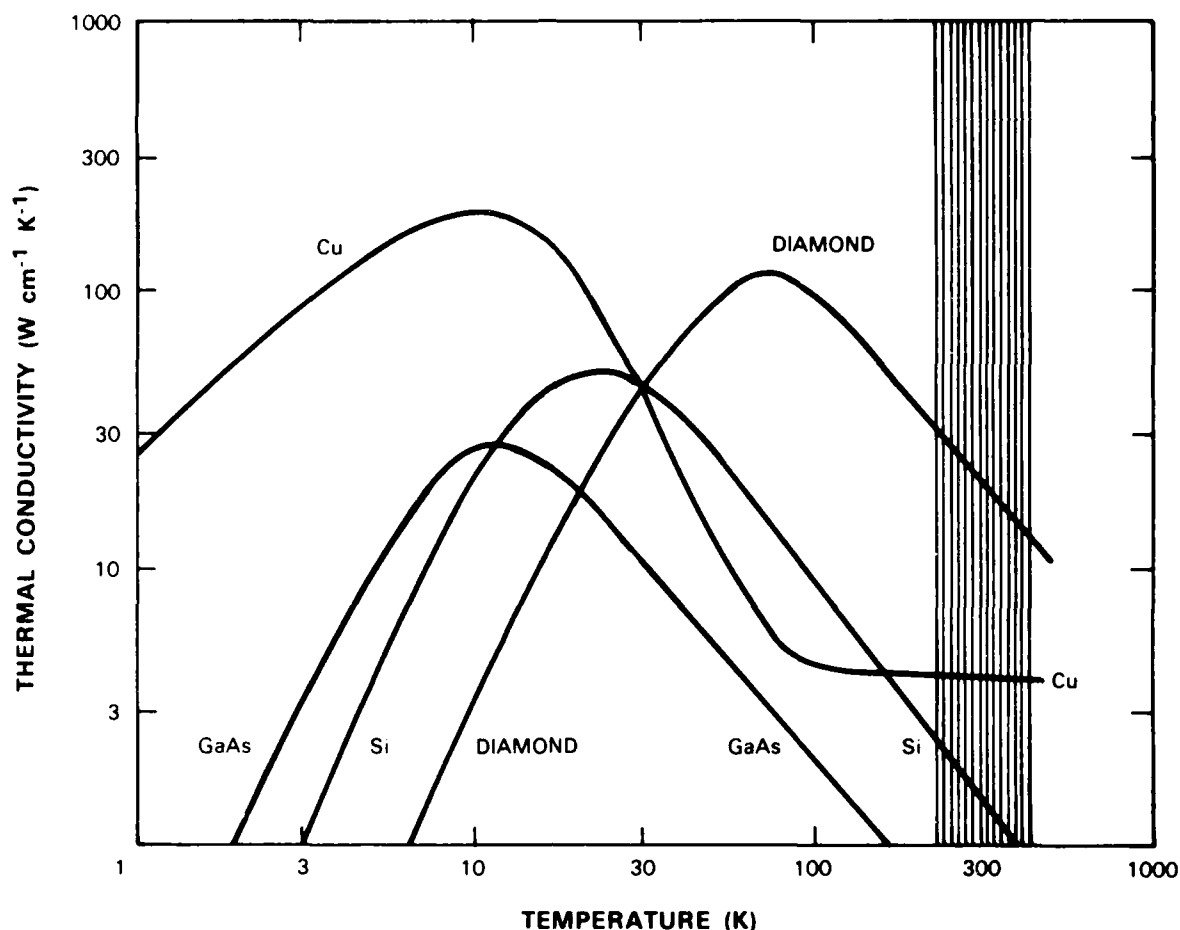


Figure 4-3. Thermal conductivities of several solids as a function of temperature. The vertical gray band around 300 K represents the temperature range from  $-25$  to  $125^{\circ}\text{C}$ . The thermal conductivity of IIa diamond is displayed (Reference 6).

gain.<sup>7</sup> Demonstration point-contact transistors have been formed on synthetic p-type diamond which exhibit power gain even at  $510^{\circ}\text{C}$  (Reference 8). Now, using the permeable base transistor (PBT) structure, the first practical transistor has been fabricated in diamond without use of point contacts. Figure 4-4(a) shows the schematic drawing of the device structure in which ion-beam-assisted etching was used to etch the  $4\text{-}\mu\text{m}$ -wide alternating base and channel regions, producing a device structure similar in topology to a Si PBT. This structure, in which the current flows vertically, does not require spatially isolated doped regions on the surface of the substrate, which are not possible to achieve on diamond with present technology. Figure 4-4(b) shows typical electrical characteristics. The device has a transconductance of  $30\text{ }\mu\text{S/mm}$ . This low transconductance is the result of parasitic resistance in the device associated with the high substrate resistance ( $10^4\text{ }\Omega\text{-cm}$ ) and is not an inherent limitation. Future devices with refined fabrication techniques and improved substrate material are expected to exhibit substantial performance improvement.

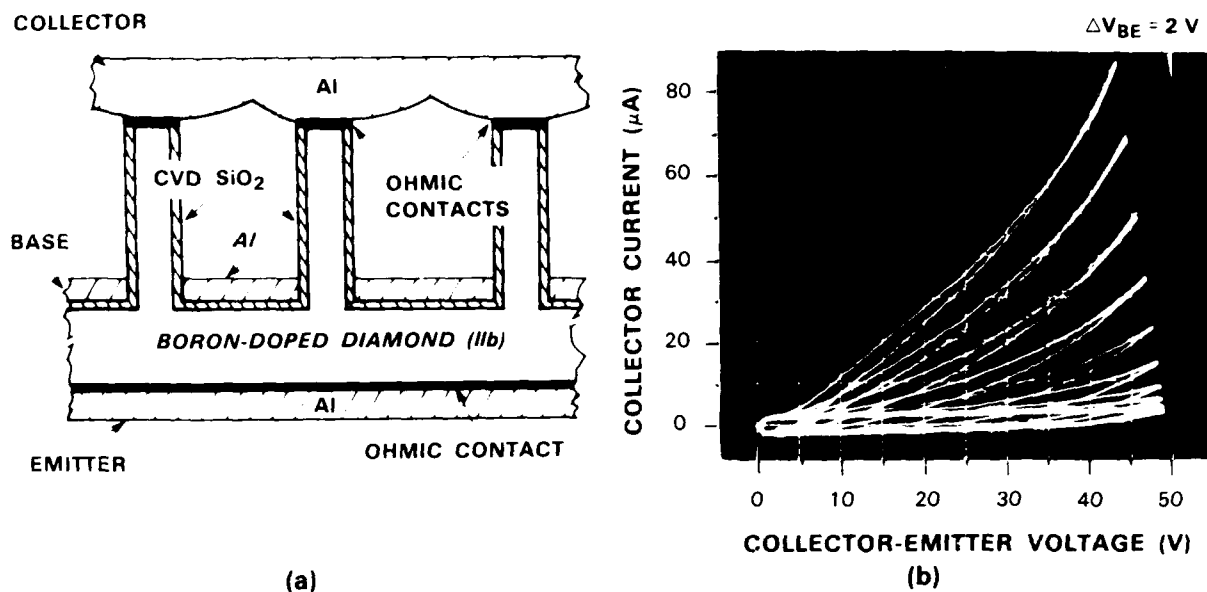


Figure 4-4. (a) Schematic diagram of a diamond permeable base transistor. To fabricate this device, ion-beam-assisted etching was used to produce the grating in the diamond (Reference 9). (b) Collector current as a function of collector-emitter voltage for base-emitter voltage steps of 2 V.

Previously the difficulty of obtaining semiconductor-quality diamond starting material and the difficulty of device fabrication have limited the practicality of electron devices in diamond. However, semiconductor-quality diamond films are now being grown,<sup>10,11</sup> and several demonstration devices have been fabricated. In the next few years high power, high frequency diamond devices may surpass the performance of devices fabricated in conventional semiconductors.

M.W. Geis  
N.N. Efremow  
D.D. Rathman

## 4.2 LASER-DIRECT-WRITE TUNING AND MODIFICATION OF MONOLITHIC MICROWAVE INTEGRATED CIRCUITS

Process-induced variations in device and circuit parameters can result in degradation of performance of a monolithic microwave integrated circuit (MMIC). However, in many instances the performance can be improved by tuning the circuit after the fabrication is completed. The tuning is usually accomplished by incorporating metallized tuning pads around the circuit and connecting selected pads with manual wire-bonding procedures which are labor intensive and time consuming. On-chip tuning in which a laser is used to disconnect prefabricated air-bridges has previously been demonstrated, but the tuning of the MMIC is limited by the quantity as well as locations of the air bridges and the tuning process is irreversible.

Laser-direct-write deposition of tungsten has been developed as a convenient and versatile technique for postfabrication trimming of GaAs MMICs. Tungsten microstrip lines of 15 to 30  $\mu\Omega$ -cm resistivity are deposited via a vapor-phase reaction induced by a focused argon-ion laser beam with micrometer position accuracy. The deposited W lines can also be easily removed by laser ablation. These W microstrip lines have been successfully used for tuning an 8-GHz GaAs MESFET amplifier and a 30-GHz monolithic attenuator. The latter application is described below.

Laser-direct-written W lines serve as shunt inductors to tune out the drain-source capacitances of GaAs MESFETs used in a Ka-band monolithic attenuator. Figure 4-5(a) is a scanning electron microscope (SEM) micrograph of the monolithic attenuator, which consists of a branch-line coupler with two MESFETs at the coupled ports. The attenuation is controlled by the variation of the drain-source impedance with the dc bias applied to the gate. The measured transmission of the as-fabricated attenuator for different gate biases is plotted in Figure 4-5(b). The maximum attenuation of the circuit is approximately 10 dB. This rather small range of attenuation is caused by the undesirable drain-source capacitance of the MESFET. Figure 4-5(c) shows the measured transmission of the circuit after a W inductive line to tune out this capacitance was deposited between drain and source using the laser-direct-writing technique. As a result, the total attenuation increased to more than 30 dB at approximately 30 GHz, the resonant frequency of the drain-source capacitance and the W inductive line. By writing different lengths of shunt inductors the maximum attenuation will occur at different frequencies. This example shows the potential of using this postfabrication writing technique for semi-custom circuit design applications.

J.G. Black	R.A. Murphy
W.E. Courtney	C.L. Chen
M. Rothschild	L.J. Mahoney
S.P. Doran	D.J. Ehrlich

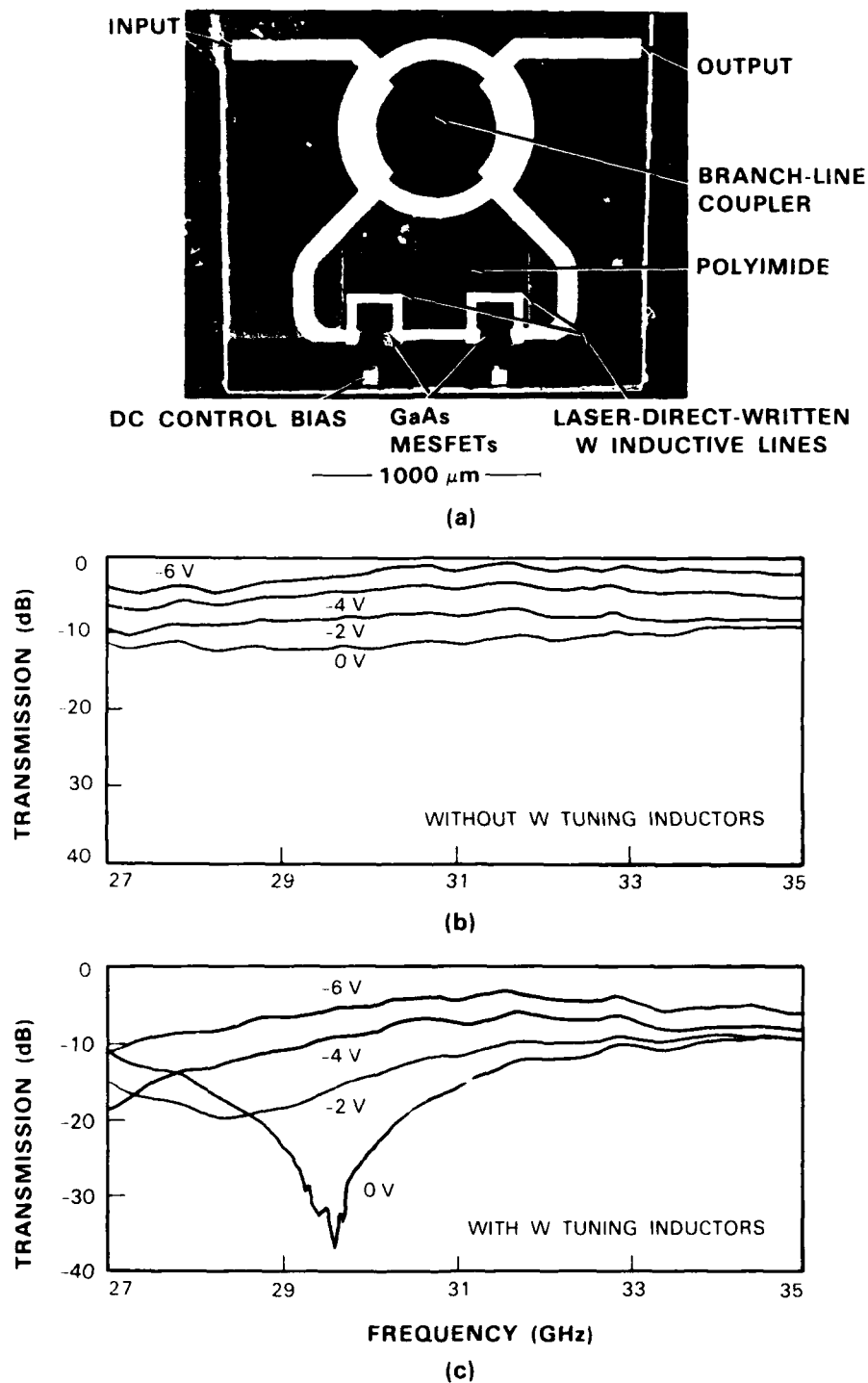


Figure 4-5. Circuit trimming of a Ka-band attenuator. (a) SEM micrograph of the monolithic attenuator using  $W$  lines as tuning inductors. (b) Measured transmission for different gate biases without  $W$  tuning inductors. (c) Measured transmission with laser-direct-written tuning inductors.

### 4.3 GaAs GROWTH ON DIAMOND SUBSTRATES BY MBE

Diamond is an attractive substrate material for high power device applications because of its high thermal conductivity, which is five times that of copper at room temperature, and over a factor of ten higher than many semiconductor materials. Diamond heat sinks have already been used in device mounting and packaging in order to improve heat dissipation. Direct heteroepitaxial growth of semiconductor devices on diamond substrates should result in reduced junction operating temperatures for power devices and lasers. At present, single-crystal diamond substrates are relatively small, but are large enough for some specialized monolithic GaAs circuit applications such as millimeter-wave oscillators or laser arrays.

Growth of high-quality GaAs on diamond would seem to be impossible, owing to a large lattice mismatch of 58 percent, despite the similarity of the two crystal structures. As a consequence of this, successful single-crystal growth will likely only be obtained for those orientations of substrate where a low mismatch superlattice ordering between the materials can be found. One such possible case appears to be between the (111) planes of GaAs and the (110) surface of diamond. Initial growths on the unreconstructed (110) diamond surface have resulted in GaAs which is predominantly (111)-oriented, as shown by X-ray and electron diffraction, but exhibits twinning. Growth on the (100) surface of diamond results in polycrystalline material over all ranges of growth conditions studied.

Growth proceeds via a nucleation process, and as a result of the twinning, the surface morphology is heavily faceted. The material is electrically insulating, even when intentionally doped, which is probably a consequence of carrier trapping at the twinning planes. Improvements in the properties of the material will require an avoidance of twinning during the growth initiation. Continuing work is directed towards that goal.

The diamond surface presents some unique characteristics as a substrate material for heteroepitaxial growth. The surface has no native oxides and is usually hydrogen terminated, such that there are no dangling bonds or surface reconstruction unless the substrate is thermally annealed at high temperatures in vacuum. The presence or absence of a surface reconstruction is a factor which strongly influences the growth process. At present, we have only investigated growth on the unreconstructed surface, because of the difficulty of reaching high enough temperatures to obtain reconstruction.

P.A. Maki  
M.W. Geis

## REFERENCES

1. D.K. Ferry, Phys. Rev. B **12**, 2361 (1975).
2. E.A. Konorova and S.A. Shevchenko, Sov. Phys. Semicond. **1**, 299 (1967).
3. L. Reggiani, S. Bosi, C. Canali, F. Nava, and S.F. Kozlov, Solid State Commun. **30**, 333 (1979).
4. A.V. Bogdanov, I.M. Vikulin, and T.V. Bodanova, Sov. Phys. Semicond. **16**, 720 (1982).
5. A. Johnson, RCA Rev. **26**, 163 (1963).
6. Y.S. Touloukian, R.W. Powell, C.Y. Ho, and P.G. Klemens, *Thermophysical Properties of Matter* (IFI Plenum, New York, 1970), Vol. 2, p. 12.
7. J.F. Prins, Appl. Phys. Lett. **15**, 950 (1982).
8. M.W. Geis, D.D. Rathman, D.J. Ehrlich, R.A. Murphy, and W.T. Lindley, IEEE Electron Device Lett. **EDL-8**, 341 (1987).
9. N.N. Efremow, M.W. Geis, D.C. Flanders, G.A. Lincoln, and N.P. Economou, J. Vac. Sci. Technol. B **3**, 416 (1985), DTIC AD-A151426.
10. H. Nakazawa, Y. Kanazawa, M. Kamo, and K. Osumi, Thin Solid Films **151**, 199 (1987).
11. R.C. DeVries, Ann. Rev. Mater. Sci. **17**, 161 (1987).

## 5. ANALOG DEVICE TECHNOLOGY

### 5.1 CONTROL OF STOICHIOMETRY OF REACTIVELY SPUTTERED NIOBIUM NITRIDE FILMS

NbN is the only compound superconductor for which a junction technology is available<sup>1</sup> and which has a transition temperature high enough to permit cooling by commercially available cryocoolers.

Reactive magnetron sputtering of niobium using argon-nitrogen mixtures has been the most successful method for the deposition of NbN films. Many investigators<sup>2</sup> have observed that the quality of the film, usually evaluated using  $T_c$  as a criterion, is extremely dependent on the nitrogen partial pressure during deposition. In general, the optimization of the deposition process is a tedious procedure in which many films must be deposited at different  $N_2$  pressures and their  $T_c$  evaluated. Because of target erosion, the magnetic field at the surface of the target is continually changing and hence the optimum condition varies with time, requiring frequent, time-consuming recalibration of the system.

Presently, there is no comprehensive theory of magnetron reactive sputtering. In fact, only very recently have theories appeared that try to explain quantitatively the behavior of magnetron sputtering.<sup>3,4</sup> However, the basic process of reactive diode sputtering is qualitatively understood and can be used as a guideline to the understanding of any reactive sputtering process.

If in a system where Nb is being sputtered in Ar we introduce increasing amounts of nitrogen, some of the  $N_2$  molecules will, at first, be positively ionized and will be accelerated toward the target, reacting with the target and forming possible NbN moieties that will then be sputtered off. In this regime, contaminated Nb films will be deposited with a transition temperature lower than pure Nb. Because most of the target is pure Nb the sputtering rate is that of niobium.

The more nitrogen we add to the chamber, the more will be ionized and consumed. At the same time, the films will become "dirtier" and their transition temperature will be further depressed. The process continues until, for a large enough  $N_2$  pressure, the rate of compound formation at the target becomes larger than the target sputtering rate. For higher  $N_2$  flow, the target is rapidly covered with nitride and deposition of NbN film occurs. At the same time, because NbN has a lower sputtering yield than Nb, the deposition rate drops substantially. Consequently, less nitrogen is necessary to form NbN and the nitrogen consumption also decreases. Furthermore, because the secondary electron yield for NbN is smaller than for Nb, the plasma impedance increases, and, for conditions of constant current or constant power, the target voltage increases.

Any of these changes can be used for process monitoring and, in fact, both deposition rate, measured by monitoring the optical emission of excited Nb atoms,<sup>5</sup> and nitrogen consumption, measured by the difference in the partial pressure of nitrogen with the plasma on and off,<sup>6</sup> have been used to optimize the stoichiometry of NbN films and, consequently, their  $T_c$ . In this work we used the target voltage, a more accessible parameter, as a control parameter.

To verify the feasibility of the process we have deposited a series of films using a magnetron cathode assembly and a Nb target at different  $N_2$  flows and at constant power. The flow of Ar was also kept constant. We varied the nitrogen flow and simultaneously measured: (1) the deposition rate, both by determining the mass of the deposited Nb (using a crystal microbalance) and by measuring the intensity of Nb optical emission in the plasma (using an optical spectrometer tuned to one of the Nb lines); (2) the nitrogen consumption; and (3) the target voltage. For twelve films approximately  $1\text{ }\mu\text{m}$  thick we measured the transition temperature and resistivity.

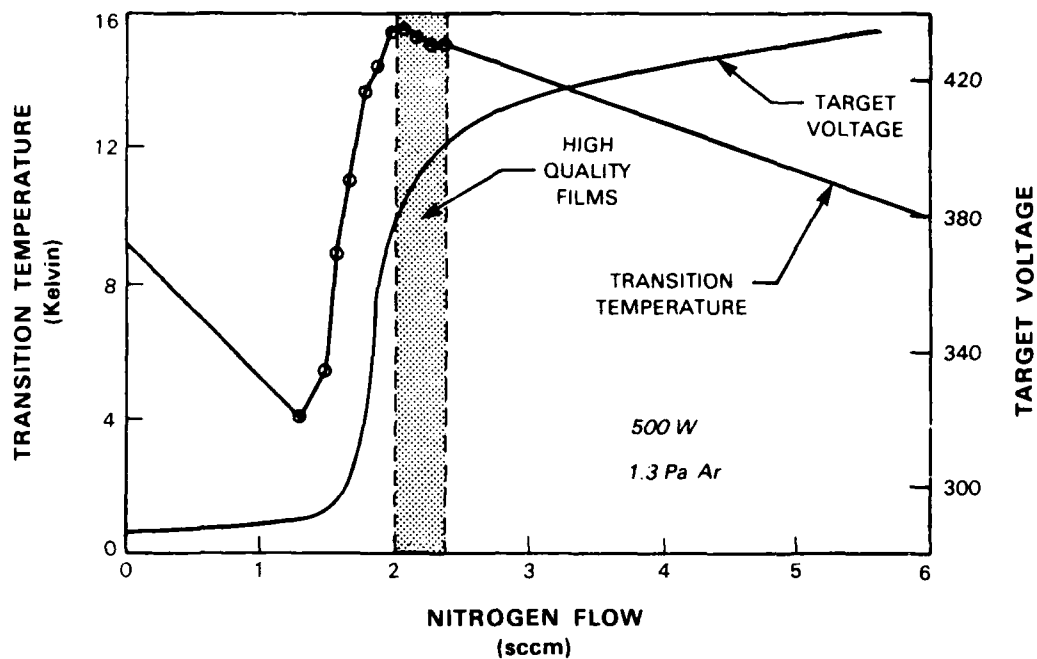
In Figure 5-1 we present data for a series of films deposited at 500 W at an Ar partial pressure of 1.3 Pa. As can be seen, the highest  $T_c$  is obtained for films deposited for  $N_2$  flow slightly higher than that corresponding to the steepest variation of target voltage, to the largest drop in deposition rate as measured by the crystal microbalance or optical spectrometer, and to the maximum nitrogen consumption.

Based on the above experiments, a simple scheme using the target voltage as a control parameter, represented schematically in Figure 5-2, was implemented to control the process. The target voltage is sampled and compared with a reference level. The difference is amplified and used to regulate a flow controller for  $N_2$ . In optimizing the process the following procedure is used: with the feedback loop open, the flow of nitrogen is slowly increased while monitoring the target voltage. The control system is then used to deposit two or three films with the feedback loop holding the target at voltages near where we expect to find the highest  $T_c$ . In our experience, with films deposited at different powers and different pressures of Ar, we usually have been able to obtain the film with the highest  $T_c$  in the first trial.

We believe this same simple process can be used to control the stoichiometry of films in any reactive sputtering process.

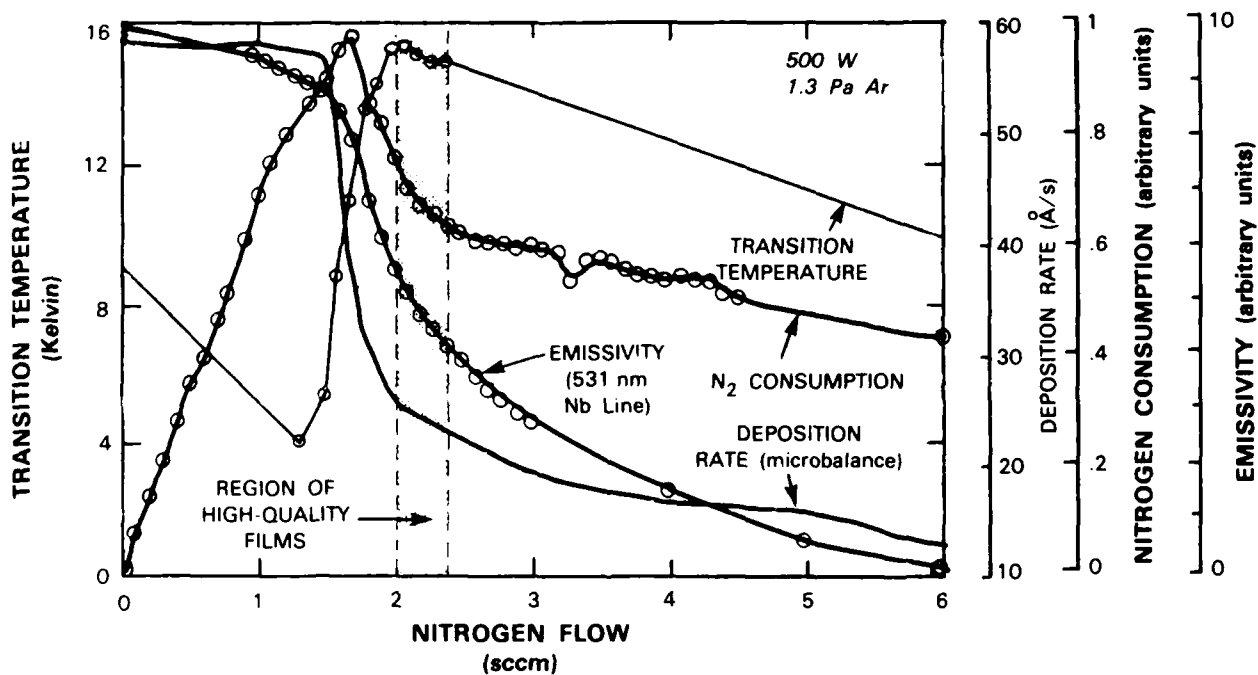
A.C. Anderson  
D.J. Lichtenwalner  
W.T. Brogan

96005-39



(a)

96005-40



(b)

Figure 5-1. (a) Variation of the target voltage and transition temperature as a function of nitrogen flow for reactive sputtering of NbN. (b) Variation of the deposition rate, emissivity, nitrogen consumption, and transition temperature as a function of nitrogen flow.

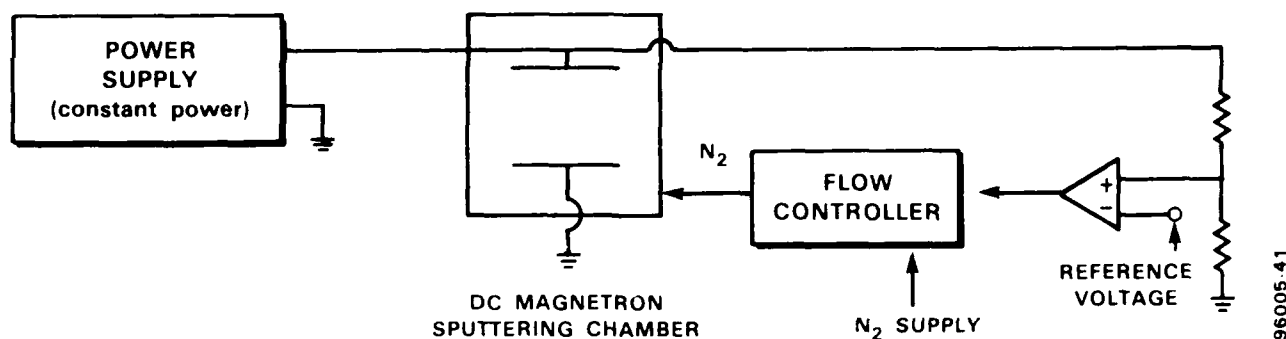


Figure 5-2. Schematic diagram of the feedback control mechanism to maintain the stoichiometry of the NbN films.

## 5.2 SUPERCONDUCTING ANALOG TRACK-AND-HOLD CIRCUIT

A superconducting analog track-and-hold circuit that uses a switching junction to capture a sample of a signal waveform as a circulating current in a superconducting loop<sup>7</sup> has been analyzed and tested. A SQUID readout device is used to determine the amount of current in the loop. While this method has lower time resolution than the binary sampler described by Faris<sup>8</sup> and Hamilton,<sup>9</sup> it can capture a single sample of a transient signal rather than iteratively comparing a necessarily repetitive input signal with a reference level. In the circuit diagram shown in Figure 5-3(a), a sine-shaped Josephson junction J1 is used as a switch across the inductance L1 + L2. As shown by the threshold curve in Figure 5-3(b), magnetic flux produced by the gate current  $I_g$  couples into J1, suppressing its critical current  $I_m$ . A sine-shaped junction is used because its threshold curve has very low side lobes.<sup>10</sup> In this case, the critical currents are highly suppressed for gate currents exceeding about 10 mA. When the critical current of J1 is suppressed, signal current  $I_s$  flows through L1 + L2 to ground. When the gate current is removed at sample time T, J1 returns to its zero-voltage state, trapping the signal current at time T in loop L1, L2, L3, and J1. Since the loop is superconducting, the signal will not decay and can be read out at any later time using the read SQUID circuit L2, L4, J2, and J3.

In designing the circuit, the following constraints must be considered:

- (1) Changes in the signal current must not exceed  $I_m(0)$ , the critical current of J1 in its hold mode. This requires that  $|\Delta I_s| < I_m(0)$  or, for signal currents with a range centered about zero,  $I_m(0) \geq 2 < I_s < + I_m(0) \geq 2$ .
- (2) Since the magnetic flux stored in the loop is quantized into integer multiples of the flux quantum, the dynamic range of the circuit is limited by the number of flux quanta which can be stored in the loop. Therefore, the dynamic range will be less than  $I_m(0) (L1 + L2 + L3) \phi_0$ , where  $\phi_0 = 2.07 \text{ mA-pH}$ .

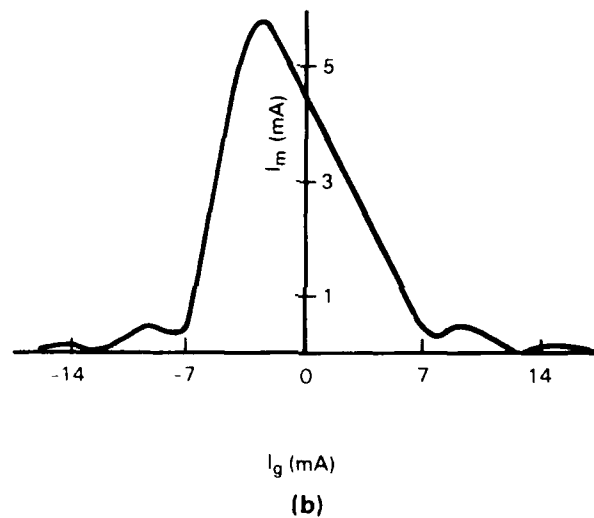
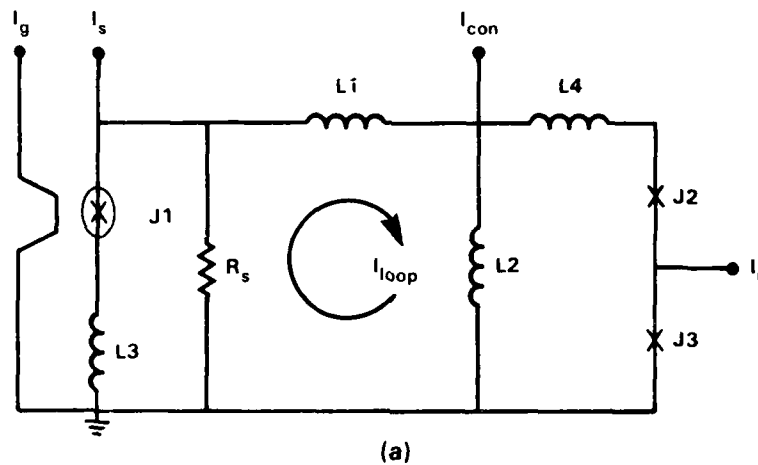


Figure 5-3. (a) Circuit diagram of superconducting analog track-and-hold. (b) Sine-shaped-junction threshold curve.

- (3) The shaped junction switch is not an ideal switch because it can carry a small supercurrent  $I_m(I_g)$  even when it is in its open state. Thus signal-current changes less than  $I_m(I_g)$  will not be tracked by the circuit and the dynamic range is limited by the ratio  $I_m(0) : I_m(I_g)$ . It has been found that a sine-shaped junction with a length of several times the Josephson penetration depth can achieve a critical current suppression ratio  $I_m(0) : I_m(I_g)$  on the order of 50, resulting in a 35-dB dynamic range.<sup>10</sup>
- (4) Another nonideal characteristic of the switch is the existence of a small parasitic inductance L3. Because of this inductance, signal variations in the hold mode are

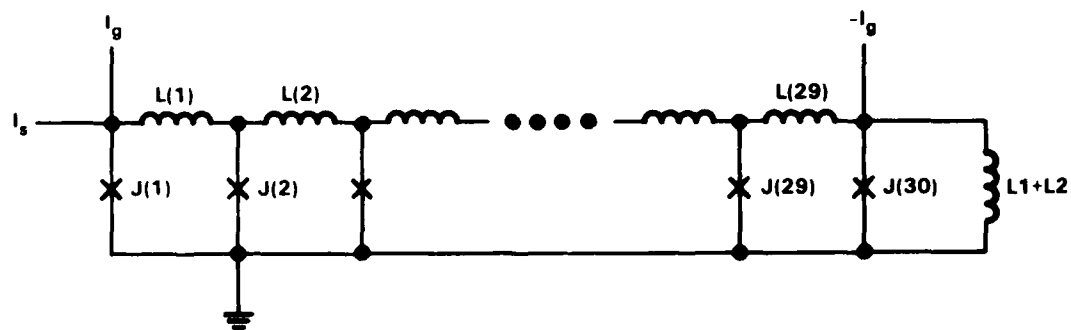
not completely shorted to ground. A small fraction  $L3/(L1 + L2 + L3)$  of the signal current is coupled into  $L1 + L2$ , resulting in unwanted feedthrough. A simple solution to this problem is to force  $I_s$  to zero before the circulating current is read.

- (5) The read-SQUID critical current is a periodic function of the circulating current to which it is coupled. Therefore, in order to avoid ambiguity in reading the circulating current, the nearly linear portion of the threshold curve should span the full range of possible circulating currents. This requirement is met if  $I_m(0)(L2 + L4) \approx 0.7 \phi_0$ . The inductances  $L2$  and  $L4$  and the critical currents of  $J2$  and  $J3$  are chosen to optimize the shape of the SQUID threshold curve.<sup>11</sup>
- (6) Optimum frequency response is achieved by choosing the value of the shunt resistor  $R_s$  such that it will critically damp the resonance formed by the capacitance  $C_{J1}$  of  $J1$  and the inductance  $L1 + L2$ . This leads to the condition  $R_s = [(L1 + L2)/4C_{J1}]^{1/2}$ . The bandwidth of the circuit will be approximately  $0.20 R_s/L$ .

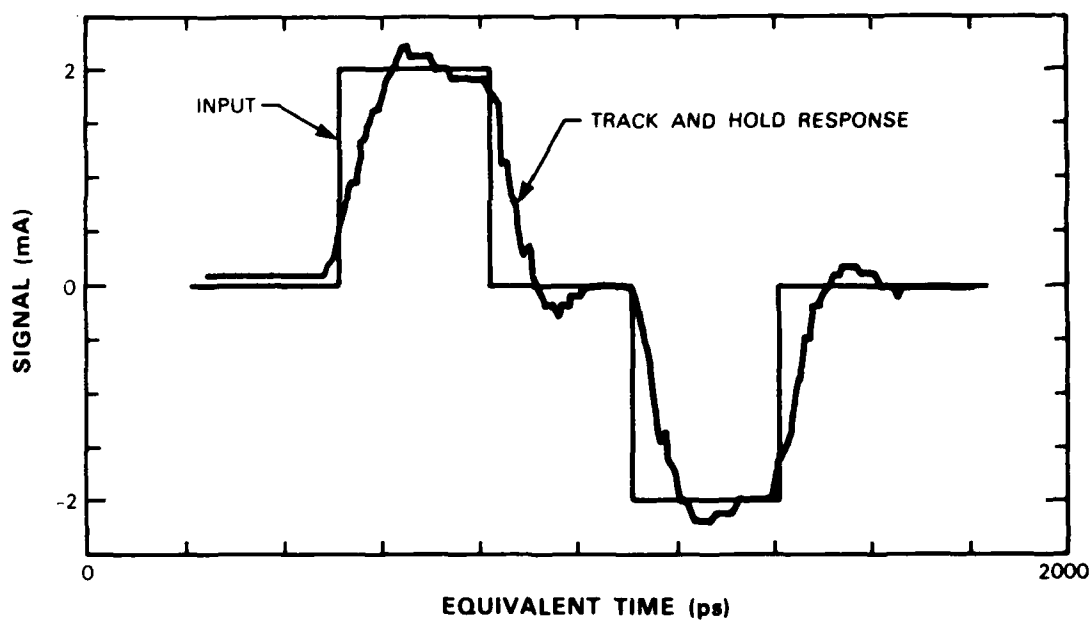
The first column of Table 5-1 shows the circuit parameters chosen to satisfy the above conditions. With these circuit parameters a numerical simulation is made by replacing the shaped junction with the lumped-element equivalent circuit shown in Figure 5-4(a). At least 30 sections are required to properly model the shaped junction.<sup>10</sup> An equivalent-time response is made by calculating the trapped current,  $I_{loop}$ , of the track-and-hold as the relative input/gate-pulse timing

**TABLE 5-1**  
**Track-and-Hold Circuit Parameters**

	Design	Measured
Critical current density	1000 A/cm <sup>2</sup>	350 A/cm <sup>2</sup>
Sine-shaped junction length	60 $\mu$ m	60 $\mu$ m
Sine-shaped junction width	35.5 $\mu$ m	35.5 $\mu$ m
$C_{J1}$ , sine-shaped junction capacitance	54 pF	54 pF
$L1$	21 pH	21 pH
$L2$	0.4 pH	1 pH
$L3$	—	1 pH
$L4$	2 pH	1.6 pH
$R_s$	0.31 $\Omega$	0.13 $\Omega$
Bandwidth	5 GHz	1.2 GHz
Critical current of $J3$ and $J4$	0.06 mA	0.05 mA



(a)



(b)

Figure 5-4. (a) Shaped junction lumped-element equivalent circuit.  
(b) Simulated equivalent-time response to a pulsed input.

is incremented and then plotting  $I_{\text{loop}}$  as a function of this relative timing. Figure 5-4(b) shows the equivalent-time response to a pulsed input. The transition times indicate that the loop current tracks the input with a 4.3-GHz bandwidth.

Circuits were fabricated which had critical current densities of  $350 \text{ A/cm}^2$ . The measured circuit parameters of the tested track-and-hold are shown in column 2 of Table 5-1.

The circuit was tested by sampling a repetitive waveform at different times and then plotting the sample value as a function of sample time, as is done in conventional sampling oscilloscopes. Figure 5-5 shows signal pulses triggered from a clock at about a 60-kHz repetition rate. The clock also triggers the gate-current transition with an electronically variable delay. The delay is swept to generate many sample points along the signal waveform. The sample values, represented by the current in L2, are read out by using a flux-locked loop around the read SQUID. This loop uses the critical current of the SQUID to sense the current in L2 and adjusts the SQUID control current  $I_{\text{con}}$  to maintain a constant value of SQUID critical current. This technique maintains a linear readout in spite of the somewhat nonlinear SQUID threshold curve. By plotting  $-I_{\text{con}}$  vs the delay time the signal waveform is reproduced.

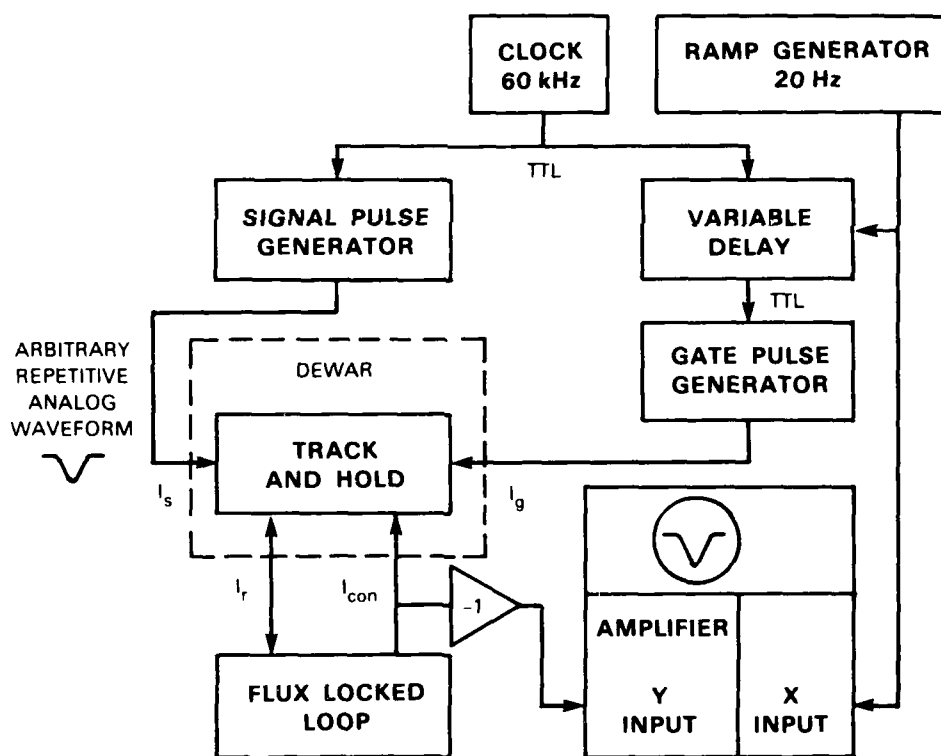


Figure 5-5. Test apparatus for high-speed analog measurements.

Figure 5-6(a) shows an input signal pulse with a 250-ps transition and Figure 5-6(b) shows the gate pulse used to trigger the sampler. Figure 5-6(c) is the equivalent-time sampler response curve showing a fall time of 300 ps, corresponding to a bandwidth of 1.2 GHz. Note that the gating pulse is not a perfect square wave. Since the sample value is averaged over the fall time of the gating pulse, the response curve will be distorted when the fall time of the gating pulse approaches the transition time of the signal waveform. Figure 5-7 shows the equivalent-time response to a sinewave input, demonstrating the ability of the track-and-hold to track at 1 GHz.

Since the bandwidth increases with decreasing capacitance  $C_{J1}$  and the capacitance can be reduced by fabricating a smaller junction at a higher critical current density  $J_c$ , the bandwidth will be proportional to  $J_c^{1/2}$ . Within the limits imposed by the fabrication technology, a bandwidth of 20 GHz can be attained.

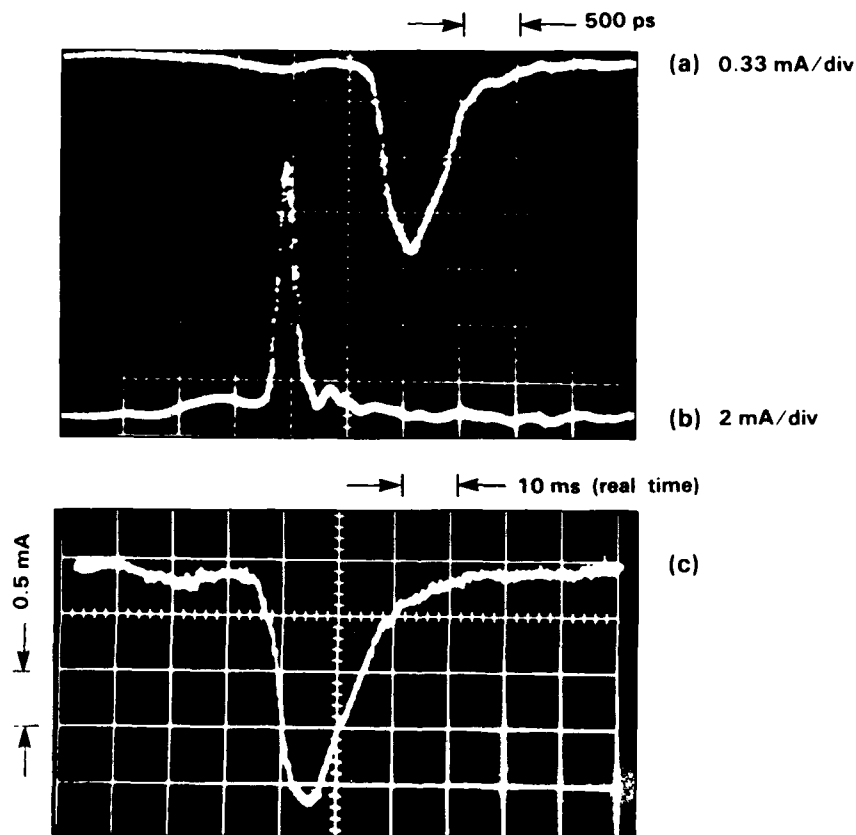


Figure 5-6. (a) Real-time input signal pulse. (b) Gating pulse used to trigger the track-and-hold. The gating pulse is swept across the input (a) to produce the equivalent-time response (c).

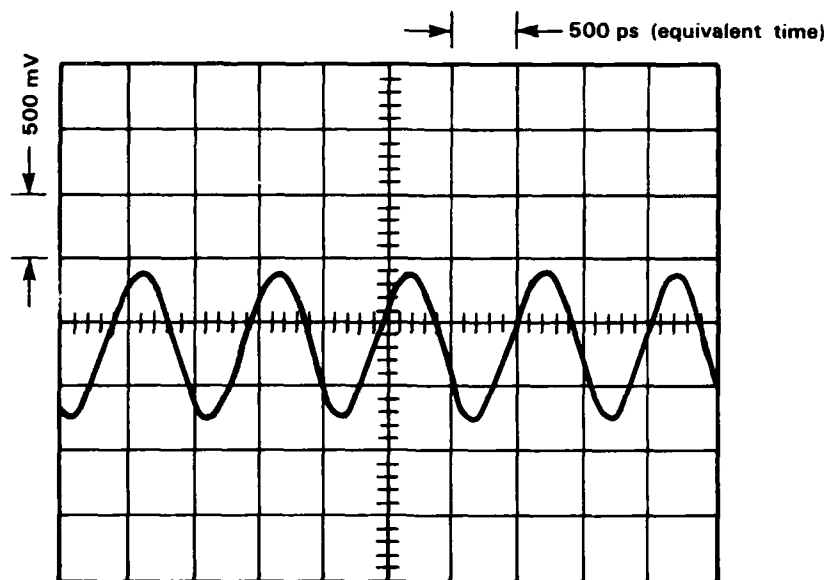


Figure 5-7. Equivalent-time response of track-and-hold to a 1-GHz sinusoidal input signal phase-locked to the system clock.

In summary, a superconducting analog track-and-hold has been analyzed and tested. Our experimental circuit demonstrates a 1.2-GHz bandwidth with dynamic range of 34 dB, consistent with circuit simulations. By reducing the junction capacitance within the fabrication limits, it is possible to obtain a 20-GHz bandwidth track-and-hold circuit. Integrating many of these track-and-hold circuits on a single chip could produce a multipoint transient recorder with a signal input bandwidth that is not currently achievable in any other technology.

D. Go	M.S. DiIorio
C.A. Hamilton	R.S. Withers
F.L. Lloyd	

### 5.3 FOUR-CHANNEL, 128-SAMPLE, 64-TAP ANALOG-TERNARY CCD CORRELATOR

A quad analog-ternary correlator has been designed and fabricated for applications that require two matched pairs of in-phase and quadrature (I and Q) channels, or simply two independent pairs of channels. A photomicrograph of the chip is shown in Figure 5-8, with specifications given in Table 5-2. This third-generation device has ternary reference weighting (+1, 0, -1), which for the first time allows electrical length control on a bit-by-bit basis. With the ability to match code lengths exactly, near-theoretical peak-to-sidelobe performance has been achieved for cyclic m-sequence autocorrelation.

Figures 5-9 shows the autocorrelation of a cyclic 63-bit m-sequence on two time scales. Theoretically, the side lobes would be perfectly flat for this case. Although it is impossible to generate an ideal input code, the peak-to-sidelobe ratio nevertheless exceeds 40 dB. An on-chip

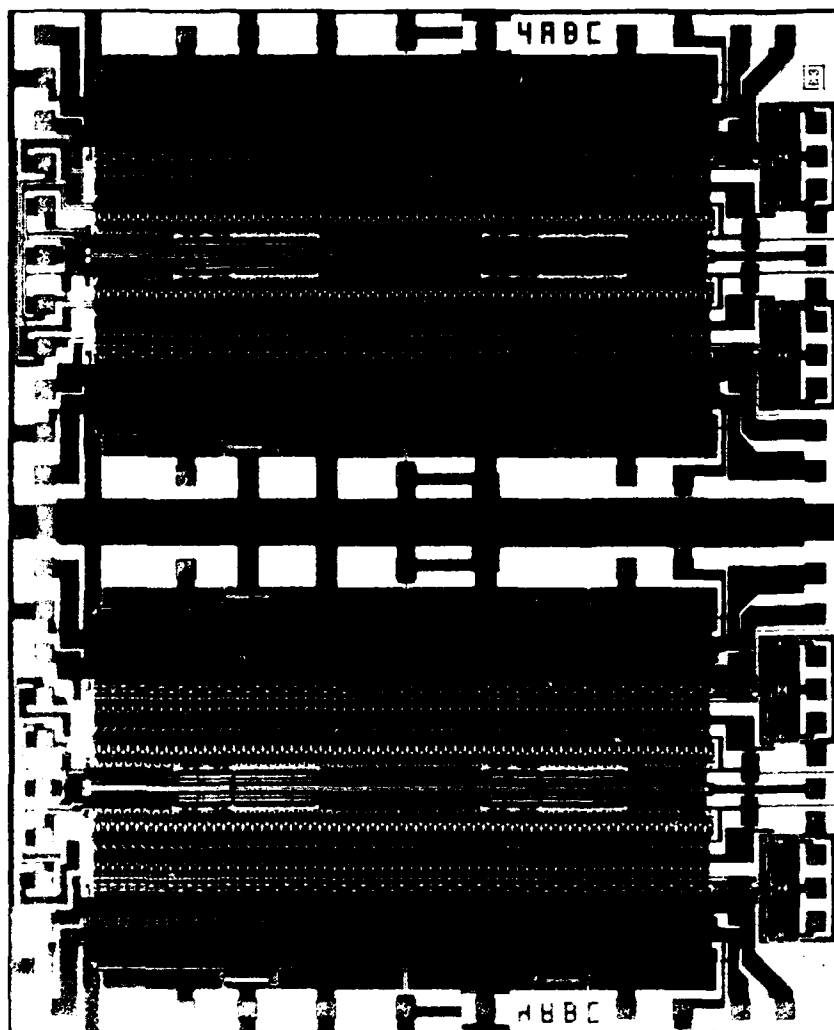


Figure 5-8. Photomicrograph of a four-channel, 128-sample, 64-tap analog-ternary CCD correlator. The chip size is  $4.8 \times 5.83$  mm.

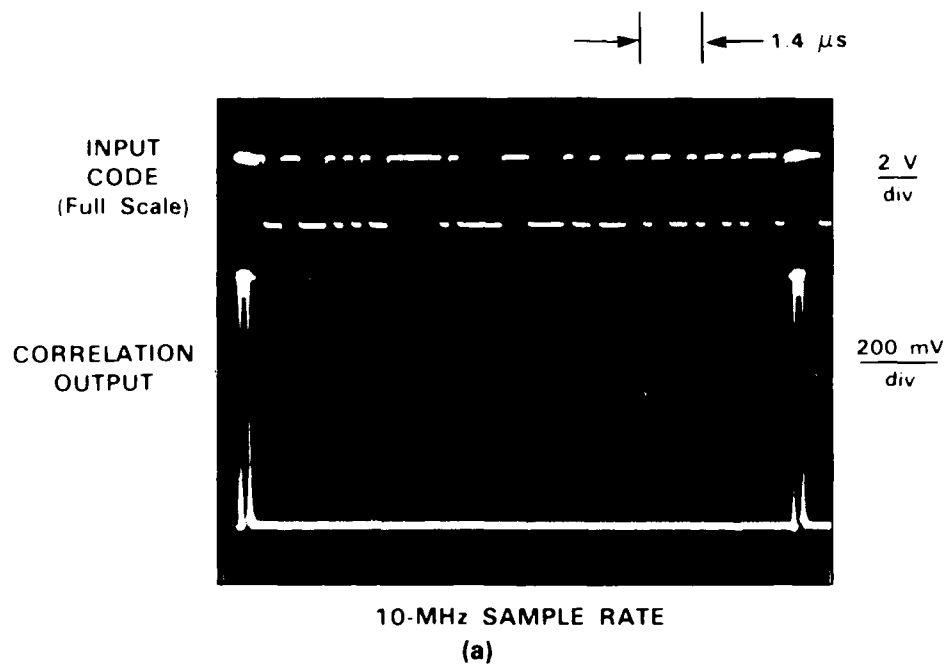
TABLE 5-2
Correlator Specifications
Quad 128-sample, 64-tap architecture
Reference code weights: +1, 0, -1
Minimum dynamic range > 66 dB
Sample rate: 10 kHz to 40 MHz
Electrical length: 2 to 64 samples
Power dissipation < 1 W
On-chip clock drivers
On-chip static protection
5-V CMOS logic compatibility
MILSPEC temperature range operation
69-lead PGA package
Adjustment-free operation
Device interchangeability

track-and-hold circuit allows the correlation spike to occupy nearly an entire clock period. As can be seen in Figure 5-9(b), a double correlation spike occurs once every code cycle. This phenomenon is due to the double-sampling, single-tapping architecture, in which the signal is sampled twice per code chip but only alternate samples (one per code chip) are sensed internally at a given time.

This architecture provides considerable flexibility. In addition to double-sampling one waveform, single-sampling of two independent waveforms is possible. In I and Q applications, for example, the I and Q inputs may alternate between the two channels in each pair (thereby facilitating MSK demodulation). If one of the two independent waveforms is the analog zero of the other, then a high accuracy auto-zero reference is available at the output every other clock cycle.

Although fabricated in mature 4- $\mu$ m NMOS technology, the device performance compares extremely favorably with digital correlators fabricated in state-of-the-art (1- $\mu$ m) CMOS technology. In addition, the CCD correlator is immune to the detrimental effects of quantization possible with digital correlators in many applications. As with its predecessors,<sup>12</sup> a major effort was made to simplify the user interface to the quad correlator. Only standard power supplies (+12V, +5V) and logic levels (5-V CMOS) are required. Aside from a fixed external resistor, all necessary support circuits (clock drivers, buffer amplifiers, etc.) have been placed on-chip; no adjustments are necessary. Device interchangeability without adjustment is possible if unit-to-unit gain variations of up to  $\pm 10$  percent are acceptable.

96005-48



96005-49

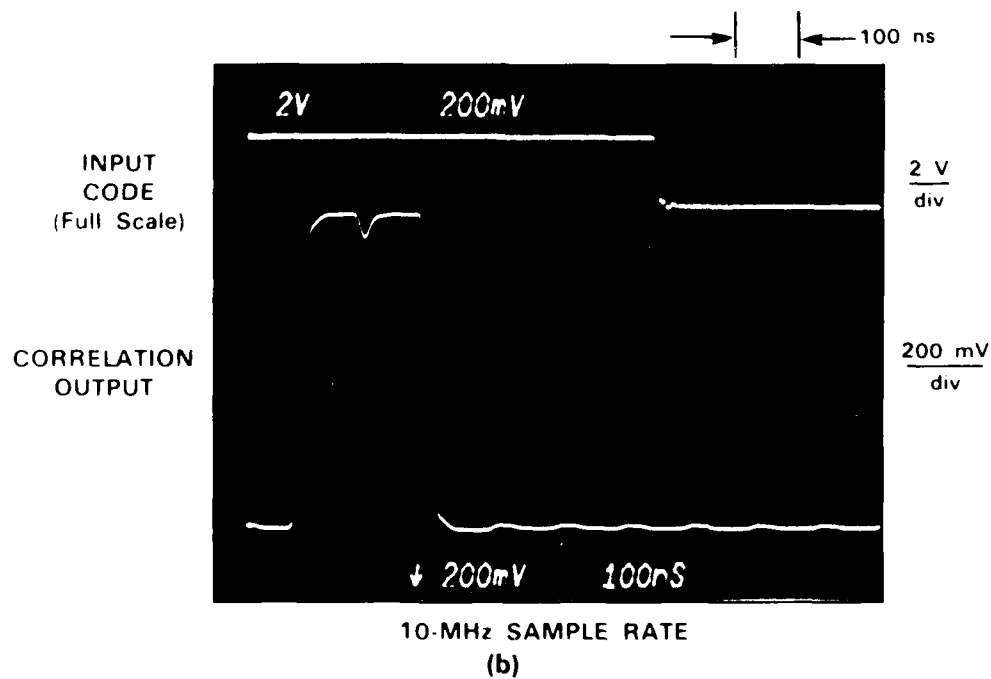


Figure 5-9. Performance of the correlator in processing a 63-chip m-sequence at a 10-MHz sample rate, displayed at a sweep rate of (a) 1.4  $\mu\text{s}/\text{div}$  and (b) 100 ns/div.

To assure that sufficient quantities of chips are available for large-scale programs, the correlator is being fabricated in a commercial foundry. In addition, we are transferring the testing and packaging technology to the foundry, so that users will be able to obtain fully qualified parts directly from industry.

A second iteration of the part is now in fabrication, with design improvements to reduce nonlinearity to less than 0.4 percent and output offsets to below 5 percent of full scale.

S.C. Munroe

## REFERENCES

1. A. Shoji, M. Aoyagi, S. Kosaka, F. Shinoki, and H. Hayakawa, *Appl. Phys. Lett.* **46**, 1098 (1985).
2. E.J. Cukauskas and W.L. Carter, *Adv. Cryogenic Eng.* **32**, 643 (1986).
3. S.M. Rossnagel and H.R. Kaufman, *J. Vac. Sci. Technol. A* **4**, 1822 (1986).
4. S.M. Rossnagel and H.R. Kaufman, *J. Vac. Sci. Technol. A* **5**, 2776 (1987).
5. M. Bhushan, *J. Vac. Sci. Technol. A* **5**, 2829 (1987).
6. S. Thakoor, J.L. Lamb, A.P. Thakoor, and S.K. Khanna, *J. Appl. Phys.* **58**, 4643 (1985).
7. Hans H. Zappe, "Apparatus for Measuring Pulsed Signals Using Josephson Tunneling Devices," U.S. Patent 3,764,905, 9 October 1973.
8. S.M. Faris, "Generation and Measurement of Ultrashort Current Pulses with Josephson Devices," *Appl. Phys. Lett.* **36**, 1005 (1980).
9. C. Hamilton, "A Sampling Circuit and Method Therefore," U.S. Patent 4,245,169, 13 January 1981.
10. R.F. Broom, W. Kotyczka, and A. Moser, *IBM J. Res. Develop.* **24**, 178 (1980).
11. R.L. Peterson and C.A. Hamilton, *J. Appl. Phys.* **50**, 8135 (1980).
12. Solid State Research Report, Lincoln Laboratory, MIT (1985:4), p. 53, DTIC AD-A172872.

UNCLASSIFIED

SECURITY CLASSIFICATION OF THIS PAGE

## REPORT DOCUMENTATION PAGE

1a. REPORT SECURITY CLASSIFICATION Unclassified			1b. RESTRICTIVE MARKINGS		
2a. SECURITY CLASSIFICATION AUTHORITY			3. DISTRIBUTION/AVAILABILITY OF REPORT Approved for public release; distribution unlimited.		
2b. DECLASSIFICATION/DOWNGRADING SCHEDULE					
4. PERFORMING ORGANIZATION REPORT NUMBER(S) 1988:1			5. MONITORING ORGANIZATION REPORT NUMBER(S) ESD-TR-88-119		
6a. NAME OF PERFORMING ORGANIZATION Lincoln Laboratory, MIT		6b. OFFICE SYMBOL (If applicable)		7a. NAME OF MONITORING ORGANIZATION Electronic Systems Division	
6c. ADDRESS (City, State, and Zip Code) P.O. Box 73 Lexington, MA 02173-0073			7b. ADDRESS (City, State, and Zip Code) Hanscom AFB, MA 01731		
8a. NAME OF FUNDING/SPONSORING ORGANIZATION Air Force Systems Command, USAF		8b. OFFICE SYMBOL (If applicable)		9. PROCUREMENT INSTRUMENT IDENTIFICATION NUMBER F19628-85-C-0002	
8c. ADDRESS (City, State, and Zip Code) Andrews AFB Washington, DC 20334			10. SOURCE OF FUNDING NUMBERS		
			PROGRAM ELEMENT NO. 63250F	PROJECT NO. 649L	TASK NO.
			WORK UNIT ACCESSION NO.		
11. TITLE (Include Security Classification) Solid State Research					
12. PERSONAL AUTHOR(S) Alan L. McWhorter					
13a. TYPE OF REPORT Quarterly Technical Report		13b. TIME COVERED FROM 11/1/87 TO 1/31/88		14. DATE OF REPORT (Year, Month, Day) 1988 August 5	
				15. PAGE COUNT 98	
16. SUPPLEMENTARY NOTATION None					
17. COSATI CODES			18. SUBJECT TERMS (Continue on reverse if necessary and identify by block number)		
FIELD	GROUP	SUB-GROUP	solid state devices      lasers      charge-coupled devices		
			quantum electronics      laser arrays      microwave semiconductor		
			materials research      optical switch      devices		
			microelectronics      nonlinear optics      silicon-on-insulator films		
			analog device technology      infrared detectors      superconductors		
19. ABSTRACT (Continue on reverse if necessary and identify by block number)					
<p>This report covers in detail the research work of the Solid State Division at Lincoln Laboratory for the period 1 November 1987 through 31 January 1988. The topics covered are Solid State Device Research, Quantum Electronics, Materials Research, Microelectronics, and Analog Device Technology. Funding is provided primarily by the Air Force, with additional support provided by the Army, DARPA, Navy, SDIO, NASA, and DOE.</p>					
20. DISTRIBUTION/AVAILABILITY OF ABSTRACT <input type="checkbox"/> UNCLASSIFIED/UNLIMITED <input checked="" type="checkbox"/> SAME AS RPT. <input type="checkbox"/> DTIC USERS			21. ABSTRACT SECURITY CLASSIFICATION Unclassified		
22a. NAME OF RESPONSIBLE INDIVIDUAL Lt. Col. Hugh L. Southall, USAF			22b. TELEPHONE (Include Area Code) (617) 981-2330		22c. OFFICE SYMBOL ESD/TML

DD FORM 1473, 84 MAR

83 APR edition may be used until exhausted.  
All other editions are obsolete.

UNCLASSIFIED

SECURITY CLASSIFICATION OF THIS PAGE